1-1-2015

Thermomechanical Stabilities in Automotive Brakes & Clutches Systems

Ali Bendawi
University of Denver

THERMOMECHANICAL STABILITIES IN AUTOMOTIVE BRAKES & CLUTCHES SYSTEMS

A Dissertation

Presented to

The Faculty of the Daniel Felix Ritchie School of Engineering and Computer Science

University of Denver

In Partial Fulfillment

of the Requirements for the Degree

Doctor of Philosophy

By

Ali Bendawi

November 2015

Advisor: Dr. Yun-Bo Yi

Author: Ali Bendawi
Title: Thermomechanical Stabilities in Automotive Brakes & Clutches Systems
Advisor: Dr. Yun – Bo Yi
Degree Date: November 2015

Abstract

This thesis involves three related topics in the area of thermal stress resulting from sliding contact of frictional materials. These three contributions collectively and the discussion of them herein form a collective basis furthering the research and understanding within this field. Firstly, the effect of convective cooling on thermoelastic instability is evaluated using finite element analysis involving insertion of a thermal convection term in the formula for frictional heat generation. It has been found that convection or radiation heat dissipation can stabilize the thermal-mechanical feedback process, leading to a raised critical sliding velocity. Two representative models for brake and clutch systems are studied. The computational results reveal that the effect of thermal convection on critical sliding speed is significant for liquid cooling, but negligible for air convection. With a practical range of convection coefficients estimated from fundamental heat transfer theories, critical speed in the presence of convection can be doubled or tripled. However, the wave number for the lowest critical speed remains nearly unchanged regardless of convective dissipation. Comparisons between linear and quadratic finite element interpolations are also made via a set of convergence studies. The results show that implementing quadratic elements in the friction layer has an obvious advantage over implementing linear elements due to rapidly-oscillating temperature-variations across the thermal skin layer. This is particularly important for future studies when higher-dimension problems are of interest. Secondly, a finite element model is

developed for the fractionally excited thermoelastic instability problem in intermittent sliding contact with finite geometries and realistic friction materials. Existing analytical solutions are used to validate the method in several limiting cases. It is concluded that some caution must be taken for the commonly-used strategy of assuming time-averaged, frictional heat generation for intermittent contact. Predictions made by half-plane analytical solutions that assume thermally-nonconductive, rigid frictional surfaces considerably overestimate dimensionless critical speeds of realistic brake and clutch systems. Long wavelength perturbations become unstable at a dimensionless sliding speed approaching zero, which opposes the convergence of two unity in half-plane solutions. Averaging the heat input over the entire circumference is appropriate only when the period of frictional contact is longer than that of separation. These results merit the use of finite element analysis in more general applications involving intermittent contact. Thirdly, in the automotive world, the usage of sliding-disk mechanical systems that produce friction has ever led engineers to address problems regarding friction, heat, and distortion of materials, particularly friction discs themselves, with many examples found when disassembling working systems. Engineers have witnessed the phenomenon of thermal buckling, the conditions of which are analyzed herein from the perspective of moments that lead to buckling. Various parameters of system configuration, geometry, and graphical analyses based on theoretical calculations of buckling potential are considered. Distribution of temperature as a system parameter is given particular importance. It is our belief that these three contributions each provide further understanding of their respective domains while their results and their implications

provide bases from which future research can be based to further a more unified understanding.

Acknowledgments

First of all, I would like to give greatest thanks to my supervisor, Dr. Yi, for his support, encouragement, expert advice, understanding, and coordination of my research. I owe a great deal of thanks to Dr. Matt Gordon and Dr. Mohammad Matin, the members of my supervisory committee. I most want to thank my wife Maha Hafala & my kids, and my Mother for their love and support, special thanks to my brother Adel enormous support and countless sacrifices to help me get to this point. Also I would like to thank all my brothers Essam & Abdalbaset and sisters Soad & Ebtesam and Asma for their love and support.

Finally I would like to dedicate this achievement to the spirit of my Father Salem Bendawi and to the spirit of my sister Amal.

Table of Contents

List of Figures

List of Tables

CHAPTER I

Introduction & Literature Review

1.1 Thermoelastic instability (TEI)

When two bodies slide against each other such as automotive disk brake or transmission clutch, frictional heat is generated and produces non-uniform thermoelastic deformation changes the contact pressure distribution. If the sliding speed is sufficiently high, the thermal mechanical feedback process is unstable, leading eventually to the localization of the load in a small region of the nominal contact area of the sliding surface, this phenomenon, generally known as “Thermoelastic instability “or TEI, was first discovered and explained by Barber (1967, 1969) in sliding systems involving frictional heating. The phenomenon of TEI has been observed in many experiments during the past half century. Parker and Marshall (1948) were the first researchers noticing the existence of local heating in railway brake tests. Similar results were later observed and reported by Sibley and Allen (1961). However, the mechanism of the phenomenon was not fully explained until Barber (1968, 1969). He found that thermal deformation is responsible for the change in contact geometry from many small widely separated contacting asperities to one or more discrete areas in which all the contact is concentrated. When the effect of thermal deformation exceeds that of wear, the contact area changes can become unstable [Barber (1969)]. Following Barber’s pioneer works on

TEI, much research in this area has been carried out and published. Those works include more than 20 publications by Barber, and around 10 publications by R.A. Burton's team. Other works include Lee and Barber (1993, 1994), Du, S. (1997, 2000), Yi, Y. B. (1999), Kao, T. K (2000). In these works, finite element methods and numerical approaches are used to quantify the thermoelastic instability problems. More practically, a team at Ford Science Research Laboratory, led by Fash and Hartsock [Harsock and Fash (2000)] work intensively and closely with Barber's group but independently on TEI as well, and experimentally validated the TEI phenomena and the models by Barber's group.

Recent study by Davis, Krousgrill and Sadeghi (2002) on the effect of temperature on TEI in thin discs indicates that above critical values of temperature and sliding speed, the response of the plate becomes unstable and exhibits large deformations, where thermal buckling and bending account for this behavior. A parametric study is conducted in this work. In another related work by Krempaszky and Lippmann (2003), Kirchhoff plate theory is used to develop a model for TEI in automotive disc clutch systems. The model is for a qualitative study of the system parameters. This work indicates, in contrast to the finding in previously mentioned work by Davis et al., the axiymmetrical buckling mode is of vital importance, if the radial expansion of the outer disc radius is constrained.

TEI and thermal buckling both can be classified as structure thermal instability problems because the structure becomes unstable due to the thermal loads. The sources of the instability are not identical; however, they can be interacting. Thermal buckling is caused by in-plane excessive thermally induced membrane compressive stresses, and is a

result of non-uniformly distributed temperature in disc. TEI is caused by non-uniformly distributed contact pressures in typically non-uniform temperature fields, and is a function of contact pressures and frictional sliding speed. Thermal stresses can cause brake disc distortion, thermoelastic instability, or even thermal buckling, which could ultimately result in brake failure. Thermal buckling of disc plate under high temperature is another type of instability, which mainly focuses on the relationship of critical thermal load (buckling load) and the buckling shape (buckling mode).

Evidences of TEI in automotive brake applications were also reported in the past decade. Andersin and Knapp (1990) found that there are four types of hot spotting in automotive friction: asperity, focal, distortional and regional. Friction material and metal counter surface wear consequences wear believed to relate to different hot spotting types. They indicate that such hot spots especially focal hot spots can provide a root cause for unacceptable performance or durability in automotive friction systems. Lee and Barber (1993) identified the onset of TEI through experimental observations and showed the stability boundary condition is a function of both the mean temperature and sliding speed. This is attributable to the temperature-dependence of the brake pad material properties, since the mean pad temperature increases as sliding

1.2 Intermittent contact

Practical brake systems, such as automotive drum brakes and caliper disk brakes, differ from the clutch problem in that the pad geometry is not axisymmetric in circumference and the sliding surfaces are not coextensive. As a result, the disk and the pad experience intermittent contact. In particular, martial points on the disk experience

periods of contact with the pad alternating with periods of non-contact. Thermally, these periods correspond to periods of frictional heating alternating with periods of convective cooling and hence the temperature at such points cannot grow exponentially with time. However, if we set up the interment contact problem in a frame of reference that is stationary with respect to the pad, exponential solutions are still possible and indeed indicated by the separable nature of the variables in the governing equations and the linearity of the system. But the Eigen functions would not be sinusoidal in general.

Barber et al. (1985), in an analysis of thermoelastic instability in railway brake, attempted to allow for this affect by averaging the heat input over the circumference. This approximation was based on the argument that the thermal transient for the system is generally much longer than the period of one revolution, so that changes in thermal distortion during a single cycle are small. However, this hypothesis had never been verified by analysis of any intermittent contact system until Ayala, et al., (1996), who investigated a simple system consisting of a rotating thin-walled cylinder sliding against rigid surface. The results showed that at low wave number, i.e., when the frequency of the process is high compared with the thermal transient of the system, only the time averaged frictional heat input is important in the critical speed is an inverse linear function of the proportion of time and sliding contact. At higher wave number, low critical speeds are obtained, but the dependence on Fourier number relatively weak. This method could be used in the brake application. But the analysis would clearly involve to many simplifications on the brake geometry as well as the boundary conditions, and it is difficult to assess the magnitude of the approximation involved. There for it would be

very desirable to solve the problem in a more practical way, in particular, using the finite element method. Geijselaers and Koning (2000) studied the intermittent contact problem in freight train wheels with block breaks using a finite element discretization. The perturbation of temperatures and distortions were described by an amplitude function, which is spatially fixed multiplied by sinusoidal running wave turn of fixed wave length. The intermittent nature of the contact was directly specified through the boundary conditions. This approach assumed the brake block to be rigid and non-conducting, and thus there was no relative motion of hot spots with respect to the wheel. Since the sinusoidal Eigen function was assumed in the analysis, the effect of the free boundary of brake blocks on the Eigen mode shape was not taken into account, ether, as a result, the approach is essentially an extension of Du's method (1997).

1.3 Brake system introduction

The study of buckling and instability of a brake rotor disc is initiated by studying the buckling of a plate. The fundamental formulas of buckling of a plate are derived from the plate theories. Therefore, the brake disc buckling study starts by first reviewing and studying the plate theories. Due to the geometric similarity between a brake rotor disc and a circular or an annular disc, some of the important research associated with buckling theories and thermal buckling of circular and annular plates are reviewed and discussed. These reviews and discussions are the basis for the study on thermal buckling of brake discs, and lead to the need to study the thermal buckling theories, analysis methods, and application of the methods to automotive brake discs. A typical automotive brake system is illustrated in Figure 1-1. In general, a brake system consists of a cast-iron rotor disc,

which rotates with the hub. When hydraulic pressure is applied, the pistons, which are fitted to each half of the caliper, are forced inwards and press segmented friction pads against the flat sides of the disc. Most vehicles built since the late 1920s use a brake on each wheel. The principle of a brake system is to decelerate and stop the car. The driver exerts a force on a brake pedal, and the force on the brake pedal pressurizes the brake fluid in a master cylinder. This hydraulic force is transferred through steel lines to a wheel cylinder or caliper at each wheel. The hydraulic pressure to each wheel cylinder or a caliper is used to force the friction materials against the brake rotor.

The friction between the stationary material and rotating rotor or disc causes the rotating part to decelerate and eventually stop. Since the wheels are attached to the rotors, the wheels of the vehicles will stop [Halderman (2000), Puhn, F (1985), DuPuy (2000)].

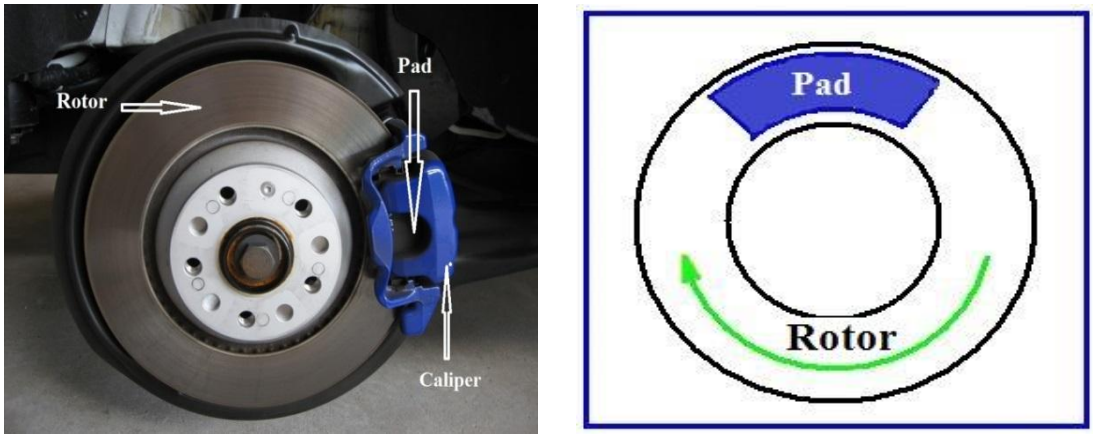

Figure 1.1: Typical disc brake system and components assembly

The function of the brake system is to convert kinetic energy into thermal energy through friction during braking. A brake has to be able to absorb or dissipate the generated heat while the brake rotor provides the friction surfaces for the brake pads to

rub against. It is a flat circular disc with a contact surface on each side. The rotor is the largest and heaviest part of a disc brake, and is usually made of cast iron because of cast iron's excellent friction and wear properties. There are two basic types of rotors: solid (as shown in Figure 1-1) and vented. Solid rotors were the first type fitted on automobiles, and they are still used on most lightweight, low-powered cars. The focus of this dissertation is on solid rotors.

1.4 Problem background

Automotive brakes are an energy-absorbing mechanism that converts vehicle movement into heat while stopping the rotation of the wheel. To stop a wheel, the pressure is applied to each caliper (Figure 1-1) to force the friction materials against the brake rotor. The friction force between the stationary material and the rotating rotor (disc) causes the rotating part to slow down, and to decelerate the vehicle. An average deceleration rate of 15 feet per second per second (FPSPS) (3 m/s/s) can stop a vehicle traveling at 55 mph (88 km/h) in about 200 feet (61m) in less than 4 seconds. During a standard brake system test, a vehicle is braked at this rate fifteen times. Temperatures sometimes can reach as high as 980°C [Halderman (2000)].

One of the functions of a friction brake is to store and/or dissipate thermal energy generated at the interface. During braking, the potential energy and kinetic energy of a vehicle are converted into thermal energy via the mechanism of friction. Theoretical investigations of stop-braking predict that approximate 95% of heat generated is absorbed by the disc [Pamphlet (1976) pp. 3-4]. Figure (1.2) shows conversion of the kinetic energy of vehicle motion into heat.

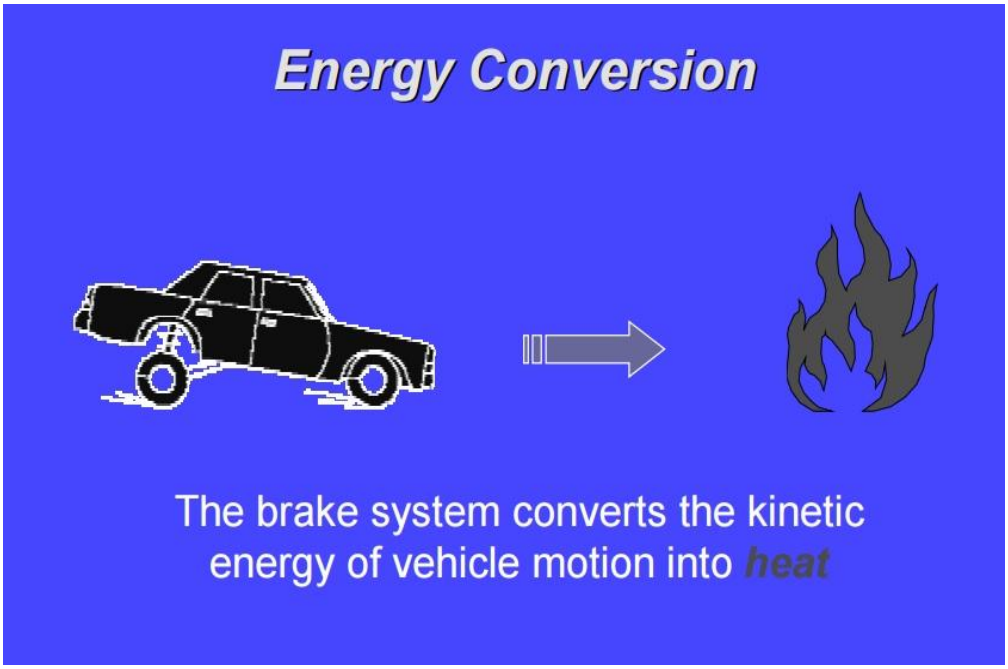

Figure 1.2: The brake system converts the kinetic energy of vehicle motion into heat

"http://www.fkm.utm.my/~arahim/daimlerchrysler-gritt.pdf "

The heat energy causes the disc temperature to rise. In general, to provide adequate braking force, the disc and a pair of friction pads as a friction pair could operate at temperatures up to 800 C, interface pressures up to 10 MPa, and a rubbing speed up to 22 m/s.

The heat generated is usually distributed through the brake structure non-uniformly, which leads to temperature gradients through the brake disc. This non-uniformly distributed temperature and the physical constraints, restraining the structure from expanding freely, generate thermal stresses on the brake structure. Since most brakes are made of malleable cast iron, it is expected that this heat generated and the induced stresses could affect the properties of the material.

The strength may decrease to as much as 20% of the room temperature strength, and the elastic moduli could also decrease [(Pamphlet (1976), pp. 3-17]. The non-uniform temperature distribution could produce non-uniform properties in the disc material. In addition to non-uniformity of heat, the repeated braking action could lead to thermal fatigue on the disc. The thermal fatigue could further lead to disc cracking and other defect. The high level thermal stresses can result in many thermally induced problems in the brake disc, such as thermal cracks on the surface of brake disc, thermal disc distortion including coning, disc thickness variation (DTV) thermal growth, disc hot spotting, and thermoelastic instability (TEI).

The thermal distortion of the disc surface can generate DTV leading to roughness. The brake roughness causes unacceptable vibration that is felt on the seat, steering wheel, and brake panel while braking. Brake roughness is a major source of customer dissatisfaction and one of the biggest sources of noise, vibration and harshness (NVH) that concerns both the automakers and customers. The combination of DTV and TEI generate disturbances at the brake disc and friction pad interface which cause brake torque variation (BTV). BTV is again a source of vibration which would lead to high NVH that leads to premature failure. These distortion and vibrations are also sources of discomfort for the passengers, and would lead to customer complaints and dissatisfaction.

The significant high level warranty cost, as well as customer complaints associated with automotive brakes is one of the most difficult and toughest jobs the automakers have to deal with. Therefore, it is very important to study and understand all the possible failure modes and design controlling factors that contribute to the problems.

1.5 History of buckling studies

The history of buckling theory of structures begins with the studies by Euler of flexible compressed beams in 1744. General theories of stability and bifurcation originated in the mathematical studies of Schmidt (1908) and Lyapunov (1947) using the inverse and implicit function theorems as basic mathematical tools, which dominate studies of buckling and post buckling structures.

Particularly, a study of the elastic stability of a thin circular plate was done first by Bryan in 1891. The study showed that the critical buckling load for a circular plate without a central hole corresponds to a radially symmetric buckling mode. Von Karman (1910) formulated the equations for bucking of thin, linearly elastic plates. The buckling of a circular annular plate subjected to shearing forces along the edges was first studied by Dean (1924). Von Karman published his plate theory in 1924, which is a starting point for many later plate theory practices and applications. In 1936, Timoshenko studied plate stability problems using thin-plate stability equations based on von Karman's equations. These early works focused on plate theory and the closed form solutions to the simple geometric structures with simple boundary conditions, such as rectangular and circular plates.

A state of the art of what was known as the theory of elastic stability, which is related to plate buckling, was published by S. Timoshenko in 1936. Relatively recent textbooks and monograph on buckling include those by Brush and Almroth (1975), Cox (1963), Gerard (1962), Ziegler (1968), Wang (1953), Godoy's (2000). Yamaki (1958) approached a study of buckling of a thin annular plate under uniform compression by

integrating equilibrium equations to derive the general stability conditions for various boundary conditions, to determine the least critical load with the ratio of radii of annular plate as the parameters. Yamaki showed that for some cases, a radially symmetric buckling mode does not correspond to the lowest buckling load. In another work by Majumdar (1971) on the same topic, for a particular case of inner free and outer clamped annular plate boundaries, the solution indicates that for small ratios of inner to outer radius, the plate buckles into a radially symmetric mode. However, when the ratio exceeds a certain value, the minimum buckling load corresponds to buckling mode with waves along the circumference. The number of waves depends on the ratio of the inner to outer radii. Laura et al. (1997) also studied the buckling for the annular plates with non-uniform thickness by using Timoshenko's optimal Rayleigh-Ritz method, which agrees well with the FEA method. Platt et al. (1992) reviewed the thin-plate stability equations in their work, discussed Timoshenko's approach, and derived the acceptable form of the thin-plate equations. This work reviews thin-plate equilibrium equations that characterize the geometrical nonlinear behavior of thin flat plate under in-plane loading based on a model proposed by von Karman. The equations are the coupled set, and the coupling of the equations arises from the compatibility condition. This coupling causes difficulties in finding solutions, especially for the cases of complex geometric shape structures.

There are also many studies using Mindlin theory applied to plate buckling. Among these works, Chang et al. (1990) studied Mindlin-thick plate applications with interior cutouts by adapting the incremental deformation concept from FEA, and

validated the results by checking against existing solutions for full-plate buckling. The study was limited to simple geometric structure and simple boundary conditions. Wang et al. (1993) presented a Rayleigh-Ritz formulation for the axisymmetric buckling analysis of radially loaded circular Mindlin plates with internal concentric ring supports. The results show that the buckling factors for circular plate with one concentric ring support decrease with increasing thickness- radius ratio due to the increasing shear deformation effect. Simple buckling formulas for simple supported and clamped plates were presented.

In another work by Wang (1997), he presented the relationships between the buckling loads determined using classical Kirchhoff plate theory, and shear deformable plate theory, which consider the first order shear deformation plate theory of Reissner-Mindlin.

For buckling load predictions with thick plate theory, Chen et al. (1988) demonstrated that the Finite Element method with selective high order elements can estimate the buckling loads. However, as indicated in Chen's work, so far, there are few references in the literature devoted to the stability analysis of thick annular plates under in-plane forces. Kumelj et al. (1993) investigated the elastic stability of thin annular plates; the numerical solutions were obtained on the basis of the energy method, and the Kirchoff-Love hypothesis was adopted for relative thin plates. In another work by Pi et al. (1993), through examining thin-walled beam columns, they showed that the classic predictions of the lateral buckling loads of beams and beam-columns are generally conservative, but the predications obtained by linearized procedure are overestimated.

The predictions by the nonlinear iteration procedure agree well with the experimental results. In this work, the buckling is assumed to be independent of the prebuckling deflections, the buckling loads obtained by including the effects of the prebuckling deflecting may significantly exceed the classical predictions. Matsunaga (1995) used another approach based on power series expansion of displacement components through the principle of virtual displacements, and presented approximate theories. He showed that this method can predict the buckling loads of an extremely thick plate more accurately compared with other refined theories and classical plate theory.

1.6 Thermal buckling problems

The previous sections presented a review of some key research works on buckling of plates; this section focuses on the review of thermal buckling of plates.

Thermal buckling of a plate is a result of excessive in-plane compressive, thermally induced membrane stresses, and plate buckling occurs when compressive membrane forces are large enough to reduce the bending stiffness to zero for some physically possible deformation modes [Cook (1989)]. The plate in-plane thermal compressive membrane stresses are the result of non-uniformly distributed temperature in the plate structure. These stresses are thermally induced rather than induced by external mechanical loads. Gossard et al. (1952) described the buckling and post-buckling behavior of rectangle plates. In this work, the critical buckling temperature was analytically determined, and the post-buckling non-linear, out-of-plate bending displacement was studied analytically and experimentally. They found that the critical temperature is independent of the modulus of elasticity. Heldenfels and Roberts (1952) in

another related work investigated the plane stresses due to temperature in plates theoretically and experimentally, and correlated the results well. The most important point, however, is that the unrestrained plate with initial transverse deflection may experience thermal buckling due to compressive stresses induced by the spatial temperature gradients.

Mote (1966) and Mote et al. (1969) studied the membrane temperature distributions and their influences on disc natural frequencies in discs. The theories and formulations for obtaining membrane thermal stresses and equation of motion provide good reference for studying and solving plate thermal buckling problems. Limpert (1972) published a dissertation on temperature and stresses analysis of solid-rotor discs, with the focus on investigating the thermal stress behavior of automotive disc brake rotors as it is affected by design parameters, operating characteristics, and environmental conditions, as well as on determining the effects of heat generation on the thermal crack characteristics.

A survey of thermally induced flexure and buckling of plates by Tauchert, T. R. (1986) provides a review of thermal buckling of plates, in which the classical plane stress problem consisting of a thin, perfect plate, isotropic plate is studied. Thornton et al. (1994) conducted an experimental study of a global-buckling response in a plate by spatial temperature gradients, and also reaffirmed that localized heating can cause substantial out-of-plane bending of real plates. The work indicates that small initial warpage with compressive membrane thermal forces are sufficient to initiate substantial transverse bending.

Some post buckling works associated to plates, some under thermal loadings, have been intensively studied by a group led by Rao, G. V and Raju, K. K. (1982, 1983, 1985, 1991, 1994, and 1995). In those works, the finite element method is employed to solve the post-buckling problems and behaviors on mainly the elastic circular plates, including the thermal post-buckling behavior on circular plates. One of the important findings in their works is that the effect of non-linearity on the load parameter is found to be much higher in the cases of thermal loading than in the case of mechanical loadings. Shih et al. (1995) studied a circular disc with axially symmetric internal membrane force with a non-uniform radial temperature distribution in the disc. They showed when the temperature is higher at the disc center, the first buckling mode is dome shaped, which maintains the polar symmetry; however, when the radial temperature is reversed, the mode of buckling changes to a saddle shape (potato chip). The Timoshenko and Woinowsky-Krieger plate equations were used for this study.

1.7 Objective and scope of the research

The objectives and scope of this research are divided into several, interrelated parts. Firstly, this work intends to establish a current understanding of thermoelastic instability (TEI) and the mechanism of convective cooling on TEI with specific focus on the use of finite element analysis (FEA). Secondly, this work intends to develop a finite element model (FEM) for the frictionally-excited thermoelastic instability problem in intermittent sliding contact with finite geometries and realistic friction materials along with validating the model in several limiting cases using analytical solutions. Finally, this work intends to establish a current understanding of thermal buckling and its associated

behavior in regard to rotor discs, specifically in regards to modes of failure, and provide results and discussion of an analytical experiment with established material properties and thermal loadings where properties of disc geometry were varied.

1.8 Overview of dissertation

This dissertation contains five additional chapters. The second chapter discusses the effect of convective cooling on thermoelastic instability through the FEM. The third chapter develops a FEM for the frictionally-excited thermoelastic instability problem in intermittent sliding contact with finite geometries and realistic friction materials and validates the model in several, limiting cases using existing analytical solutions. The fourth chapter presents an analysis of the conditions of thermal buckling from the perspective of moments that lead to buckling and details the results and discussion of an experiment where various parameters for system configuration and geometry were considered under several models of thermal loading. The fifth chapter provides a collective summarization and corresponding discussion and conclusions of the second through fifth chapters along with recommendations for future study.

CHAPTER 2

Effect of Convective Cooling on Frictionally Excited Thermoelastic Instability

2.1 Introduction

It is well known that thermoelastic instability (or TEI) occurs in high speed frictional sliding systems such as disc brakes or clutches [1]. If the sliding speed exceeds a critical value, a small perturbation in the system can lead to an exponentially growing temperature or contact pressure due to the thermal-mechanical feedback. To predict the growth rate of temperature/pressure at a given sliding speed or the critical value of the speed above which the system becomes unstable, the perturbation method, sometimes in conjunction with the finite element formulation, is applied in a variety of applications. This typically leads to an eigenvalue equation in the matrix form, from which the critical sliding speed of the system can be found by searching for the lowest speed at which the leading mode has a positive growth rate.

Since the mechanism of TEI was first discovered by Barber in 1969 [2], both the analytical [3, 4] and numerical [5, 6] approaches have been widely used in the stability analyses. For the latter, the demand for extensive numerical iterations may impose a major hurdle especially on transient analyses. In automotive applications involving axisymmetric disc-like geometries, the Fourier reduction method has proven an efficient

way to overcome this difficulty [7]. Linear perturbation solutions [8] are sought that vary sinusoidally in the circumferential direction, resulting in an eigenvalue problem defined on the cross-sectional thickness domain.

The effects of various geometric configurations [9, 10] as well as material properties [11, 12] on the stability boundaries of the TEI phenomenon were investigated. However, traditionally the conductive heat transfer inside the moving solids was the only concern in most of the formulations. Other sources of heat dissipation including convective cooling and radiation were nearly always neglected. Convective cooling, in fact, is a major heat dissipation mechanism and plays an important role in brake and clutch systems. Without conductive cooling, temperatures may exceed 1000°C on some brake disc surfaces in the friction contact region [13] and in some extreme situations can reach as high as 2000°C for carbon-carbon composite multidisk brakes in aircraft applications [14].

It is well known that convective cooling is important in lowering the maximum bulk temperatures of brake or clutch systems, the effect of thermal convection on the TEI phenomenon, however, is much less studied, mainly because of the fact that the theory of TEI is concerned about the temperature variation rather than the steady state temperature level. It was believed that the majority part of heat exchange in the system occurs between the alternating hot and cold regions of the solids, as opposed to the heat transfer taking place on the fluid-solid interface in convective cooling. Due to the high sliding speed in the automotive applications, the rate of heat exchange inside the solids is typically much faster than the convective cooling, especially when the system is cooled

by air. This is because air has a relatively low convection coefficient. Some heavy duty clutches and brakes used in naval and aerospace applications, however, are liquid cooled with the cooling water contained in the water jackets [15]. Transmission fluids used in wet clutch systems may also play an important role in convective cooling. While the coefficient of air convection rarely exceeds 200 W/m^2K, it is not unusual to have a convection coefficient for liquid cooling greater than 10,000 W/m^2K [16]. It is noticed that some pioneering work was already made by Zagrodzki regarding the effect of Newtonian cooling on TEI [17], however a systematic investigation on the phenomenon, e.g. how and to what extent the convective cooling rate can affect the stability boundaries of TEI, is still unavailable in the literature. Additionally thermal radiation may also contribute to the overall heat dissipation. It will be shown later that the effect of radiation is analogous to that of convection by introducing an equivalent convection coefficient, which can be readily obtained from the Stefan-Boltzmann Law.

2.2 Basic methodology

2.2.1 Heat transfer equation

The two-dimensional heat conduction equation for the sliding bodies in the fixed frame of reference *x* and *y* shown in Fig (2.1) can be written as

$$k\left(\frac{\partial^2 T}{\partial x^2}+\frac{\partial^2 T}{\partial y^2}\right)-\left(\frac{\partial T}{\partial t}+V\frac{\partial T}{\partial y}\right)=0 \tag{2.1}$$

where *k* is the thermal diffusivity. If the sliding takes place in the y-direction, then one can assume an exponentially growing perturbation solution of the following form

$$T(x,y,t)=T_0(x,y)+\Re\{e^{bt+jmy}\Theta(x)\} \tag{2.2}$$

Where T_0 is the steady state solution, b is a complex exponential growth rate and m is the wave number defined as the number of oscillations for perturbation within a length of 2π. Note that $\boldsymbol{m}$ can take any positive real value and it has a unit m^{-1}. $\Re$ represents the real part of a complex number. Substitution of Eq. (2.2) into Eq. (2.1) yields

$$k\frac{\partial^2\Theta}{\partial x^2} - km^2\Theta - \left(jmV + b\right)\Theta = 0 \tag{2.3}$$

Applying the Galerkin finite element formulation leads to a matrix equation in the form

$$(\mathrm{K} + \mathrm{R} + b\mathrm{H})\Theta + \mathrm{Q} = 0 \tag{2.4}$$

Where **Q** is the nodal heat flux and the rest are the matrices evaluated from the aggregation of the following elemental matrices:

$$\mathrm{K}_\mathrm{e} = \int k\left(\frac{\partial \mathrm{N}}{\partial x}\frac{\partial \mathrm{N}^T}{\partial x}\right)dx \tag{2.5}$$

$$\mathrm{R}_\mathrm{e} = \int \left(km^2 + jmV\right)\mathrm{N}\mathrm{N}^T dx \tag{2.6}$$

$$\mathrm{H}_\mathrm{e} = \int \mathrm{N}\mathrm{N}^T dx \tag{2.7}$$

where $\mathbf{N}(x)$ is the shape function.

2.2.2 Frictional heat generation

The rate of frictional heat generation on the contact interface of the sliding bodies is given by

$$\mathrm{Q}_{fric} = fV\Phi\mathrm{P} \tag{2.8}$$

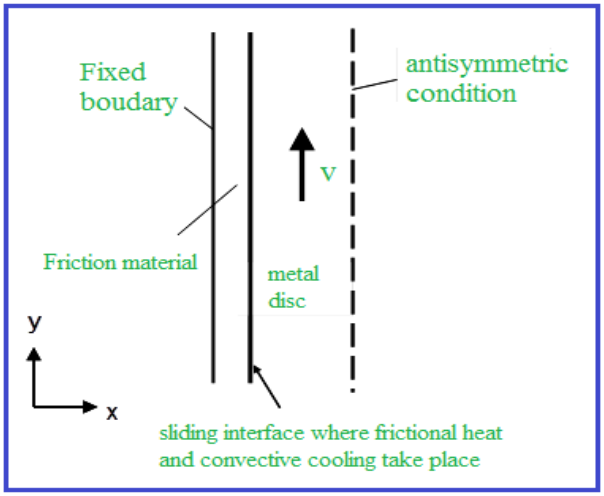

Figure 2.1: Schematic of the computational model

where **Q** is the nodal heat generation (heat flux), **P** is the nodal contact pressure defined at the contact nodes only, and *f* is the coefficient of Coulomb friction. **Φ** is a coefficient matrix constructed in the following way

$$\Phi = \begin{bmatrix} I & 0 \end{bmatrix}^T \tag{2.9}$$

2.2.3 Convective heat dissipation

Assuming a constant heat transfer coefficient *h* over the entire contact area, the convection heat loss expressed in the matrix form is then given by

$$Q_{conv} = h\Theta \tag{2.10}$$

Where both $\mathbf{Q}_{conv}$ is defined as the nodal heat loss due to convection.

Considering the net heat generation on the contact interface, Q, we have

$$Q = Q_{fric} - Q_{conv} = fV\Phi P - h\Theta \tag{2.11}$$

Please note that the terms in the above equation contain the variable components only. The constant quantities such as the ambient temperature in the convective heat dissipation satisfy the steady state heat transfer equations and therefore do not appear here. It should also be pointed out that this formulation does not apply to the clutch system described in reference [15] where water jackets cool the back side of the metal plate rather than the sliding interface. However, the temperature variation on the back side is generally much lower than that on the sliding interface, and therefore it is believed that the effect of convective cooling on TEI is less important in that situation.

2.2.4 Thermoelasticity

For plane strain problems, the constitutive law for thermoelasticity is

$$\sigma = \mathrm{C}e - \mathrm{D}T \tag{2.12}$$

Where

$$\mathrm{C} = \frac{E}{(1+\nu)(1-2\nu)}\begin{bmatrix} 1-\nu & \nu & 0 \\ \nu & 1-\nu & 0 \\ 0 & 0 & 1-\nu/2 \end{bmatrix} \tag{2.13}$$

$$\mathrm{D} = \frac{E\alpha}{(1-2\nu)}\begin{bmatrix} 1 & 1 & 0 \\ 1 & 1 & 0 \\ 1 & 1 & 0 \end{bmatrix} \tag{2.14}$$

Where ν is Poisson's ratio, E is the elastic modulus, α is the coefficient of thermal expansion and e is the strain, which can be expressed in the matrix form in terms of the nodal displacement vector **U**. That is

$$e = \mathrm{B}\mathbf{U} \tag{2.15}$$

By assuming the displacement components in the perturbation forms:

$$u_x(x,y,t) = u_{x0} + \Re(e^{bt+jmy}U_x) \tag{2.16}$$

And

$$u_y(x,y,t) = u_{y0} + \Re(e^{bt+jmy}U_y) \tag{2.17}$$

One can obtain an additional matrix equation

$$\mathrm{LU} - \mathrm{G}\Theta = \Phi\mathrm{P} \tag{2.18}$$

Where **G** is a square matrix and **L** is a rectangular matrix. The elemental matrices for **L** and **G** are defined by

$$\begin{aligned} \mathrm{L}_\mathrm{e} &= \int_\Omega \mathrm{B}^T \mathrm{C}\mathrm{B}dx \\ \mathrm{G}_\mathrm{e} &= \int_\Omega \mathrm{B}^T \mathrm{D}\mathrm{N}dx \end{aligned} \tag{2.19}$$

and

$$\mathrm{B}_i(m,x) = \begin{bmatrix} \dfrac{d\mathrm{N}_i}{dx} & 0 \\ 0 & m\mathrm{N}_i \\ -m\mathrm{N}_i & \dfrac{d\mathrm{N}_1}{dx} \end{bmatrix} \tag{2.20}$$

Here $\mathbf{N}_i$ represents the shape function of the ith node in a given element. Rearranging Eq. (2.18) in the partitioned form yields

$$\begin{bmatrix} \mathrm{L}_1 \\ \mathrm{L}_2 \end{bmatrix} \mathrm{U} - \begin{bmatrix} \mathrm{G}_1 \\ \mathrm{G}_2 \end{bmatrix} \Theta = \begin{bmatrix} \mathrm{I} \\ 0 \end{bmatrix} \mathrm{P} \tag{2.21}$$

where **I** is the identity matrix of order n_c, the number of the contact nodes. Therefore

$$\begin{aligned} \mathrm{L}_1\mathrm{U} - \mathrm{G}_1\Theta &= \mathrm{P} \\ \mathrm{L}_2\mathrm{U} - \mathrm{G}_2\Theta &= 0 \end{aligned} \tag{2.22}$$

In the above formulation, the nodal vectors are partitioned according to whether they belong to the contact nodes. This is because the contact node pairs share the same normal displacements, and also because the frictional heat is presumably generated at the contact nodes. Equation (2.22) immediately yields

$$\begin{aligned} \mathrm{U} &= \mathrm{L}_2^{-1}\mathrm{G}_2\Theta \\ \mathrm{P} &= (\mathrm{L}_1\mathrm{L}_2^{-1}\mathrm{G}_2 - \mathrm{G}_1)\Theta \end{aligned} \tag{2.23}$$

2.2.5 Eigenvalue equation

Combining Eqs. (2.4), (2.11) and (2.23) yields the following eigenvalue equation:

$$\mathrm{M}\Theta = b\mathrm{H}\Theta \tag{2.24}$$

Where

$$\mathrm{M} = fV(\mathrm{G}_1 - \mathrm{L}_1\mathrm{L}_2^{-1}\mathrm{G}_2) - \mathrm{K} - \mathrm{R} - h \tag{2.25}$$

Note that it is a standard eigenvalue equation without considering the inertial effects.

2.2.6 Convective heat transfer coefficient

In automotive applications it is generally believed that both laminar and turbulent flows are viable depending on design and operational parameters. For simplicity, here we neglect the laminar flow regions and assume an idealized situation in which the turbulent flow covers the entire sliding surface. For an external, turbulent flow over an isothermal flat plate, the local convection heat transfer coefficient can be approximated from the Reynolds Analogy [16] as

$$Nu_x = 0.0296\,\mathrm{Re}_x^{4/5}\,\mathrm{Pr}^{1/3}, \text{ where } 0.6 \le \mathrm{Pr} \le 60 \tag{2.26}$$

In the above approximation, Pr is the Prandtl number, and Nu_x is the Nusselt number defined by

$$Nu_x = \frac{h_x x}{K_f} \tag{2.27}$$

where h_x is the local convection coefficient and K_f is the thermal conductivity of the fluid inside the boundary layer. The Reynolds number is defined by

$$\mathrm{Re}_x = \frac{\rho U x}{\mu} \tag{2.28}$$

where Re_x is the Reynolds number, ρ is the fluid density, μ is the fluid viscosity, U is the linear velocity component parallel to the plate. Assuming a typical clutch or brake disc diameter as the characteristic length, and the maximum sliding speed to be 5,000 rpm, it has been estimated that in the presence of water, the maximum convection coefficient can reach 20,000~30,000 W/m^2K, and this result is in fact quite consistent for a wide range of the characteristic length of the sliding bodies. The result is also consistent with the order of magnitude of the convection heat transfer coefficients reported in the literature regarding the wet clutch applications [18]. Note that in the above approximation, linear motion at a constant speed and parallel flow over a flat plate were assumed. In reality, however, it may vary depending on the flow conditions and geometric configurations such as grooves. Nonetheless it is expected that the actual result should have the same order of magnitude. If the transmission lubricant instead of water is used as the coolant, the high viscosity of the lubricant can bring down the Reynolds number and hence reduce the overall convection coefficient. In addition, in the above estimation the external flow condition was assumed, which is actually not the case when the lubricant is confined

between the two sliding surfaces. Hence the above result is a rough estimate and its real value should be measured from experiments. Since in the current work we are primarily concerned about the range of the parameters covered in some worst scenarios, it is reasonable to set 30,000 W/m^{2}K as the upper limit of the coefficient of convection in the discussions.

2.2.7 Radiative cooling

In addition to convection, radiation may also affect the overall heat dissipation rate due to the high operating temperatures. The Stefan-Boltzmann law denotes

$$Q_{rad} = \varepsilon\sigma(T^4 - T_\infty^4) \tag{2.29}$$

where ε is the surface emissivity and σ is the Stefan-Boltzmann constant. By differentiating the above equation, one may obtain a linearized radiation rate in the perturbation form

$$Q_{rad} = 4\varepsilon\sigma T_{avg}^3 \Theta \tag{2.30}$$

where T_{avg} is the average surface temperature. If this equation is combined with the convective heat rate, then the radiation heat transfer can be incorporated into the above formulation by augmenting the convection coefficient with a correction term as following

$$h' = h + \Delta h \tag{2.31}$$

Where

$$\Delta h = 4\varepsilon\sigma \mathbf{T}_{avg}^3 \tag{2.32}$$

With this correction, both radiation and convection can be incorporated into the overall heat transfer coefficient *h*.

2.2.8 Mesh considerations

In the TEI problem involving two sliding bodies, it is well characterized that there is a thermal skin in the vicinity of the contact surface of the poor conductor [7]. This is because the disturbance moves relatively slowly over the good conductor but with a speed close to the sliding speed over the friction material. As a result, any given location on the surface of the friction material experiences an oscillatory temperature at a very high frequency, which in turn generates very short heat waves in a direction perpendicular to the surface. To describe the temperature field adequately it is essential to use a graded mesh in this region to ensure that enough elements are generated in the thermal skin layer. In reference [7] the criteria were developed to determine the mesh refinement for this purpose and those criteria are equally applicable to the present problem. Based on these criteria a mesh bias ratio of 2.0 has been used in the friction layer and 1.5 in the metal layer, with more elements created towards the sliding interface

2.3 Computational results

2.3.1 Model parameters

The parameters used in the finite element analyses were obtained from the literature [1] and they are tabulated in (Table 2.1) and (Table 2.2). These parameters reflect the realistic clutch and brake systems used in the automotive industry, although the actual values may vary in different applications. Note that in the brake model, a 1/6 coverage, or 60 degrees of pad section was assumed and therefore the equivalent coefficient of friction is 0.4/6 = 0.0667 for the full coverage. Both clutch and brake

models assume an antisymmetric boundary condition along the midplane of the rotor Fig (2.1) because the antisymmetric modes have proved more susceptible to TEI based upon the previous researches. Therefore a half thickness has been used for the metal layer (steel or cast iron) in both models. In all the following discussions, the sliding velocity V is normalized as V* defined by

$$V^* = \frac{Va}{k_m} \tag{2.33}$$

	Steel Disk	**Friction Layer**
Young's modulus, E (GPa)	200	0.11
Poisson's ratio, ν	0.30	0.25
Thermal expansion coefficient ,α($\boldsymbol{K^{-1}}$)	1.2 x 10^{-5}	1.4 x 10^{-5}
Thermal conductivity , K (W$\boldsymbol{m^{-1}K^{-1}}$)	42	0.22
Thermal diffusivity, k ($\boldsymbol{mm^2s^{-1}}$)	11.9	0.122
Thickness (mm)	1.375	0.673
Coefficient of friction	0.12	0.12

Table 2.1: Parameters used in the clutch model.

	Cast iron Disk	**Friction Layer**
Young's modulus, E (GPa)	112.4	2.03
Poisson's ratio, ν	0.25	0.35
Thermal expansion coefficient , α ($\boldsymbol{K^{-1}}$)	1.325 x 10^{-5}	3.0 x 10^{-5}
Thermal conductivity , K (W$\boldsymbol{m^{-1}K^{-1}}$)	57	0.93
Thermal diffusivity, k ($\boldsymbol{mm^2s^{-1}}$)	17.2	0.522
Thickness (mm)	14	10
Coefficient of friction	0.4	0.4

Table 2.2: Parameters used in the brake model.

where a and k_m are the half thickness the thermal diffusivity of the metal disc, respectively. This is consistent with the dimensionless velocity defined in Lee and Barber's work [3]. The convection coefficient h is normalized as Bi, i.e. the *Biot number* defined by

$$Bi = \frac{ha}{K_m} \tag{2.34}$$

where K_m is the thermal conductivity of the metal disc. A convection coefficient of 10,000 W/m^{2}K is equivalent to a *Biot number* of 0.3274 in the clutch model or 2.456 in the brake model being discussed.

2.3.2 Comparisons between linear and quadratic elements

A series of convergence tests were attempted to study the effect of the mesh size on the result. Figure 2.2 shows the critical speed as a function of the element number in the friction layer, for three different wave numbers m=100, 200 and 400.

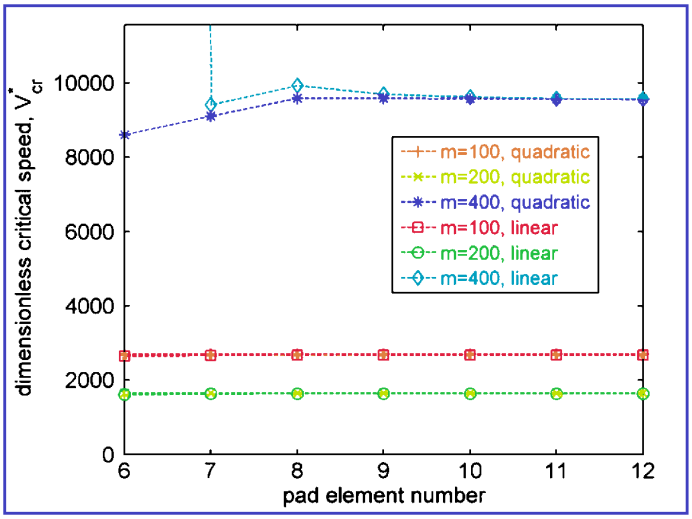

Figure 2.2: Critical speed as a function of the element number in the friction disc (pad) of the clutch model

A comparison has been made between the two finite element types: linear elements and quadratic elements. The element number in the friction layer varies between 6 and 12 in both cases. It can be seen that at lower wave numbers m=100 or 200, there is virtually no difference between the two element types whereas the difference is appreciable when m=400 and when the element number is less than 10. The main reason is that the temperature field oscillates at a higher frequency for shorter wavelengths, thus requiring a finer mesh to capture the variations in the temperature field. In this case use of quadratic elements has an obvious advantage over the linear elements. In fact, when the element number is less than seven, the solution using the linear elements diverges quickly. In contrast the model using the quadratic elements is still capable of yielding an acceptable solution. An inspection on the results shown in Figure 2.3, where the critical speed is expressed as a function of the element number in the steel layer, has revealed a similar trend. That is, the linear elements lead to a solution very close to that obtained from the quadratic elements at lower wave numbers, yet they exhibit a significant difference for higher wave numbers in terms of the convergence speed. For the quadratic elements, a surprisingly accurate result, which deviates merely about 1.5% from the convergent solution at m=400, can be obtained using only one element across the thickness of the metal rotor. Although the computational efficiency is generally not a major concern in the current problem, it has a significant importance for higher dimensions. The previous work showed that the computational time for a three dimensional system is very sensitive to the total DOFs (degrees-of-freedom). The results presented in Fig (2.2) and Fig (2.3) imply that a fine mesh is not always necessary and a

fairly coarse mesh in the metal disc using quadratic elements, for example, is a potential solution to improve the numerical efficiency for problems defined in higher dimensions.

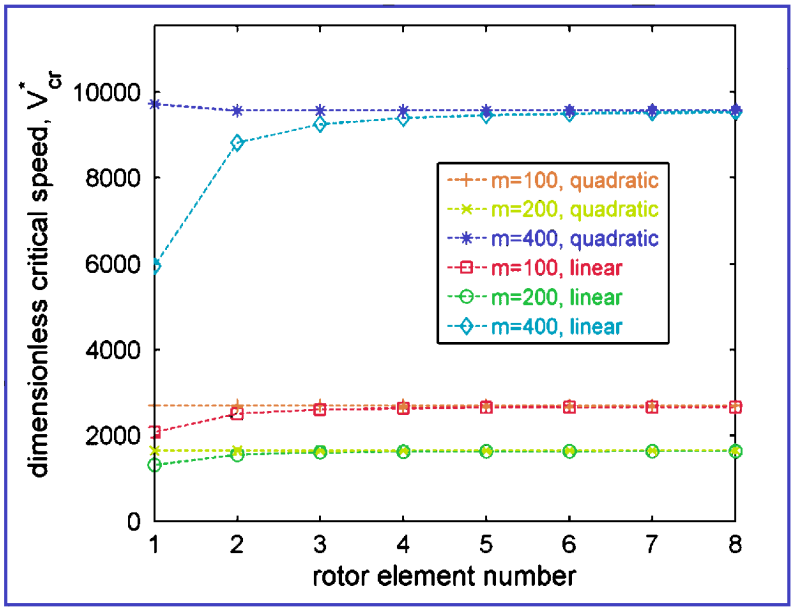

Figure 2.3: Critical speed as a function of the element number in the steel disc (rotor) of the clutch model

2.3.3 Effect of convective cooling on temperature growth rate

To investigate the effect of the convection heat transfer coefficient, the exponential temperature growth rate *b* has been plotted against the sliding velocity *V* in the clutch model using three different values of the convection coefficient when *m* was chosen as 200 Fig (2.4). This value of *m* is approximately located at the lowest critical sliding speed among all wave numbers. The results are presented in an effort to demonstrate the transition of the system from a stable mode to an unstable mode as the sliding speed increases.

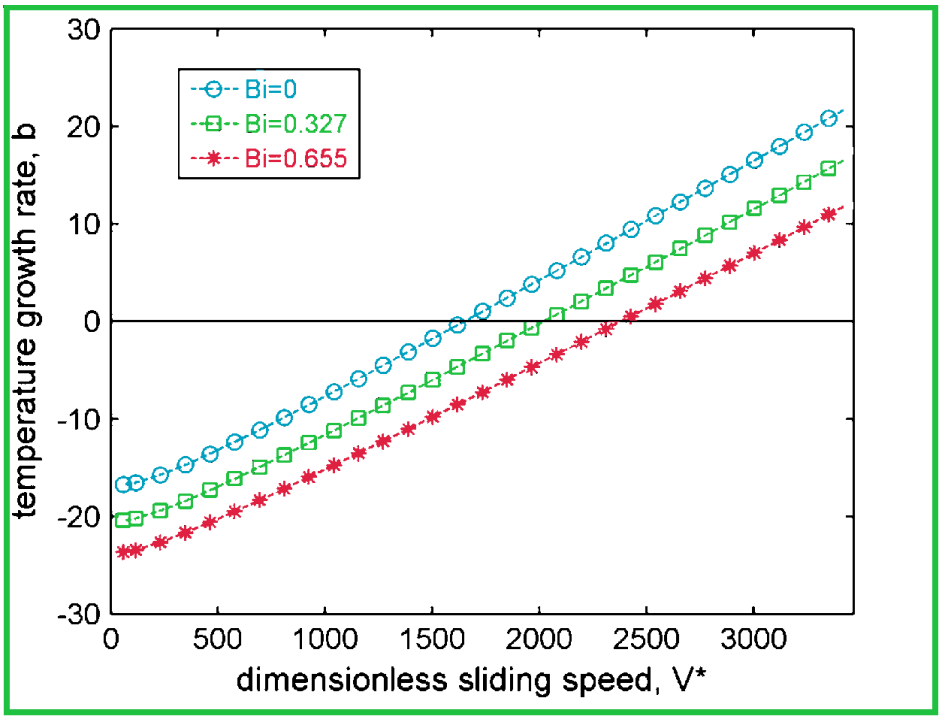

Figure 2.4: temperature growth rate as a function of the sliding velocity in the clutch model for m=200

When the convection heat dissipation is absent, the growth rate is negative at a low sliding speed showing that the temperature perturbation decays with time. When V^* is close to 1,652, the growth rate b approaches zero, which corresponds to a transition stage where the perturbation starts to grow. Beyond that point, the growth rate becomes positive, representing a thermoelastically unstable condition. Therefore this particular location on the horizontal axis corresponds to the critical speed of the system. It appears that the relationship between the growth rate and the sliding speed is almost linear in the unstable region. In the stable region, on the other hand, it starts with a nonlinear profile at a low speed, but becomes nearly linear in the remaining part. This is consistent with the prior results reported in the literature [8]. The addition of a nonzero convection coefficient has apparently shifted the curve to the right side, resulting in an increase in the

critical speed, but it does not alter the overall shape of the curve, i.e. it begins with a slightly nonlinear region and smoothly transits to a nearly linear profile. The three curves shown in Figure 2.4 are approximately parallel to each other. It is estimated that an increase of the convection coefficient by 10,000 W/m^{2}K (Bi=0.327) approximately raises the critical speed by ΔV^*=347 in the current clutch model, or around 20% of the value without convection.

2.3.4 Effect of convective cooling on critical speed

Further, the critical speed was obtained as a function of the wave number *m* under a set of different convection coefficients ranging *h*=0, 10,000, 20,000 and 30,000 W/m^{2}K (i.e. Bi=0, 0.327, 0.655 and 0.982) for the clutch problem, as shown in Fig (2.5). When the convection heat dissipation is absent, the lowest critical speed is located at the dimensionless wave number around *ma*=0.234 with a value of V*=1,537. This is very close to the critical value 1,652 obtained at *m*=200 (i.e. *ma*=0.275) shown in Fig (2.4). The entire curve has been raised by the addition of thermal convection, but the overall shape of the curve does not change much, with the lowest critical speed maintained at the same location of m. Presented in Fig (2.6) is the similar results for the brake model with the lowest critical speed occurring at *ma*=0.532. Unlike the clutch results shown in the previous figure, the *V-m* curve seems to keep changing its shape as the convection coefficient increases. A close look at the data, however, has shown that the wave number corresponding to the lowest critical speed does not change as the convection coefficient increases. An immediate implication of the result is that there should not be any change

in the dominant mode shapes at any given sliding speed, either. That is, the eigenmodes change their *b* values at the same rate as the convection coefficient changes.

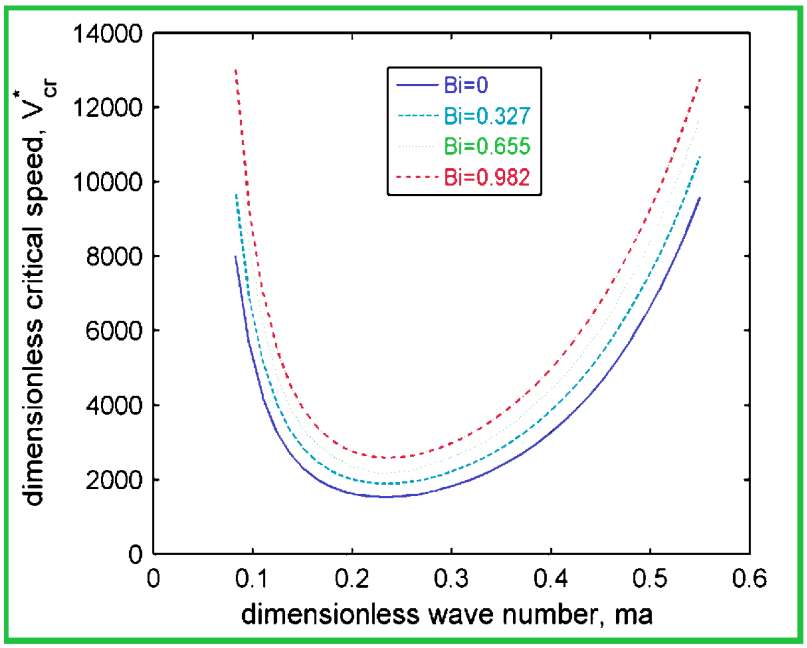

Figure 2.5: Critical speed as a function of the wave number in the clutch model

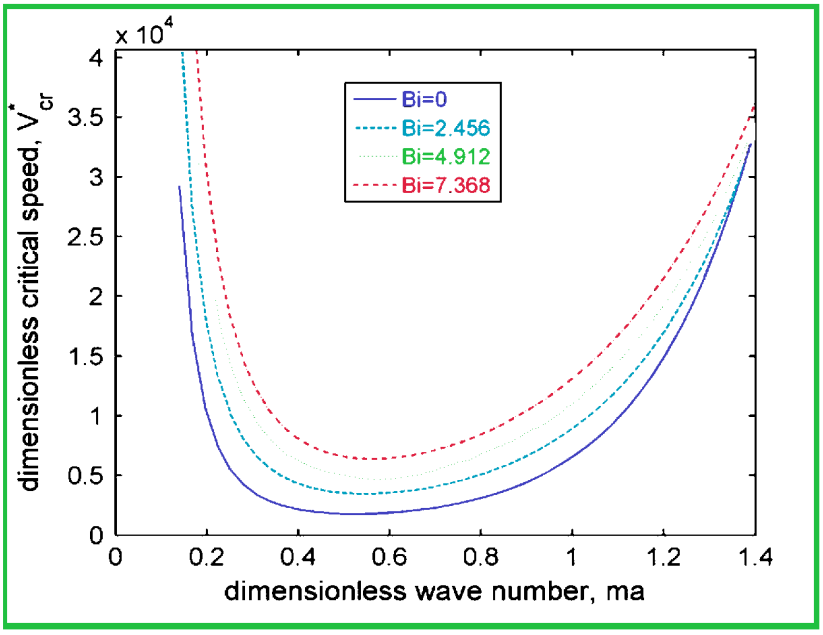

Figure 2.6: Critical speed as a function of the wave number in the brake model

Figure (2.7) shows how the minimum critical speed varies with the convection coefficient under three representative wave numbers *m*=100, 200 and 400 in the clutch model. It can be seen that the critical speed is almost a linear function of the convection coefficient. When *m*=100, the critical speed changes from V*=2,692 at *h*=0 (Bi=0) to V*=4,553 at *h*=30,000W/m^{2}K (Bi=0.982), with an approximately 69% increase.

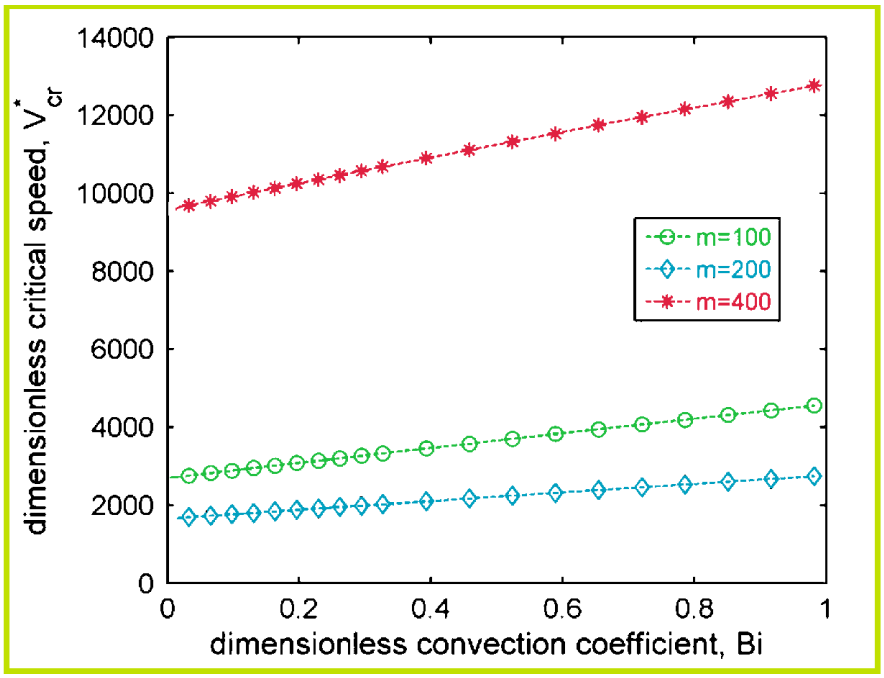

Figure 2.7: Minimum critical speed as a function of the convection coefficient in the clutch model.

In terms of percentage change this is the maximum among the three curves in Figure (2.7). For example, at *m*=400 the change in the critical speed is from V*=9,579 to 12,756, with an approximately 33.2% increase. A similar conclusion can be drawn from the brake model, as shown in Figure (2.8). The four curves representing *m*=20, 40, 60 and 80 shown in the figure have different slopes, implying different degrees of dependence of the critical speed on the convection rate. This dependence is the strongest at the lowest

wave number (m=20) among the four. Compared to the clutch model this time the difference is even more drastic: the critical V*=4,233 at h=0 (Bi=0) versus V*=14,651 at h=30,000 W/m^{2}K (Bi=7.368). That is equivalent to an increase of 246%. At m=40 where the critical speed almost reaches the valley in the *V-m* curve, it is found that the critical speed changes from V*=1,799 to 6,390 when h varies from 0 to 30,000 W/m^{2}K (Bi=0~7.368), or an approximately increase of 255%. In fact, even with h=1000 W/m^{2}K (Bi=0.246), the increase in the critical speed for m=40 is as much as 10.4% in comparison with the result at h=0, which is a non-negligible difference. On the other hand, at m=80, percentage change of the critical speed is close to 65% for the full range of the convection coefficient. Therefore it has been seen that the effect of convection coefficient is more significant for the Eigenmodes with shorter wave lengths.

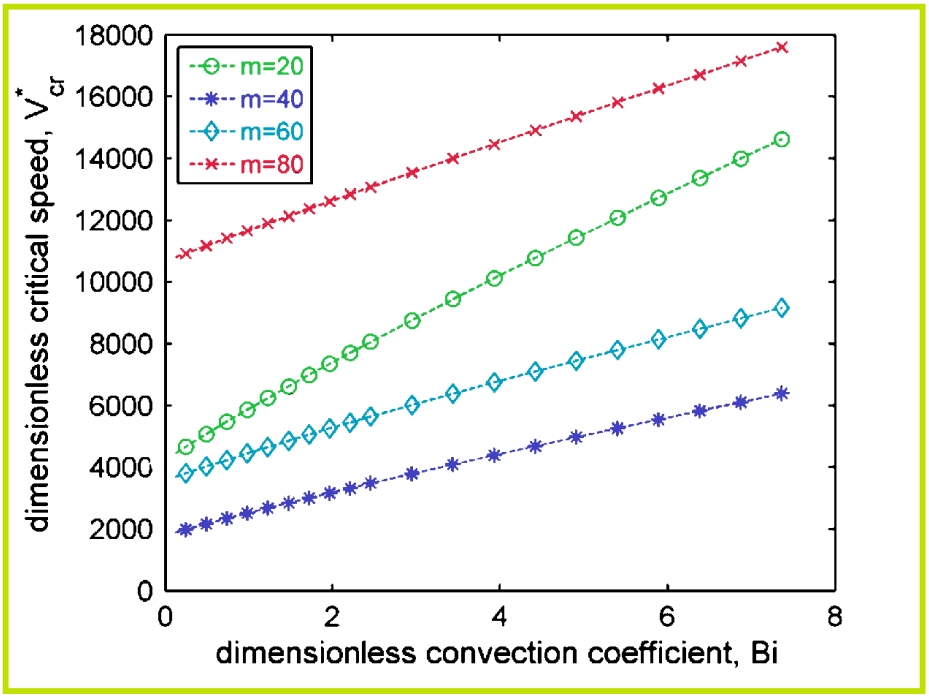

Figure 2.8: Minimum critical speed as a function of the convection coefficient in the brake model.

2.3.5 Effect of radiation cooling

Figure (2.9) shows the equivalent coefficient Δh as a function of the surface temperature under the different values of thermal emissivity ε ranging from 0.2 to 1.0, based on Eq. (2.32). Clearly, the thermal radiation rate is much less significant than convection. Even with ε=1 and T_{avg}=1500K, the equivalent coefficient Δ*h* is still below 1000 W/m^{2}K (i.e. ΔBi<0.0327 in the clutch model or ΔBi<0.246 in the brake model), which is an order of magnitude less than the convection coefficients of common liquids. With a practical disc surface temperature around 500 °C and a realistic thermal emissivity of the material, it is found that Δ*h* is well below 100 W/m^{2}K. Therefore the effect of thermal radiation on TEI is usually negligible compared to convective cooling.

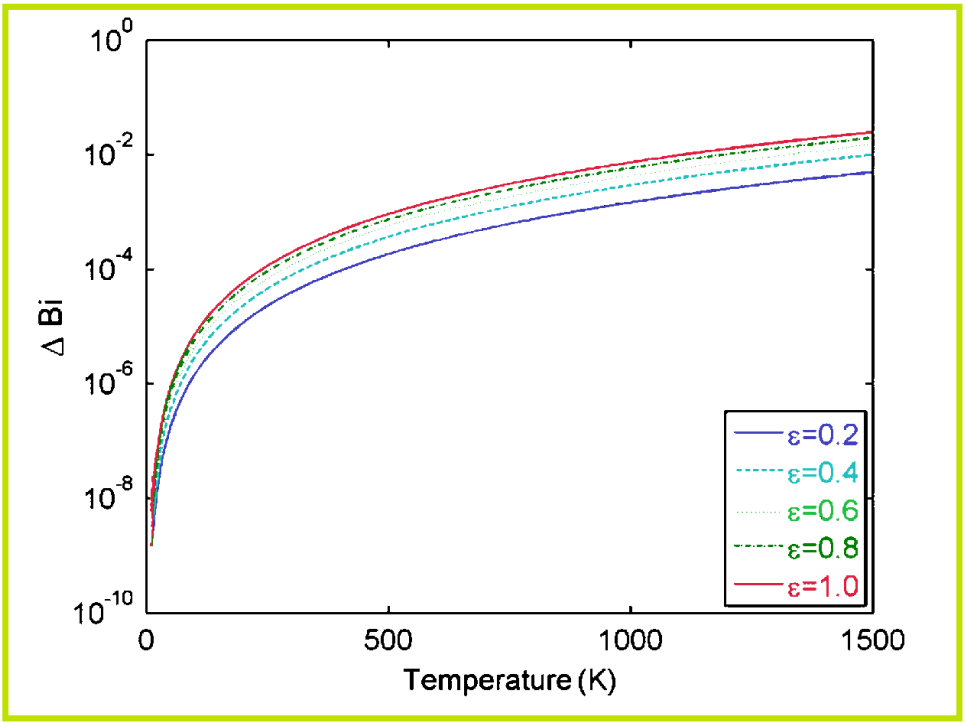

Figure 2.9: Equivalent Biot number for thermal radiation as a function of the surface temperature.

2.4 Conclusions

A finite element method is implemented to investigate the effect of convective cooling on the stability boundaries of thermoelastic instability in a couple of representative brake and clutch systems. By adding a negative term representing the convective heat dissipation to the frictional heat generation rate, convective cooling is successfully incorporated into the finite element formulation. This is analogous to a system with a reduced frictional heat rate, and therefore can stabilize the thermal-mechanical process. As a consequence it has been found that the previous analyses on TEI typically overestimated the critical sliding speeds. Liquid cooling such as water and lubricants removes heat at a much faster rate than gases such as air, and therefore affect the system stability more significantly. The parametric studies have shown that the critical speed in some cases where the system is cooled by water can be three times as high as the value without convective cooling. However, the wave number corresponding to the lowest critical speed is nearly independent of the convection effect. This implies that the dominant mode pattern at a given sliding speed remains unchanged as well. Further, in comparison with the linear elements, the quadratic elements are capable of accurately capturing the oscillatory patterns of the temperature in the vicinity of the friction interface, and therefore provide a better numerical accuracy with the same computational effort. Although using quadratic elements is not necessary in lower dimensions, it will potentially permit efficient solutions for problems defined in higher dimensions.

CHAPTER 3

Finite Element Analysis of Thermoelastic Instability in Intermittent Sliding Contact

3.1 Introduction

Thermoelastic instability (TEI) theory states that in frictional sliding systems such as disk brakes or clutches, the thermal-mechanical feedback can be unstable if the sliding speed exceeds a certain threshold [19]. The theoretical models were developed over the past decades to investigate the phenomenon, both analytically [20] and numerically [21], using either the eigenvalue formulation [22] or transient simulation [23], the former of which assume a perturbation of the solution in the exponentially growing form, and an eigenvalue equation is constructed from the governing differential equations. The growth rates of the variables, and further the critical sliding velocity, can then be recovered from the eigenvalues of the equation. The majority of these works assume coextensive contact, especially for clutch systems, due to the fact that they have annular geometries, moving continuously in the circumferential direction. Many other sliding surfaces, such as those in disk brake systems, are not coextensive as the brake pads do not cover the entire rotor surface, and the material points on a surface always experience alternating periods of contact and separation. For

axisymmetric plates in clutches, intermittent processes are also possible, e.g., in the presence of initially uneven surfaces as a result of surface separation, manufacturing imperfection, or misalignment of the axles during mounting.

These intermittent processes can be expected to alter the stability boundaries of the TEI problem. Barber et al. [24] suggested us to allow for the intermittent contact in TEI by averaging the heat input over the circumference. This strategy was later reiterated by some other researchers, such as Hartsock and Fash [25]. However, the hypothesis was not verified until Ayala et al. [8], who explored a simplified intermittent contact problem in which an infinite, conductive material slides against a rigid nonconductive surface. Their results show that at a low Fourier number, i.e. when the thermal transient is much longer than the period of one revolution, the method by averaging the frictional heat input over the circumference works fairly well, and the critical speed is an inverse linear function of the proportion of time in sliding contact. However, at higher Fourier numbers the critical speed becomes lower, although the dependence of the critical speed on the Fourier number becomes relatively weak.

These conclusions, however, were based on the assumption that the friction material is rigid and nonconductive, and that the other material has an infinite extension. Realistic geometries do not satisfy these idealized conditions. Prior researches on continuous contact revealed considerable differences between the half-plane solutions and the models with finite dimensions and real materials [9,28]. It is not clear at this point whether the same conclusions obtained from the idealized

half-plane solutions equally work for more realistic systems involving finite geometries with both materials being deformable and conductive.

The analytical approaches have proved difficult in handling this type of problems due to the demand for numerical convergence and iterations, which are sometimes computationally prohibitive. The finite element method developed by Yi et al. [7] is therefore a preferable tool, and the present work is devoted to solving the intermittent contact problem using the same strategy. It should be pointed out that some preliminary discussions on this issue can be found in the literature [30]; however, a systematic exploration of the problem including the method validation has never been attempted.

3.2 Finite Element Models

3.2.1 General Formulation

We assume a two-dimensional configuration to approximate a brake or clutch. The circumference of a brake or clutch disk is spread out along the sliding direction, and the effect of the radial thickness is ignored in our model. The solution method follows the standard procedure for the problems in this category [7]. Briefly one can start from the governing equations of heat conduction, thermoelasticity and frictional heat generation. It is followed by a search for the constant speed solution in linear perturbations that grow exponentially in time. For the temperature field, the perturbation solution can be written as

$$T(x, y, t) = T_0(x, y) + \Re \{e^{bt} T_1(x, y)\} \tag{3.1}$$

Where T_0 is the steady-state solution, b is a complex exponential growth rate. $\Re$ represents the real part of a complex number. The amplitude of oscillation T_1 is typically complex to reflect the change in the phase angle of temperature across the thickness. Similar assumptions in the perturbation form can be made on other key variables including the displacement and the contact pressure. A direct result from the perturbation assumption is that time is eliminated from the governing equations, leading to a generalized eigenvalue equation in the following matrix form after an implementation of the finite element method:

$$\mathrm{M}\Theta = b\mathrm{H}\Theta \tag{3.2}$$

Where Θ is the nodal temperature vector; M and H are the coefficient matrices determined from the material properties and the finite element shape functions.

Given appropriate boundary conditions the critical speed can be determined from the sliding speed at which the real part of the growth rate is zero. Notice that in the above formulation, the wave number (i.e., the number of higher temperature regions in the sliding direction) is not a predefined parameter. Rather, it is a result obtained from the computed eigenfunctions. Therefore the method can be used to solve problems for both continuous and intermittent contacts. The details on the matrix derivations are omitted here, as they are modified versions of those used in the finite element scheme previously developed by the Yi et al. [7]. In intermittent contact the critical speed is presented as a function of the Fourier number, which is defined by

$$F_0 = km^2t_0 \tag{3.3}$$

Where $m = \frac{n}{r}$, $t_0 = \frac{L}{V}$ (3.4)

Here, n is the total number of waves in the circumference; r is the radius of the rotating disk, L is the circumferential length; V *is* the sliding velocity.

3.2.2 Two-Dimensional (2-D) Finite Element Model

In the 2-D finite element model, the mesh is generated uniformly in the sliding direction, but biased towards the contact surfaces in both materials. The implementation of the quadratic element type more accurately approximates the nonlinear distributions of temperature in both thickness and longitudinal directions, and it can thus improve the numerical efficiency. The total length of the model in the *y*-direction is set to the circumferential length of the disk. In a continuous contact situation, both layers in contact are coextensive with the same length, whereas in an intermittent contact the friction layer has a reduced length see Figure (3.1).

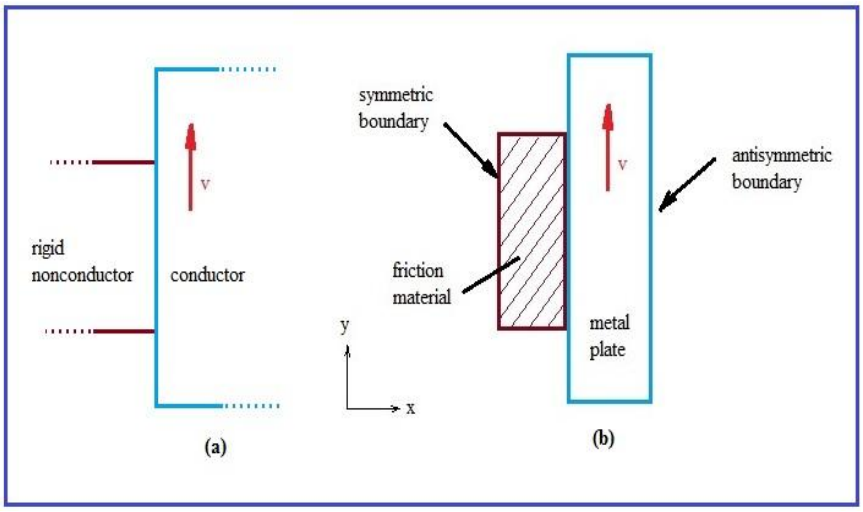

Figure 3.1: Schematic of the intermittent contact model: (a) a conductive half plane sliding against a rigid nonconductor, and (b) a conductive plate of finite thickness sliding against a deformable and conductive surface

The frame of reference is fixed to the friction layer to ensure that the problem has a fixed boundary as opposed to a moving one, which is mathematically more difficult to handle. A cyclic boundary condition, i.e., all the quantities on one end are assumed to be the same as those on the other end, is applied to the conductive layer in the direction of sliding to model the closed disk ring configuration. Notice that there are no constraints applied on the ends of the friction pad in the direction of sliding. To simplify the model, the symmetric-antisymmetric boundary conditions are assumed across the thickness see Figure (3.1), with the symmetric condition specified on the poor conductor (i.e., the friction material) and the antisymmetric condition on the good conductor (i.e., the metal plate), due to the fact that this mode pattern has been found dominant in many practical applications. Particularly, on the symmetric boundary

$$q_x = 0; \quad u_x = 0; \quad \sigma_{xy} = 0 \tag{3.5}$$

And on the antisymmetric boundary,

$$T = 0; \quad u_y = 0; \quad \sigma_{xx} = 0 \tag{3.6}$$

Where *u*, *q*, and *a represent* the displacement, heat flux and stress, respectively. It should be reiterated that the wave number is not predesignated in the two-dimensional model, nor a monotonic function of the sliding speed. Therefore iterations are required to determine the critical speeds and the associated wave numbers. More specifically the critical speed is sought on the basis of the following procedure:

1. The analysis is performed at a number of different sliding speeds with a

prescribed interval, and the growth rates of temperature at each sliding speed are computed.

2. The wave number associated with each growth rate *b* is determined by the Fast Fourier Transform (FFT) technique. This is not a trivial part of the work since the sinusoidal profiles of the eigenfunctions in continuous contact become highly distorted when intermittent contact is involved.
3. The growth rates of temperature for each wave number at the different sliding speeds are sorted following the above two steps. Three successive sliding speeds with positive growth rates are then identified.
4. The value of the sliding speed at zero growth rates, i.e., the critical speed for each wave number, is extrapolated by quadratic curve fitting on the basis of the three different pairs of growth rate and sliding speed.

3.2.3 Fourier Model for Continuous Contact

The one-dimensional Fourier finite element model serves for the validation and convergence study of the continuous contact solution. It is constructed in a way similar to the one used in Yi [31]. The model is discretized in the thickness only and each node has two degrees of freedom along the x- and *y*-directions. The wave number appears in both stiffness and thermal matrices in the finite element equations. The cyclic boundary conditions and coextensive contact are the intrinsic features of the model. Therefore the computational effort is minimized in the Fourier model as the finite element discretization is not needed in the direction of sliding.

3.2.4 Nonconductive Rigid Friction Plate

To consider the extreme situation where a conductive half plane slides against a rigid nonconductive surface in the finite element models, a sufficiently large thickness equal to the circumferential length of the disk is assumed in the conductive material so that the boundary effects are minimized. Meanwhile the elastic modulus of the insulating material is set to value five orders of magnitude higher than that of the conductive material, and a single element is used across the thickness of the insulator. Other parameters remain unchanged.

3.3 Analytical Models for Comparison

3.3.1 Continuous Contact

Burton et al. [32] showed that for plane strain, the critical speed of a conductive surface sliding against a rigid nonconductive surface is linearly proportional to the wave number according to

$$V_c = \frac{2Km(1-v)}{E\alpha f} \tag{3.7}$$

where K is the thermal conductivity; m is the wavenumber per 2π of length; E, α, v, f are Young's modulus, the coefficient of thermal expansion, Poisson's ratio and the coefficient of Coulomb friction, respectively.

3.3.2 Intermittent Contact

For a conductive half plane sliding against a rigid nonconductive surface, we define the following dimensionless velocities following Ayala's notations [26]:

$$V^* = \frac{V}{km} \tag{3.8}$$

Where *V is* the critical sliding velocity in the intermittent contact, and

$$V_0 = \frac{V}{km} \tag{3.9}$$

We further define a dimensionless speed $\hat{V}$ by taking the ratio of V^* to V_0.

$$\hat{V} = \frac{V^*}{V_0} = \frac{V}{V_c} \tag{3.10}$$

It was shown [8] that at sufficiently small F0 << 1,

$$\hat{V} \rightarrow \frac{1}{R_1} \tag{3.11}$$

Namely, the critical speed is the same as that of a system in continuous contact with the heat generation rate replaced by the average rate during the intermittent process. Detailed numerical studies show that the critical speed differs from that predicted from Eq. (3.11) by less than 1% for $F_o < 0.1$.

As $F_o \rightarrow \infty$, it is found that

$$\hat{V} \rightarrow \frac{1+\sqrt{R_1}}{2R_1} \tag{3.12}$$

Where R_1 is t_1/t_0, i.e., the ratio of the contact period to the overall time. For large but finite Fourier numbers, one has to solve a nonlinear equation in the following form for b^*, the dimensionless growth rate:

$$e^{(b^*R_1-R_2)F_0} \times \left[\sqrt{1+b^*}\, e^{R_2F_0} erfc\left(\sqrt{R_2F_0}\right) - e^{(1+b^*)R_2F_0} erfc\left(\sqrt{R_2F_0(1+b^*)}\right)\right] = \frac{b^*}{1+\sqrt{1+b^*}} \tag{3.13}$$

from which $\hat{V}$ can be computed from

$$b^* = \frac{1}{2}\left[4\hat{V} - 1 - \sqrt{8\hat{V}+1}\right] \tag{3.14}$$

Notice that "*erfc*" in Equation (3.13) is the complementary error function. Equations (3.11) through (3.14) are adapted from Ayala's solutions [26].

3.4 Results

3.4.1 A Conductive Half Plane Sliding Against a Rigid Nonconductive Surface

Continuous contact. This is a limiting case of intermittent contact with the contact ratio $R_1 = 1$. In continuous contact it is expected that the one-dimensional Fourier finite element model yields the same result as Burton's solution. In Figure (3.2) clearly $\hat{V}$ of the Fourier model remains at 1.0 for the entire range of F_o. The Fourier number covered in the range corresponds to the wave number n = 1−20, or m = 6.25−125 when the disk radius r is set to 0.16 m. A convergence study for the two-dimensional finite element model is also shown in the same figure. It converges to unity at lower F_o but deviates from unity at larger F_o. We found that 24 elements in the circumference result in a maximum numerical error of approximately 20%.

In fact, when n = 20, each wave is covered by only one element, hence inadequate to delineate the profile of the Eigenfunction at larger wave numbers. On the other hand, when the element number increases to 40 or 60, a much better accuracy is obtained. For example, with the total element number of 60, the maximum numerical error obtained is less than 1%. We conclude that the two-dimensional finite element model for continuous contact must be discretized in such a way that each wave is covered by at least two or three elements in order to achieve a desirable accuracy in the solution. In the preceding results, 12 biased

elements with a bias ratio of 2.0 in the thickness direction of the conductive material have been found sufficient to capture the rapid change in the temperature gradient in the thickness.

Intermittent Contact. The plane finite element model was also compared to Ayala's solution when the contact is intermittent. We did not reproduce the entire analytical solution; however, the results in the three limiting cases represented by Eqs. (3.11), (3.12), and (3.14) are believed to be sufficient for the purpose of comparison and validation. In the finite element model for intermittent contact, the metal layer has been divided into as many as 90 elements in the direction of sliding, so that the contact region is covered by sufficient elements.

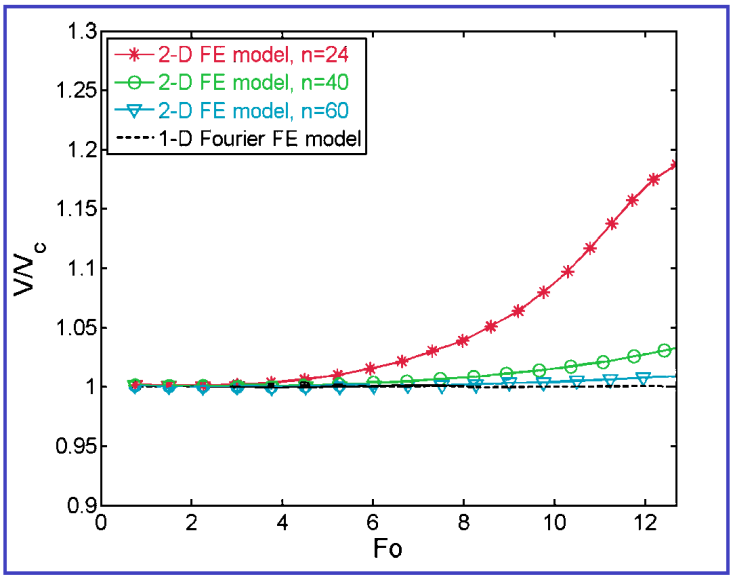

Figure 3.2: Convergence studies of the finite element models for continuous contact, assuming a conductive half plane sliding against a rigid nonconductor.

The thickness is divided into 12 elements. Figures (3.3 a, b, and c) show the finite element solutions for three different contact ratios 1/2, 1/3, and 1/6,

respectively. Clearly, in all three scenarios, the results are bounded between the analytical solutions given by Eq. (3.11) and Eq. (3.12). To the right side of the figures when F_o increases, the curves gradually approach the asymptotic solutions for $F_o = \infty$. When R_1 is reduced, the figures show a reduced range of F_o, e.g., the maximum F_o is 2.8 when R_1 = 1/6 as opposed to 8.2 when R_1 = 1/2. This is because the raised critical sliding speed as a result of the reduced R_1 leads to a reduction in the total period of sliding process, and thus a decreased Fourier number.

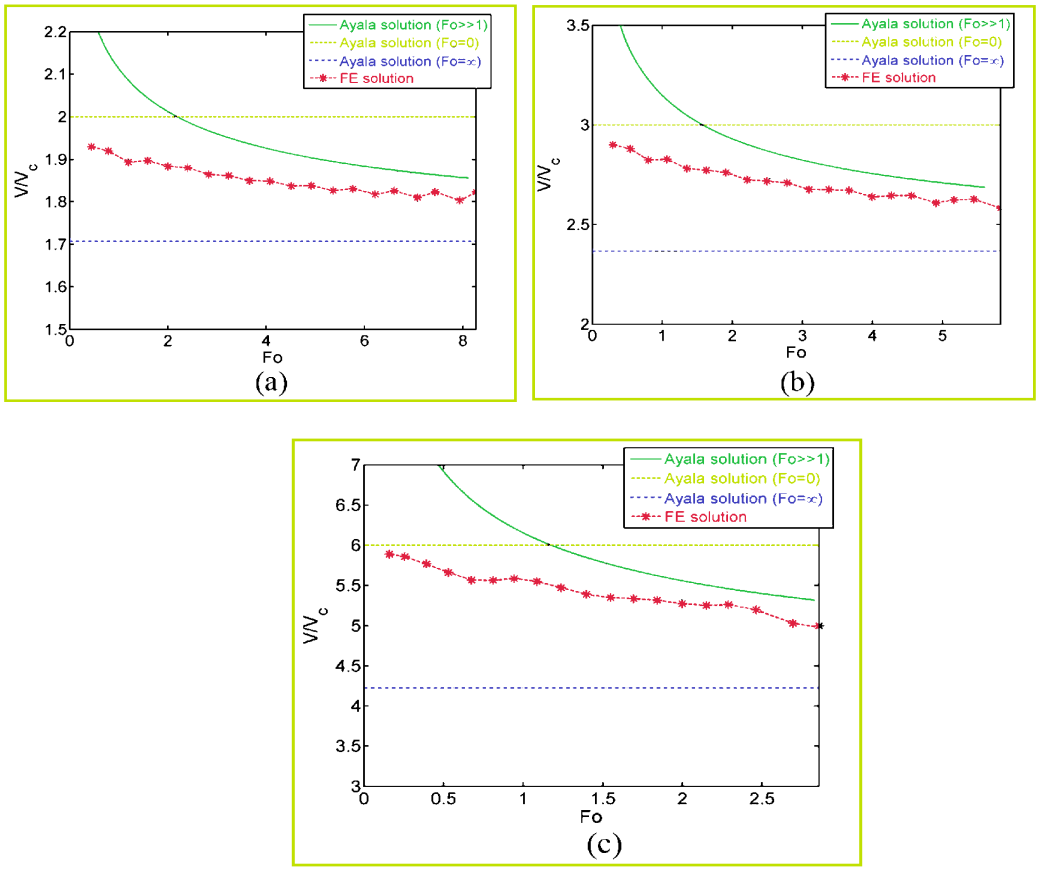

Figure 3.3: Finite element (FE) solutions for three different contact ratios (a) R_1 = 1/2, (b) R_1 = 1/3, and (c) R_1 = 1/6. A conductive half plane sliding against a rigid nonconductor is assumed.

3.4.2 Two Conductive Plates with Finite Thickness

Continuous Contact. For the continuous contact problem of two conductive, deformable plates with finite thickness, we compared the computational results between the two finite element models: (A) the full two-dimensional finite element model with both thickness and length directions discretized, and (B) the one-dimensional Fourier model defined in the thickness direction only. The parameters used in the finite element analysis are shown in Table 1. The element numbers used in the length and thickness of model A are 50 and 20, respectively. Notice that both materials are conductive now and hence both need to be divided into biased elements through the thickness. We define the dimensionless velocity in the following way:

$$\tilde{V} = \frac{V}{V_f} \tag{3.15}$$

where V and V_f are the critical speeds determined by model A and B, respectively. During the calculation of V_f in the continuous contact model, the time-averaged frictional heat input (i.e., the coefficient of friction divided by R_1) is already taken into consideration. The dimensionless wave number here is defined as following Lee and Barber's notation [33].

$$A = ma \tag{3.16}$$

The reason to change the definition of the dimensionless wave number is that the Fourier number $\boldsymbol{F_o}$ defined previously is no longer a monotonic function of the wave number $\boldsymbol{m}$ when the disk has a finite thickness. Figures 3.4(a) and (b) show the dimensionless critical speed based on Lee's notation and the definition in Eq. (3.15), respectively. It can be seen from Figure 3.4(b) that the full 2-D model

agrees quite well with the Fourier model, with a maximum numerical error around 5%. The contour plots in Figure (3.5) display the temperature distribution with an exaggerated thickness. There is a noticeable change in the phase angle across the thermal skin layer of the poor conductor. This observation is consistent with the prior research on the subject.

Intermittent contact. Now we turn our attention to the realistic situation in which both surfaces in intermittent contact are deformable and conductive. Figure (3.6) shows an example of the finite element mesh used in the computation for $R_1 = 1/3$. The model consists of 48 elements in the sliding direction and 24 elements through the thickness. For smaller values of R_1 such as 1/6, an element number up to 60 is used in the direction of sliding to ensure that the contact region is covered by sufficient elements. The computation is performed iteratively at 20 different sliding speeds with a uniform spacing to search for the critical values of the speed.

	Metal (cast iron)	Friction material
Young's modulus, E (GPa)	112.4	2.03
Poisson's ratio, v	0.25	0.35
Coefficient of thermal expansion, $a\,(\mathrm{K}^{-1})$	1.325×10^{-5}	3.0×10^{-5}
Thermal conductivity, K (W m^{-1} K^{-1})	57	0.93
Thermal diffusivity, k (mm^2 s^{-1})	17.2	0.522
Thickness (mm)	14	10
Coefficient of friction	0.4	0.4

Table 3.1: Parameters used in the intermittent contact model with both surfaces conductive and deformable

Figures 3.7(a) and (b) are the results for the intermittent contact model with both materials being conductive and deformable. Figure 3.7(b) indicates that the

continuous contact model with the time-averaged frictional heating always overestimates the critical speed, which is consistent with the conclusion from the prior analytical studies. However, Figure (3.7) reveals several new features that are quite different from the half-plane solution. First of all, the dimensionless speed V is no longer a monotonic function of the wave number. At smaller wave numbers the result is approaching zero rather than converging to Ayala's solution($\widetilde{V} = \widetilde{V}\ R_1 = 1$).

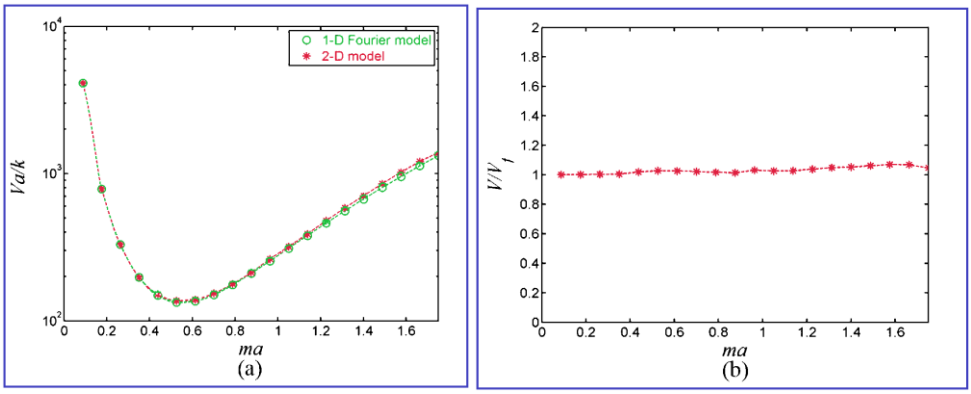

Figure 3.4: Dimensionless critical speed based on (a) Lee and Barber's definition [15] and (b) the definition given in Eq. (15). A conductive half plane sliding against a rigid nonconductor is assumed.

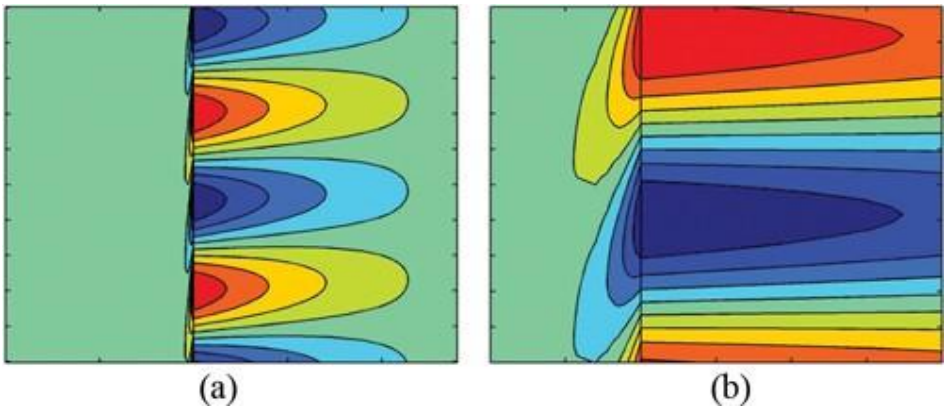

Figure 3.5: Temperature eigenfunction in continuous contact with the thickness exaggerated: (a) the entire model; (b) an enlarged local region on the sliding interface.

There exists a peak value on the curve (it is actually corresponding to the lowest value of the dimensional critical speed) where the two solutions are the closest. Particularly, when R_1 < 1/2, i.e., the period of contact is longer than the period of separation, applying the time-averaged heat input in the continuous contact model yields an error less than 10%. When R_1 = 1/3, the error becomes approximately 20%. The error is even more significant when the contact ratio is reduced further. The location of *ma* at the peak value is dependent on R_1 and it shifts slightly to the left when R_1 is reduced. Moreover, at larger wave numbers, the critical speed does not converge to Ayala's solution, either. This can be seen from a comparison between the results shown on the right side of Figure 3.7(b) and Eq. (3.12) that indicates

$$\widetilde{V} = \widetilde{V}R_1 \rightarrow \frac{\left(1+\sqrt{R_1}\right)}{2} \tag{3.17}$$

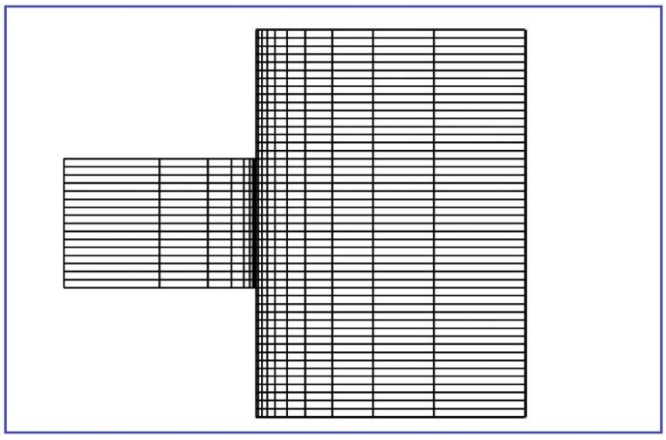

Figure (3.6) A biased finite element mesh generated for the model with R1 = 1/3. Both sliding surfaces are conductive and deformable. The thicknesses of both layers are exaggerated.

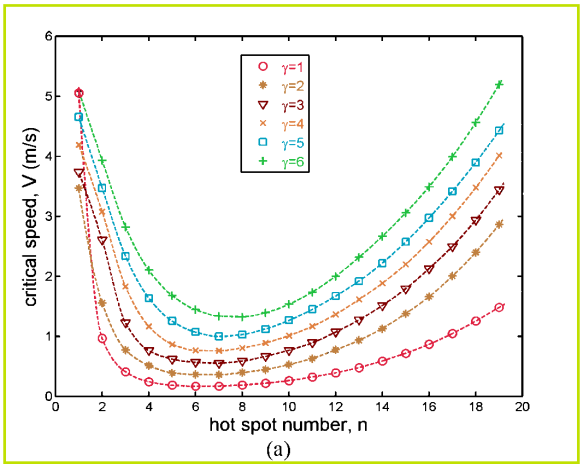

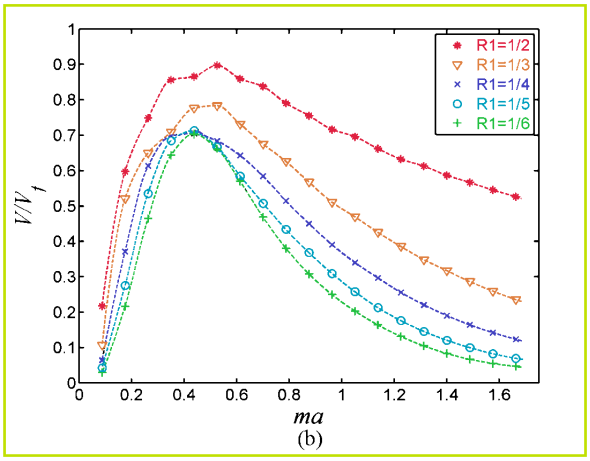

Figure 3.7: critical speed in intermittent contact as a function of the wave number, where γ is the reciprocal of the contact ratio, or 1/R1 . Vf is the critical speed in the continuous contact model, with the time-averaged frictional heat input considered.

For instance, when R_1 = 1/2, the finite element model gives V = 0.5V, which is much lower than Ayala's solution around 0.85. It is found that for a smaller value of R_1, the deviation of the result from Ayala's solution is even more pronounced. In fact, Ayala's solution always overestimates the critical speed, which is not surprising because of the significant difference in the fundamental assumptions related to the geometrical configurations and materials involved in the two models.

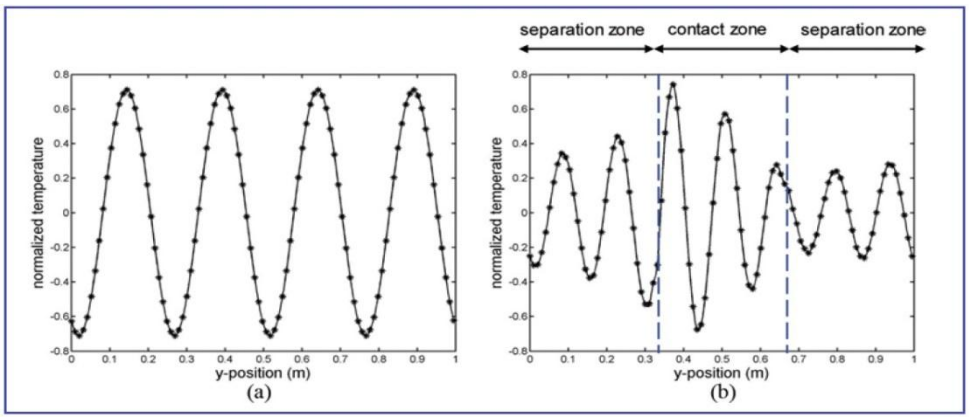

Figure (3.8) Representative Eigenfunctions of temperature in (a) continuous contact and (b) intermittent contact with R1 = 1/3.

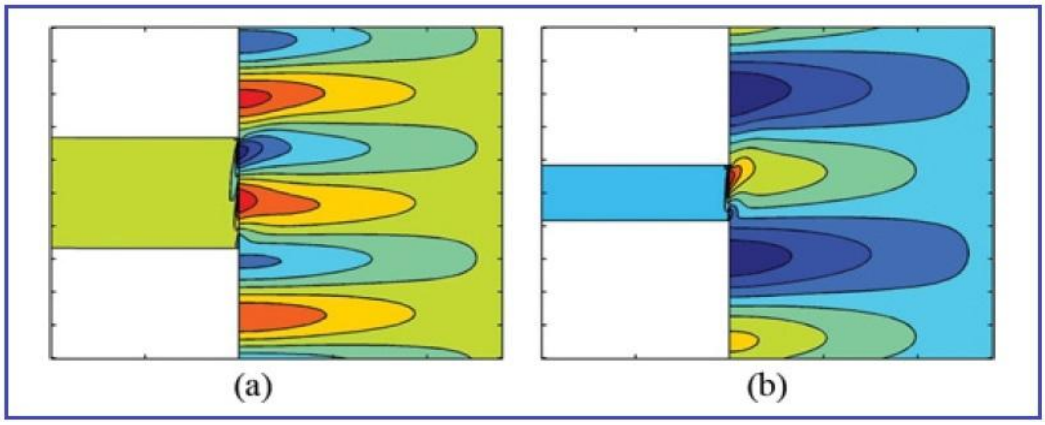

Figure (3.9) Eigenfunctions of temperature for intermittent contact with the contact ratio (a) R1= 1/3 and (b) R1= 1/6, presented in the form of contour plots. The thicknesses of both layers are exaggerated.

The Eigenfunction of temperature shown in Figure 3.8(b) exhibits two distinct zones where the amplitude of oscillation either rises or decays, corresponding to the contact zone and the separation zone, respectively. Thermally, these periods are associated with the periods of frictional heating that alternate with the periods of conductive cooling. In steady state when the growth rate is

zero, the increased temperature variation due to frictional heating during the contact period is counteracted by the reduced amplitude in the separation period.

In contrast, the continuous contact model exhibits no such variations in the amplitude as seen in Figure 3.8(a). The temperature distribution is also presented in the contour plots in Figure 3.9 where the contact ratios are $R_1 = 1/3$ in (a) and $R_1 = 1/6$ in (b). It is seen that the otherwise homogeneous distribution of temperature along the contact interface becomes disturbed. A closer inspection on the eigenfunctions reveals that the temperature distribution is severely distorted near the contact/separation points where the stress concentrations are located.

3.5 Conclusions

The finite element scheme based on the eigenvalue method is implemented for the analysis of thermoelastic instability in intermittent sliding contact with practical model parameters. A numerical algorithm is developed to determine the critical velocities by tracking the Eigenmode patterns and the corresponding growth rates. The method has been validated by both analytical and numerical solutions in some limiting situations. It is concluded that when the realistic materials and geometric configurations are considered for intermittent contact, neither the strategy of time- averaged heat input nor the analytical solution derived from the half-plane model works properly.

The finite element analysis reveals a bell-shaped relationship between the dimensionless critical speed and the wavelength: for longer waves the dimensionless critical speed approaches zero rather than unity; for shorter waves the critical speed

is much lower than that predicted by the analytical half-plane solution. There exists a location where the dimensionless critical speed is the maximum. In general, the strategy by averaging the heat input over the entire circumference is appropriate only when the period of frictional contact is longer than the period of separation, and when the peak value of the dimensionless critical speed is our primary concern.

CHAPTER 4

Buckling of Cylindrical Disk Due to Thermal Stress

4.1 Introduction

Mechanical systems containing durable, moving parts that are in close contact have been extremely common. This contact results in friction, which generates heat. Some systems ignore this situation, assuming it as a natural consequence of the materials and operations involved. For other systems, such as disc brake systems on modern vehicles, friction and the heat which it generates are desired and intended consequences. In disc brake systems, kinetic energy of moving wheels is absorbed through frictional forces by discs and pads where it is converted into heat and dissipated by convection cooling. Ideally, this cooling would be instantaneous so as not to allow heat buildup on the surface of the disc. However, real materials and mechanics do not permit such idealism. Disturbances due to operation and inconsistent materials, along with the particulars of system design may alter what would otherwise be a uniform pressure distribution. This causes inconsistent heat distribution and eventually non-uniform thermoelastic distortion resulting in an even-further altered pressure distribution. If the sliding speed between frictional materials is sufficiently high, the thermal-mechanical feedback process becomes unstable, leading eventually to the localization of the heat load in a small region of the nominal contact area of the sliding surfaces. This phenomenon,

known as thermoelastic instability, was first discovered and explained by J.R. Barber in his article on sliding systems involving frictional heating (Barber 1969).

If the sliding speed within a disc system exceeds a critical value, thermoelastic instability may occur. When a small perturbation in the system leads to an exponential growth in local temperature or contact pressure due to thermal–mechanical feedback, this is in what are known as “hot spots”. For many disc systems, such as a disc brake system, to function appropriately, it is important to prevent the formation of such hot spots that quickly lead to overall system deterioration. Because hot spots form as a result of material choices and system configuration and operation, the prevention of formation of hot spots is dependent upon understanding the conditions in which they are produced. From the disassembly of affected systems, it is evident that the thermoelastic distortion due to irregular expansion and contraction is a cause or consequence of the formation of hot spots. What may not be evident from disassembled systems is the distribution of temperatures and perturbations that led to thermoelastic distortion.

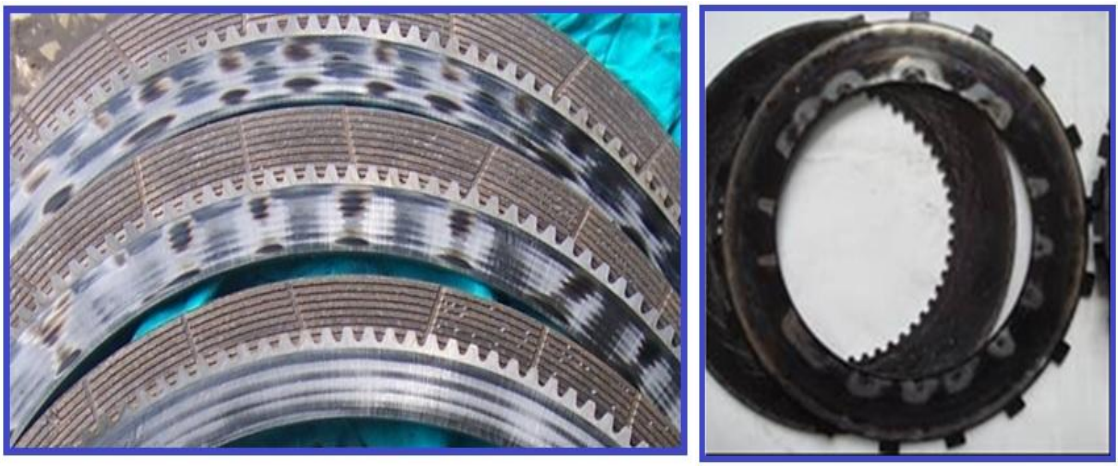

Figure 4.1: Hot spots in a disk brake system

From the physics and mechanics of common disc systems, it is clear that non-homogeneity of the temperature field inside friction discs causes thermal stresses to occur. In order for distortion to result, these stresses must be non-uniform. In support of this conclusion, disassembled systems often show discs found to be permanently deformed out-of-plane [34, 35]. This deformation commonly takes one of the two modes: "cone" or "potato chip". The "cone" mode is evident when the out-of-plane deformation is axisymmetric, resulting in a truncated conical surface [35, 36] like that shown in Figure (4.2). The "potato chip" mode is evident when the out-of-plane deformation is sinusoidal in the direction of the circumference, resulting in a saddle shape similar to that of a potato chip like that shown in Figure (4.3). A wave-number N is associated with the modelling of this particular type of distortion with N=2 in the case of a potato chip deformation. The two deformation modes show very distinct patterns of distortion related to the variations in thermoelastic stress on the systems in which they are found. The two modes of buckling are related to inhomogeneous distributions of thermal stress in either a radial or circumferential directions.

In this work, modelling of various environmental, situational, and geometrical factors on frictional disc systems illustrates their impacts on thermal distribution and the resulting thermal stresses and moments created. This helps in the prediction of buckling, a particular type of distortion, based on temperature differences between the inner and outer radii of discs responsible for heat dissipation. For example, buckling of an automatic transmission clutch depends on a dimensionless geometric shape factor ψ, material properties, and the magnitude of the largest thermal excursion [37]. In friction

disc systems, it is important to be able to understand and model temperature distributions and resulting thermal stresses to configure the system in such a way as to avoid buckling.

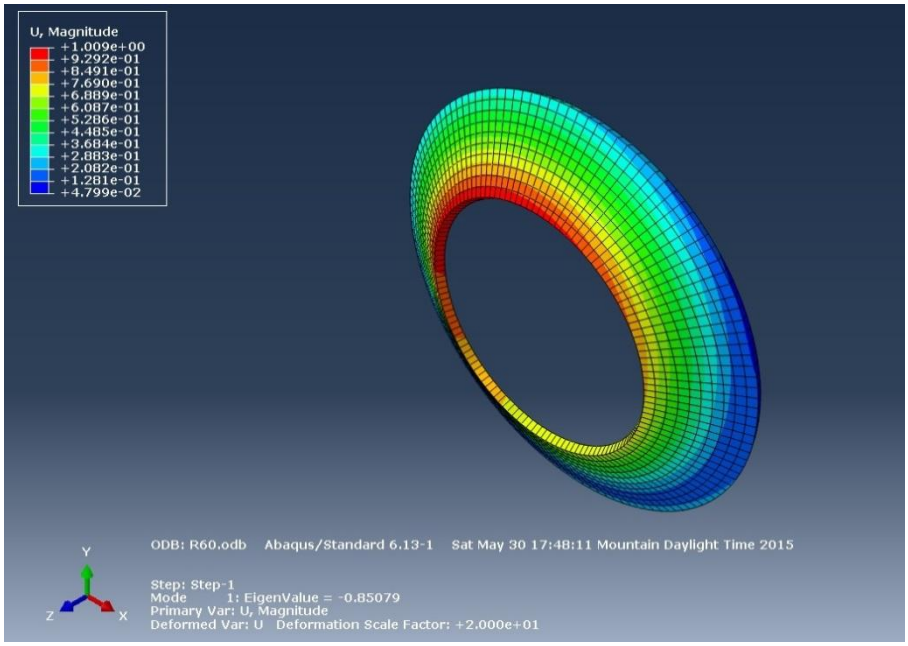

Figure 4.2: Cone buckling mode (N=0)

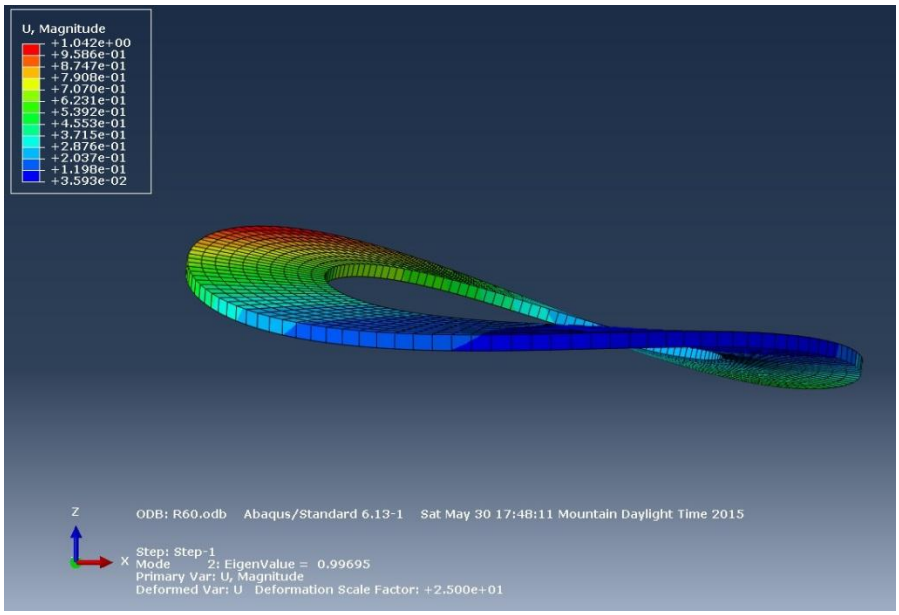

Fig 4.3: Potato chip buckling mode (N=2)

In-plane thermal stresses can be expected whenever there is a temperature difference between the inner and outer radii of a heat-dissipating disc. Various authors [19],[22],[53-55] have shown that non-uniform heating of a frictional sliding surface can result in excited thermoelastic instability, whereby thermoelastic distortions of the sliding bodies affect the contact pressure distribution, exaggerating an initial non-uniformity and leading eventually to incomplete contact between surfaces. Therefore, this work is focused upon modelling various temperature distributions upon a disc and determining the thermal stresses created, and there are corresponding moments. These moments are compared with critical values to indicate buckling. We believe that this will provide insight into system design choices and configurations so as to keep the prevention of buckling in mind.

4.2 Modelling Approach

On the basis that non-uniform temperature is responsible for the creation of thermal stresses within frictional discs, the focus of modelling in this work is based around the effects of various non-uniform temperature distributions to analyze their effects on buckling when paired with changes in other situational and geometrical properties of the system. Of primary concern is the exploration of linear, parabolic, and power temperature distributions within a disc in regards to buckling. Consider a thin, solid circular disc of radius $\boldsymbol{b}$ with a central hole of radius $\boldsymbol{a}$ and uniform thickness $\boldsymbol{h}$. It possesses a central radius $\boldsymbol{R}$ that resides half-way between $\boldsymbol{a}$, the inner radius, and $\boldsymbol{b}$, the outer radius. Three types of coordinate systems are indicated by this hollow, cylindrical disc: $\boldsymbol{r}$ in the radial direction, $\boldsymbol{\theta}$ in the circumferential/tangential direction, and $\boldsymbol{h}$ in the

vertical direction normal to the ***r-θ*** plane. For our model, temperature differences are indicated in the radial direction, thus varying with ***r***. The surface of the disc is assumed to be free of traction.

In approaching our modelling, it was necessary to make certain fundamental assumptions.in order for our equations and conjectures to hold. Firstly, physical assumptions include that the distribution of heat penetrates the disc evenly and that outside connecting structures are rigid and do not affect the distribution of heat. Secondly, materials are assumed to be uniform and consistent in qualities and property without preexisting flaws or damage. Perhaps what is most important is the assumption that heat distribution affects the potential of thermoelastic distortion, the premise upon which this work was founded.

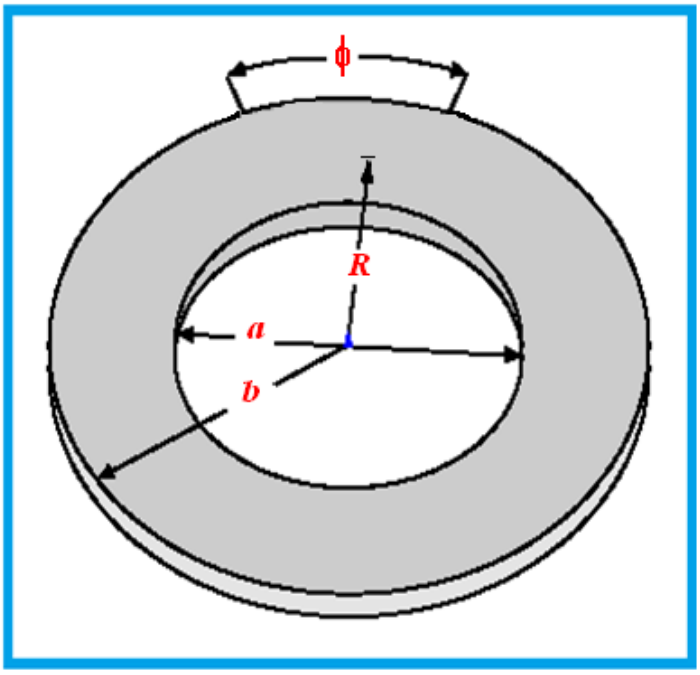

Figure 4.4: Disc Geometry

Additionally, we assumed that such distortion would be the predominant cause of failure of the system and that other forms of failure are prevented to a large enough extent by the resiliency and configuration of system and materials such that there are not compound effects of failure created by the conglomeration of multiple potential failure conditions. These assumptions are to simplify and purify the means of modelling and analysis such that the results presented herein are untainted and uncomplicated and focused upon the premises of concern. We believe that such assumptions and their disclosure are necessary for proper analyses and that the assumptions made herein will not affect the validity of the gathered results and that the modification or omission of one or more such assumptions can be seen as opportunity for further expansion under more specialized situations and conditions.

Based on assumptions that adhere to Hook's law, the radial and circumferential thermal stresses of the circular disc are indicated by the following with terms defined in Table 1:

$$\sigma_r = -\frac{\alpha E}{r^2}\int_a^r Tr\, dr + \frac{EC_1}{1-v} - \frac{EC_2}{(1+v)r^2} \tag{4.1}$$

$$\sigma_\theta = \frac{\alpha E}{r^2}\int_a^r Tr\, dr - \alpha ET + \frac{EC_1}{1-v} + \frac{EC_2}{(1+v)r^2} \tag{4.2}$$

Applying boundary conditions to (1) and (2) such that $\sigma_r = \sigma_\theta = 0$ at $r = a$ and $r = b$, constants C_1 and C_2 can be found:

$$C_1 = \frac{(1-v)\alpha}{b^2 - a^2}\int_a^b Tr\, dr$$

$$C_2 = \frac{(1+v)\alpha a^2}{b^2 - a^2}\int_a^b Tr\, dr$$

This allows (1) and (2) to be simplified to:

$$\sigma_r(r) = \alpha E\left(-\frac{1}{r^2}\int_a^r Tr\,dr + \frac{1}{b^2-a^2}\left(\int_a^b Tr\,dr\right)\left(1-\frac{a^2}{r^2}\right)\right)$$

$$\sigma_\theta(r) = \alpha E\left(\frac{1}{r^2}\int_a^r Tr\,dr + \frac{1}{b^2-a^2}\left(\int_a^b Tr\,dr\right)\left(1+\frac{a^2}{r^2}\right) - T\right)$$

In order for the surface of the disc to be traction free, there must not exist a net stress across the radial axis of the disc as indicated by:

$$F = \int_{a-R}^{b-R} \sigma\,(y+R)h\,dy = 0 \tag{4.3}$$

This can be rewritten as:

$$F = \int_a^b \sigma\,(r)h\,dr = 0 \tag{4.3}$$

However, a section can transmit an axisymmetric moment as indicated by:

$$M = \int_{a-R}^{b-R} \sigma(y+R)hy\,dy \tag{4.4}$$

This can be rewritten as:

$$M = \int_a^b \sigma(r)h(r-R)\,dr \tag{4.4}$$

Equations (1), (2), and (4) exhibit the relationship between moment and temperature distribution through stress distribution in the disc. What remains is to determine under what conditions buckling may occur to properly bound the situational (temperature distribution and material choice) and geometrical (radii and thickness) properties of the system.

Buckling in the disc results from an in-plane, axisymmetric, residual bending moment ***M***. The sign of the moment ***M*** indicates the direction of the bending relative to the appropriate coordinate (radial or circumferential). However, the simple presence of a moment ***M*** is not alone enough to result in buckling. Such a moment must exceed a

certain critical value, which can differ in the positive and negative directions, in order for buckling to occur. This critical value, referred to as the critical moment $\boldsymbol{M_0}$, can be determined by treating the disc as a cylindrical disc and applying the results found by Timoshenko and Gre [38].

For certain friction disc applications, situational factors have been gathered from data from reference. For steel as a material choice, the nominal details of the physical properties, dimensions, and operating conditions of our disc system are given in Table 1. In our experiments, these factors were adjusted to explore their relationships to buckling.

Inner disc radius (a)	110 mm
Outer disc radius (b)	140 mm
Mean disc radius (R)	125 mm
Disc thickness (h)	2 mm
Sliding length	20 mm
Young's modulus (E)	210 x 10^3 N/mm^2
Thermal expansion coefficient (α)	12.5 x 10^{-6} C^{-1}
Poisson's ratio (ν)	0.3

Table 4.1: Example parameters for a friction disc system

In approaching our experimentations, we assumed various temperature distributions were possible and modelled each with other varying parameters. The temperature distributions considered were linear, parabolic, and power in the radial direction, thus making them a function of $\boldsymbol{r}$. These $\boldsymbol{T(r)}$ resulted in thermal stress field's $\boldsymbol{\sigma(r)}$ that satisfied (3). The practical choice of materials brought a degree of nonlinearity as the thermal expansion coefficient $\boldsymbol{(T)}$ and Young's modulus $\boldsymbol{E\ (T)}$ depend significantly upon temperature. When determining conditions of buckling, the stress fields were

utilized to determine the magnitude and direction of moments, which could then be compared to corresponding critical moments.

These critical moments are indicated by:

$$M_o = \overline{M_0}\,\frac{C}{R} \tag{4.5}$$

The dimensionless critical moments for integral wave-number $\boldsymbol{N}$:

$$\overline{M_0} = \frac{1+K}{2} \mp \sqrt{\left(\frac{1-K}{2}\right)^2 + KN^2} \tag{4.6}$$

For the case of a rectangular cross-section of thickness $\boldsymbol{h}$ and radial thickness ($\boldsymbol{b}$-$\boldsymbol{a}$):

$$K = \frac{1+v}{2}, \quad C = \frac{G(b-a)h^3}{3}, \quad G = \frac{E}{2(1+v)}$$

From these definitions and the quadratic nature of the dimensionless critical moment $\overline{\boldsymbol{M_0}}$, it can be observed that there exist positive and negative (directional) critical moments. If any determined moment for a particular situation and configuration exceeds its corresponding directional critical moment, our model indicates that buckling will occur. It is from this formulation that we proceeded with our experimentations and gathered our results for analysis.

4.3 Results and Discussion

Under the models and premises set forth previously, the primary means of variance for our experiments was through variation of temperature distribution along the radial axis. The three temperature distributions of focus were linear, parabolic, and power. Other geometric aspects of the system were varied to show the corresponding relationships between temperature distribution and these aspects. The results presented herein should be generalizable as the signs, configuration parameters, and structural

configurations of the temperature distribution models are all modifiable and readily substituted. Of particular note are the general parameters ***Tmin*** and ***Tmax***, which represent the minimal and maximal temperatures present in the distribution, respectively. Choices of maximal temperature were based on material properties and operating conditions found from modelling in existing works. For instance, the authors of [6] noted that "to provide adequate braking force the disc and pad as a friction pair operates at temperatures up to 800 ˚C."

4.3.1 Linear Temperature Distribution

The linear temperature distribution proved the most simple to model. It involved a linear increase in temperature from ***a*** to ***b***, as illustrated in Figure (4.5). This results in a model similar to the ABAQUS model shown in Figure (4.6). Several existing works assume a linear temperature distribution as a starting point for analysis [40, 41]. It can be noted that a linear temperature distribution is simply the first-order case of power temperature distribution with the zeroth-order case being a constant temperature distribution. This logically follows from the fact that the sliding speed involved with friction of a disc is linear and proportional to the radius. Thus, as revolutions are made during frictional contact, the smaller inner radius will build up heat more quickly than the larger outer radius. If this heat buildup is assumed to be evenly distributed with radius, a linear distribution results. It is from this that a linear distribution can also be considered as a well-distributed, unevenly centered parabolic distribution, as is the case of some materials, such as AMC, utilized for rotors in disc systems, such as those discussed by the authors of [47, 48, and 49].

$$T(r) = m\,(r - a) + Tmin \tag{4.7}$$

where

$$m = \frac{Tmax - Tmin}{b - a}$$

making

$$\int_a^r Tr\,dr = \frac{1}{6}\left(a^3 m - 3a^2 Tmin - 3am\,r^2 + r^2(2\,m\,r + 3Tmin)\right) \tag{4.8}$$

Substituting (4.8) into (4.1) and (4.2) yields:

$$\sigma_r = -\frac{\alpha E}{r^2}\left[\frac{1}{6}\left(a^3 m - 3a^2 Tmin - 3am\,r^2 + r^2(2\,m\,r + 3Tmin)\right)\right] + \frac{EC1}{1-v} - \frac{E\,C2}{(1+v)r^2} \tag{4.9}$$

$$\sigma_\theta = \frac{\alpha E}{r^2}\left[\frac{1}{6}\left(a^3 m - 3a^2 Tmin - 3am\,r^2 + r^2(2\,m\,r + 3Tmin)\right)\right] - \alpha ET + \frac{EC1}{1-v} + \frac{E\,C2}{(1+v)r^2} \tag{4.10}$$

These radial and tangential stresses for a linear temperature distribution yield the curves shown in Figure (4.7) .While the tangential stress is an order of magnitude greater than the radial stress, it depends upon the resulting moment and its relationship to the critical moment for each direction as to whether or not buckling occurs.

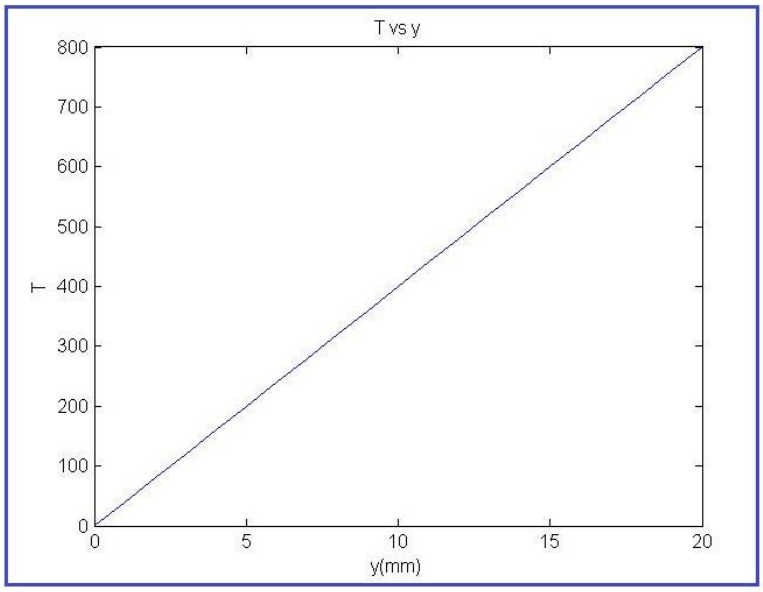

Figure 4.5: Linear Temperature Distribution

Substituting (4.10) into (4.4) yields the moments produced by radial and tangential stress:

$$M_\theta = h\left[\int_a^b \sigma_\theta r\, dr - \int_a^b \sigma_\theta R\, dr\right] \tag{4.11}$$

where

$$\int_a^b \sigma_\theta\, r\, dr = \int_a^b \frac{\alpha E}{6r}[m(a^3 - 3ar^2 + 2r^3) + 3T_{min}(r^2 - a^2)]\, dr - \int_a^b \alpha E r[\text{m (r} - \text{a)} +$$

Tmin *dr+abEC1r1−v+EC21+vr dr*

$$\int_a^b \sigma_\theta R\, dr = \int_a^b \frac{\alpha ER}{r^2}[m(a^3 - 3ar^2 + 2r^3) + 3T_{min}(r^2 - a^2)]\, dr\ - \int_a^b \alpha ER[\text{m (r} - \text{a)} +$$

Tmin *dr+abEC1R1−v+EC2R1+vr2 dr*

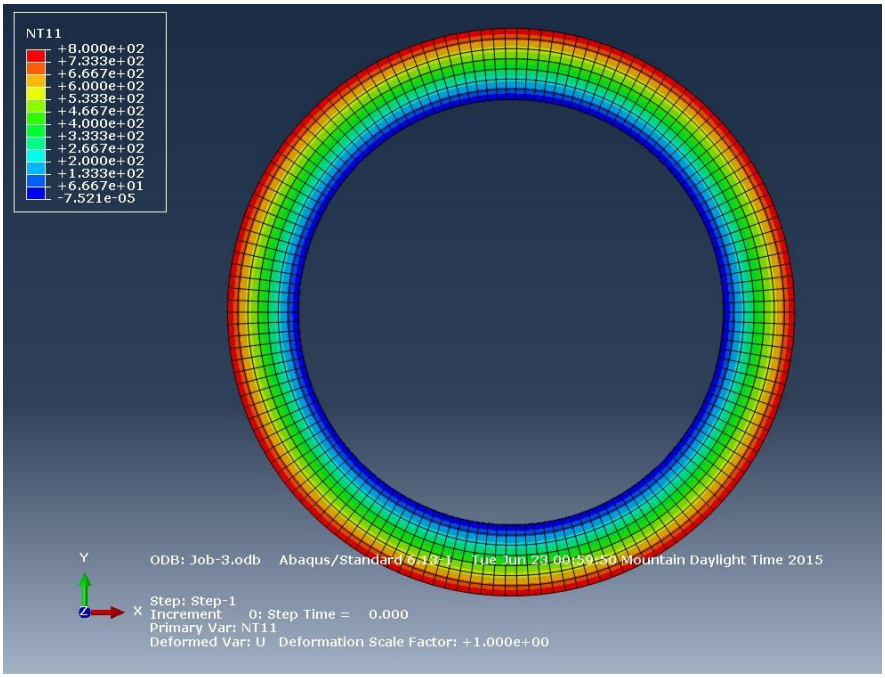

Figure 4.6: Linear Temperature Distribution in Disc

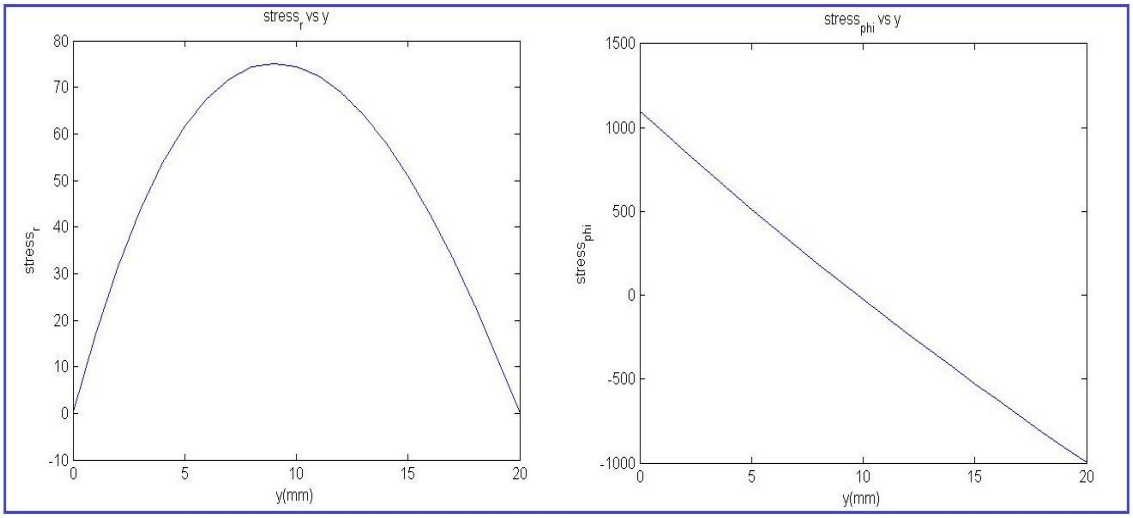

Figure 4.7: Stress Distributions for Linear Temperature Distribution

Graphing both critical moments from (4.5) with (4.11) show the relationships between critical moment and the produced moments. Figure (4.8) shows the relationship with varying central radius R with various maximum temperatures. Figure 4.9 shows the relationship with varying sliding length (b-a) with various maximum temperatures. Figure (4.10) shows the relationship with varying thickness h with various maximum temperatures. Figure (4.9) clearly shows that a much smaller sliding length is necessary to prevent buckling with a maximum temperature of 1000 ˚C than with a maximum temperature of 200 ˚C. Figure (4.8) shows that a much smaller central radius and hence a much smaller disc is necessary to withstand buckling at higher maximum temperatures. Figure (4.10) shows that increasing the thickness (h) by even a millimeter adds resiliency against buckling. The obtained results show that the critical moment results in buckling is within the range (-115 Nm ~ -140 Nm) as shown in all three figures with the parameters utilized in table (4.1). This shows strong similarity to the results presented in ref [37] by [Nadine Audebert & J.R.Barber] in Table 1 on page 314 that indicate that the critical

moment that results in buckling is -137 Nm at a thickness 3 mm for N=2. It should be noted that the results in ref [37] are based on a changing temperature with time that is linear in nature. However, the converse is true as well, which indicates that machining of the disc to smooth it to prevent hotspots due to previous deformation results in a much increased chance of buckling due to thinness.

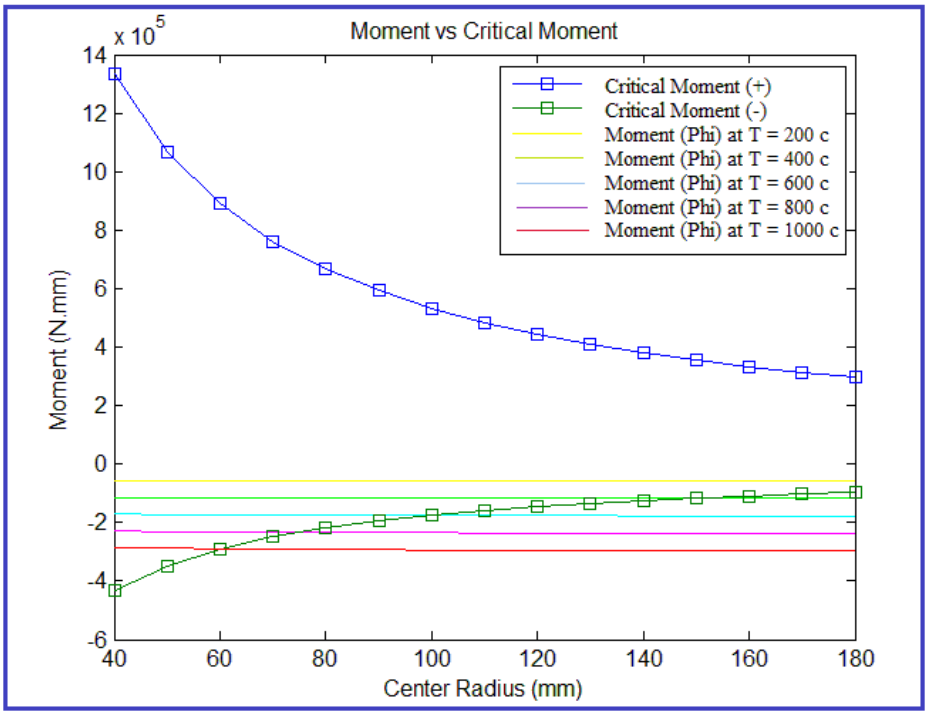

Figure 4.8: Relationship between actual moment and critical moments for linear temperature distributions with varying central radius

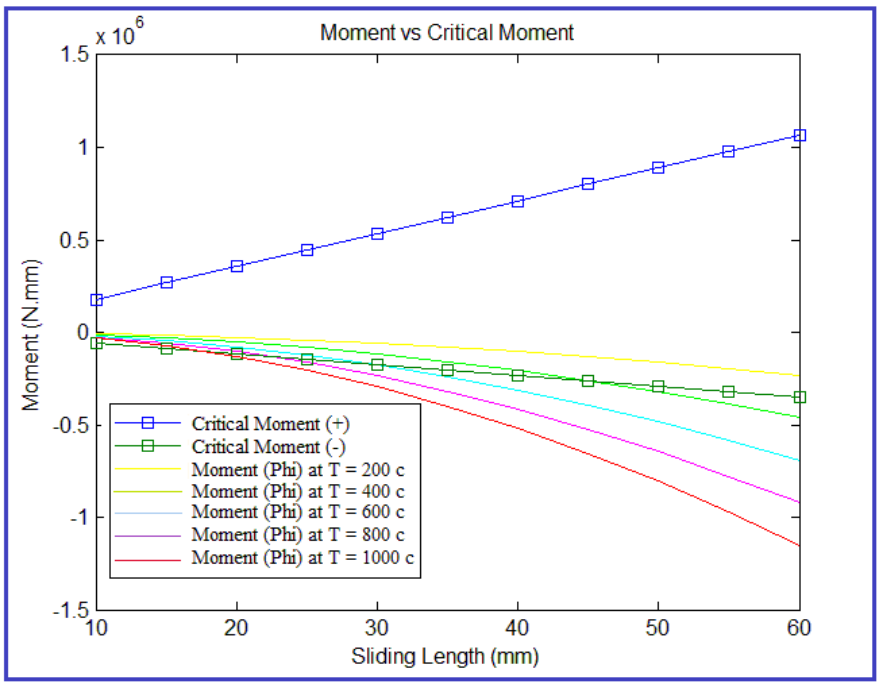

Figure 4.9: Relationship between actual moment and critical moments for linear temperature distributions with varying Sliding length

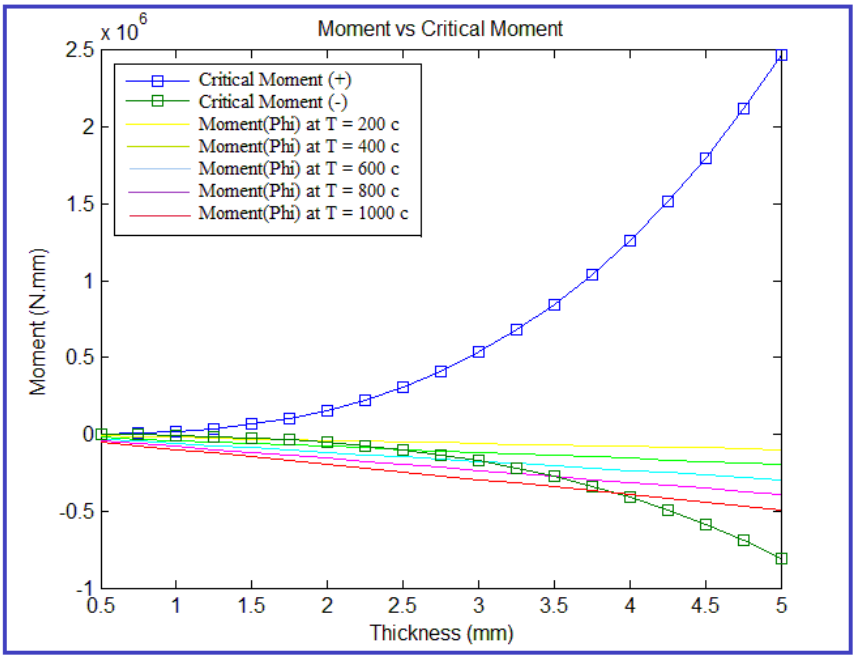

Figure 4.10: Relationship between actual moment and critical moments for linear temperature distributions with varying thickness

Figure (4.11) has shown the thermal buckling for cylindrical disk when the temperature distribution is linear at different center radius and Figure (4.13) has shown the thermal buckling for cylindrical disk when the temperature distribution is linear at different sliding length and Figure (4.15) has shown the thermal buckling for cylindrical disk when the temperature distribution is linear at different thickness.

Table (4.2), Table (4.3), and Table (4.4) and the corresponding Figure (4.12), Figure (4.14), and Figure (4-16) show comparison of the analytical and numerical results of our experiments for a linear temperature distribution. It is evident that the result for varying central radius and sliding length are practically indistinguishable. However, an anomaly in the numerical analysis was observed for varying thickness. The reason is not clear.

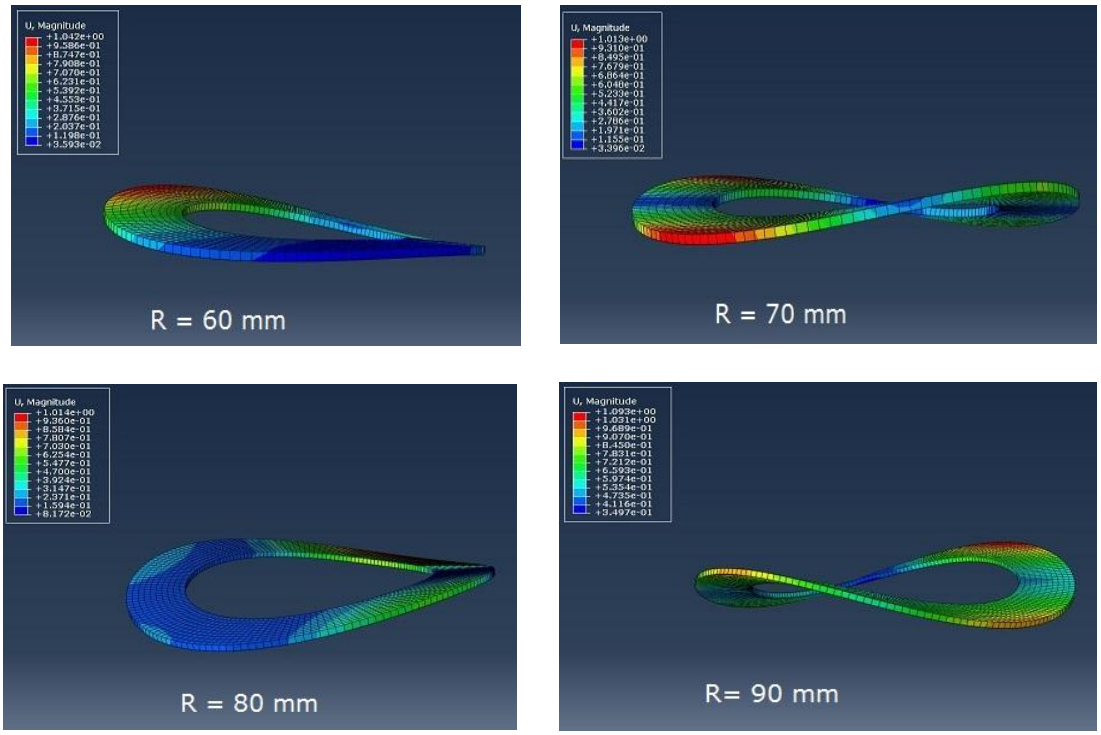

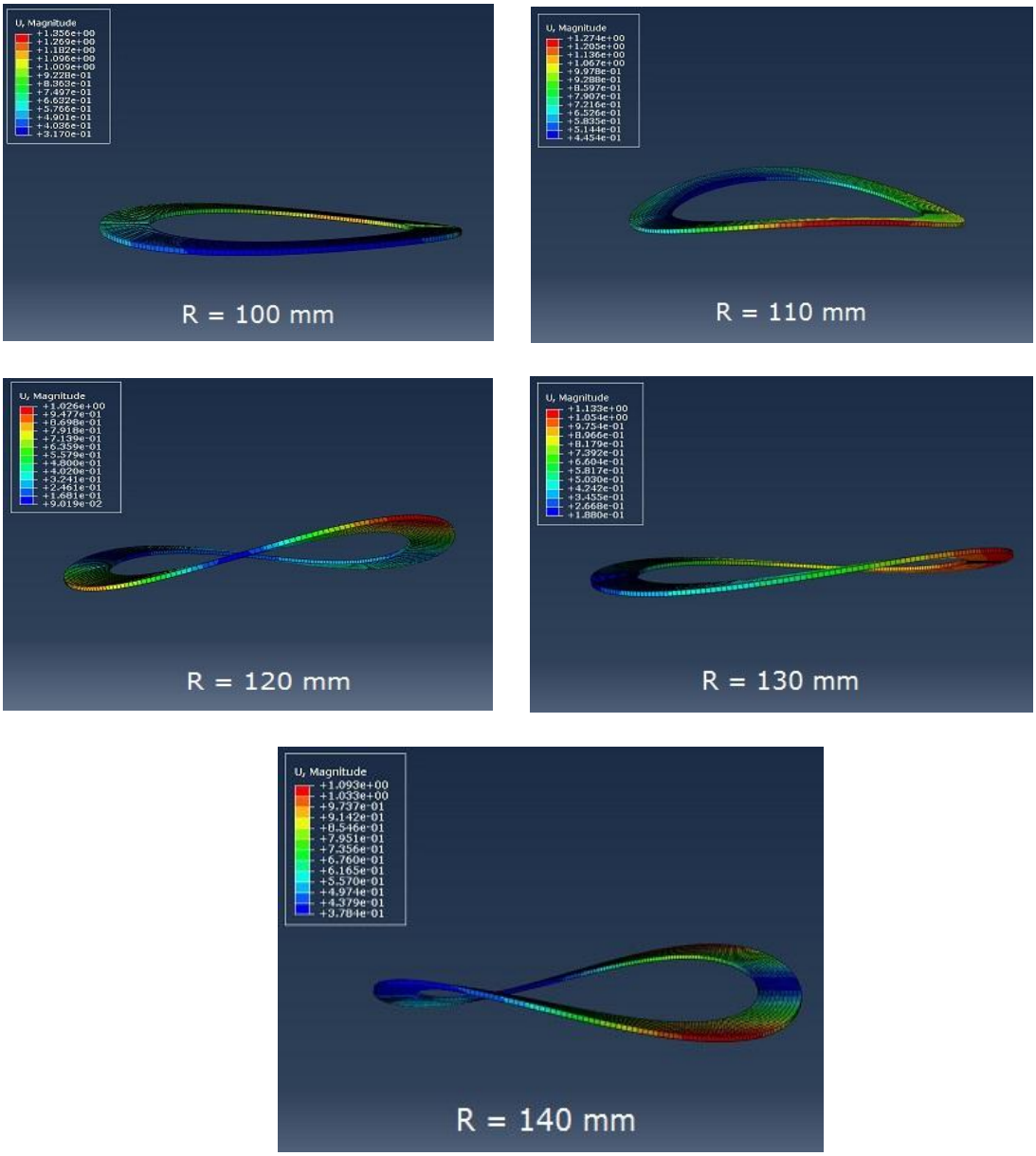

Figure 4.11: Deformation mode of thermal Buckling at different center radius

Fixed parameters:

Center Radius (R)	Sliding length	Thickness (h)	Young modules (E)	Thermal Expansion (α)
(60mm ~ 140mm)	30 mm	3 mm	$210x10^3$ N/mm^2	$12.5x10^{-6}$

R (mm)	Ra	Rb	T(Analytical)	M (Analytical)	T(Numerical)	ʎ1	M (Numerical)
60	45	75	1000	-289.6	997	0.997	-288.7312
70	55	85	852	-248.3	849	0.996	-247.3068
80	65	95	743	-217.2	740	0.996	-216.3312
90	75	105	660	-193.1	655	0.992	-191.5552
100	85	115	593	-173.8	589	0.993	-172.5834
110	95	125	540	-158	534	0.989	-156.262
120	105	135	494	-144.8	489	0.989	-143.2072
130	115	145	456	-133.7	451	0.989	-132.2293
140	125	155	424	-124.1	418	0.985	-122.2385

Table 4.2: Modeling parameters for changing central radius for linear temperature distribution

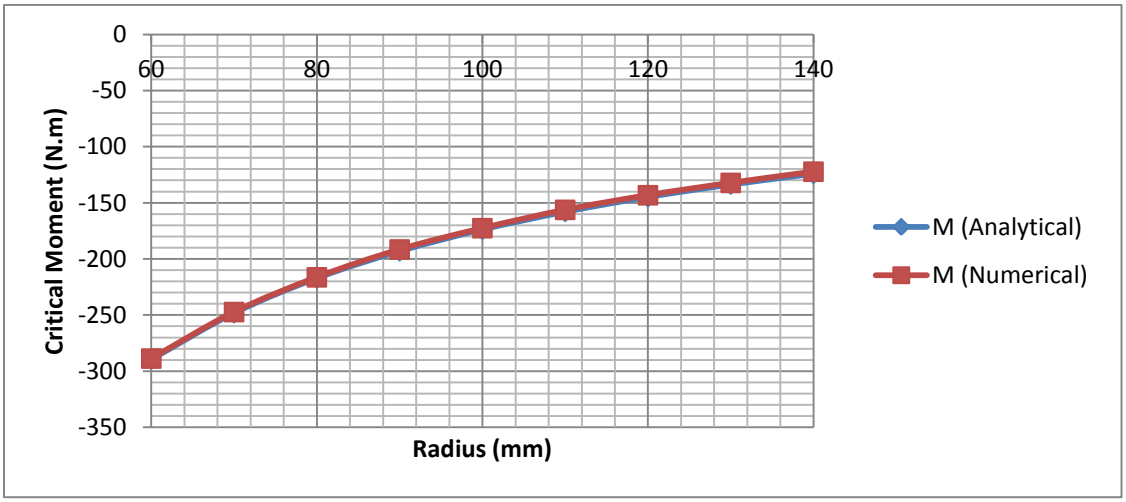

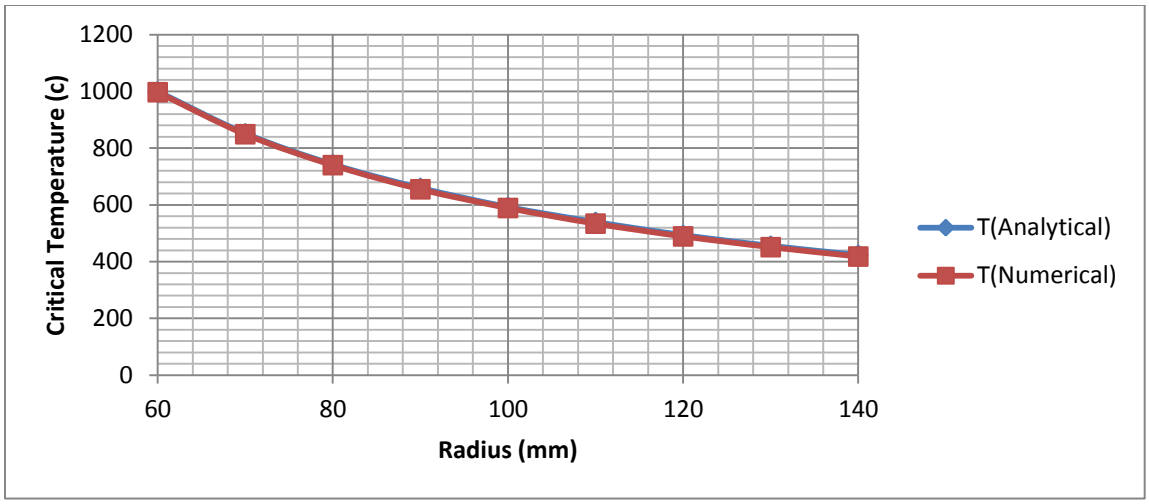

Figure 4.12: Analytical versus numerical results

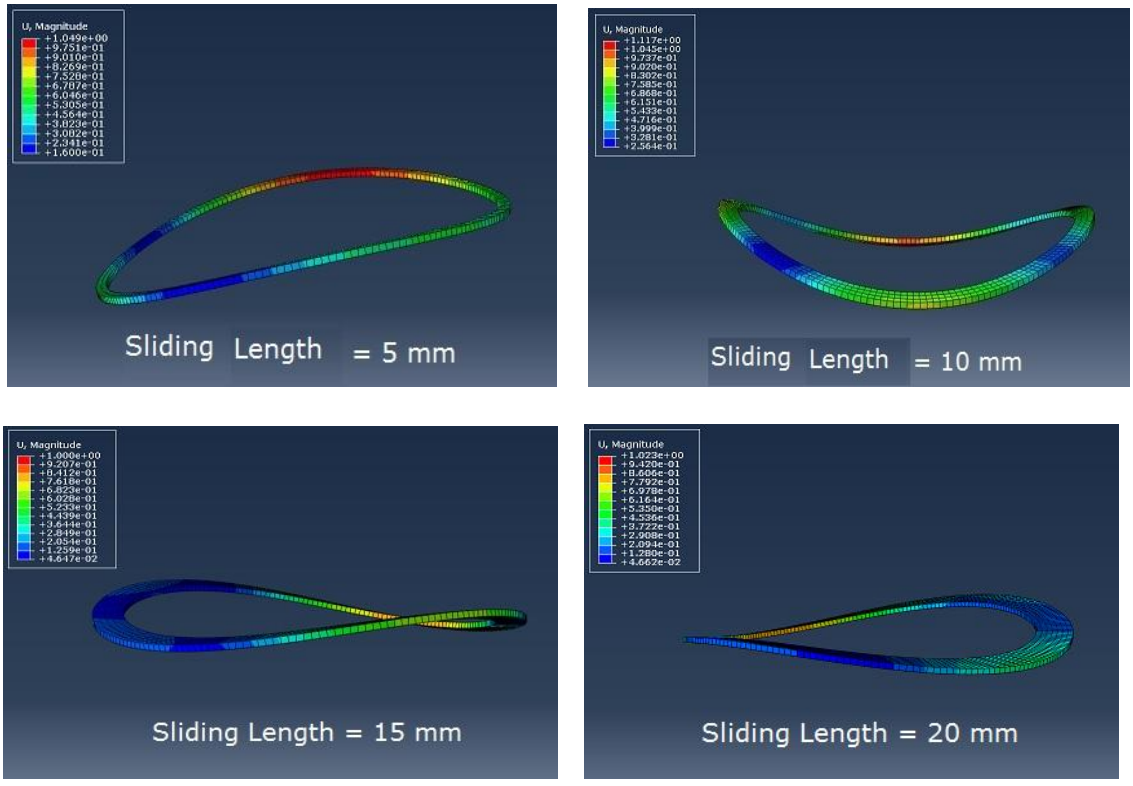

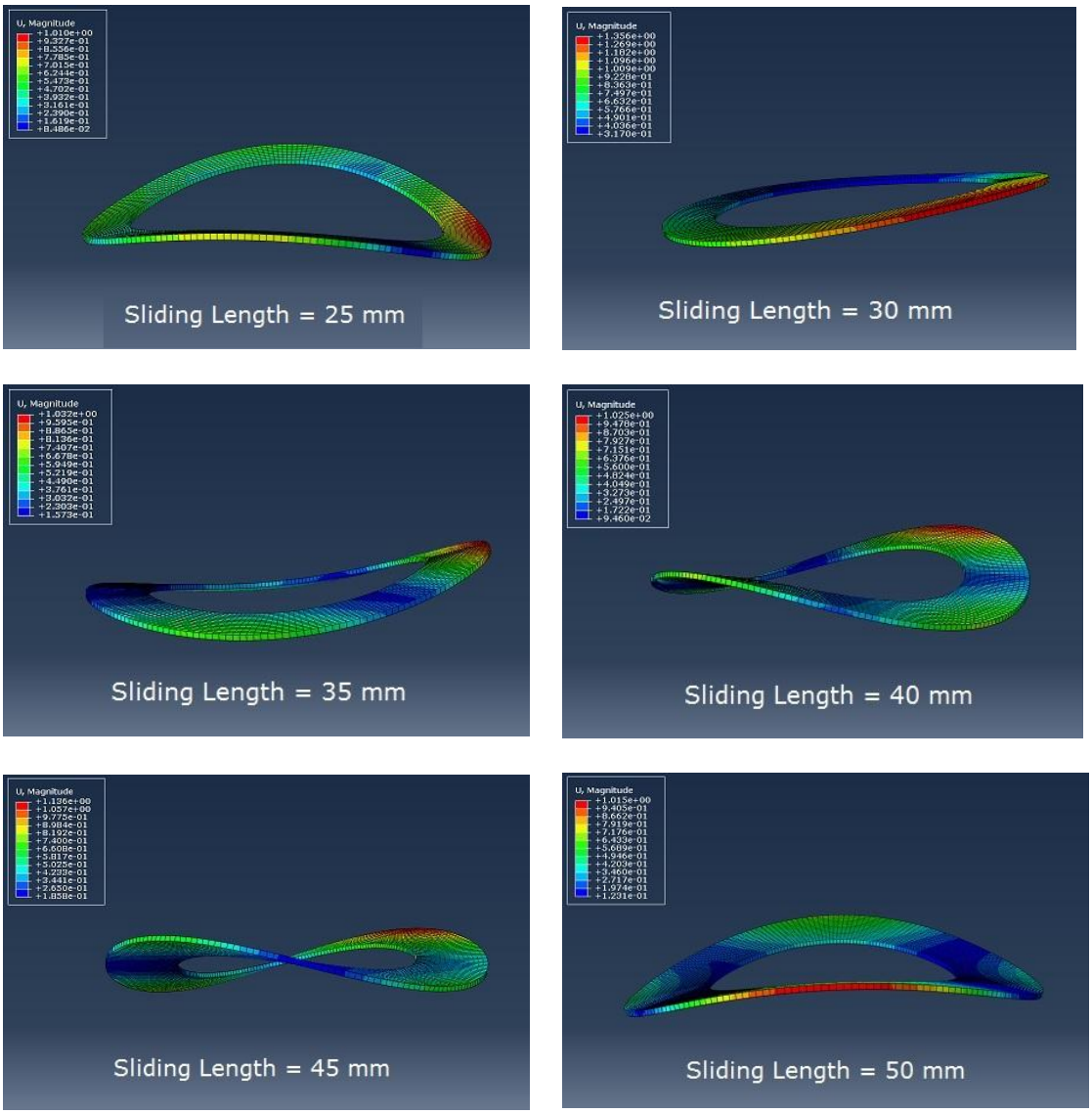

Figure 4.13: Deformation mode of thermal Buckling at different Sliding length

Fixed parameters

Sliding length	Mean Radius (R)	Thickness (h)	Young's modulus (E)	Thermal Expansion (α)
10 ~ 50 mm	**100 mm**	**3 mm**	**$210x10^3$ N/mm^2**	**$12.5x10^{-6}$**

Sliding Length	Ra	Rb	T(Analytical)	M (Analytical)	T(Numerical)	ʎ1	M (Numerical)
10	95	105	1710	-57.93	1670	0.976	-56.53968
15	92.5	107.5	1180	-86.89	1150	0.974	-84.63086
20	90	110	886	-115.86	860	0.97	-112.3842
25	87.5	112.5	710	-144.8	695	0.978	-141.6144
30	85	115	593	-173.79	588	0.991	-172.22589
35	82.5	117.5	510	-202.7	512	1.003	-203.3081
40	80	120	447	-231.7	443	0.991	-229.6147
45	77.5	122.5	398	-260.7	399	1.002	-261.2214
50	75	125	359	-289.6	358	0.997	-288.7312

Table 4.3: Modeling parameters for changing sliding length for linear temperature distribution

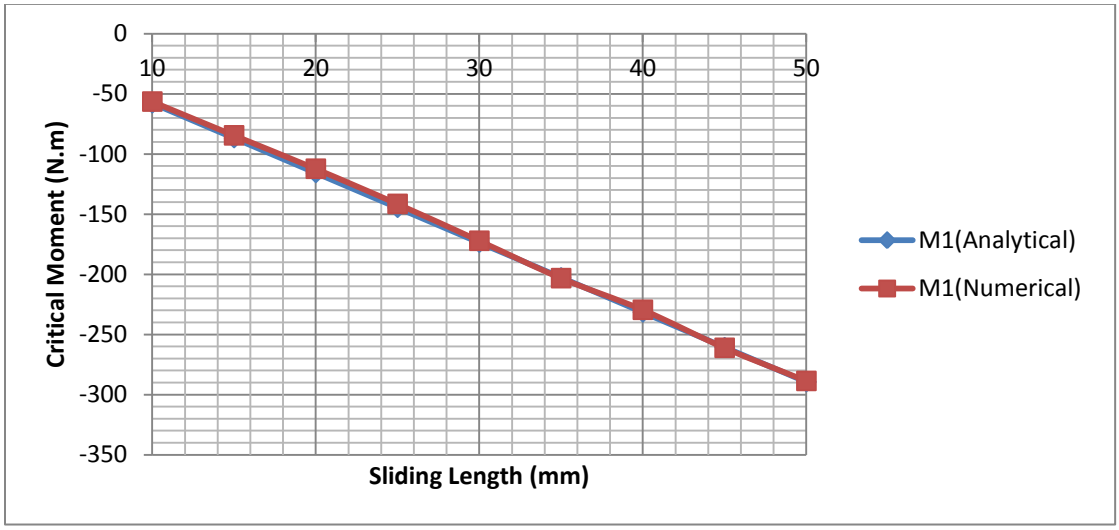

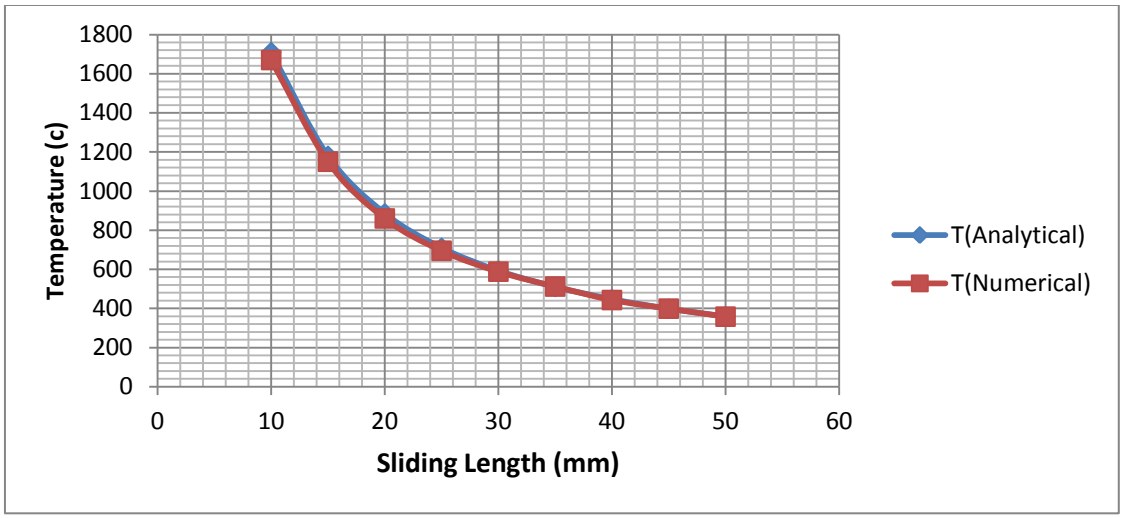

Figure 4.14: Analytical versus numerical results

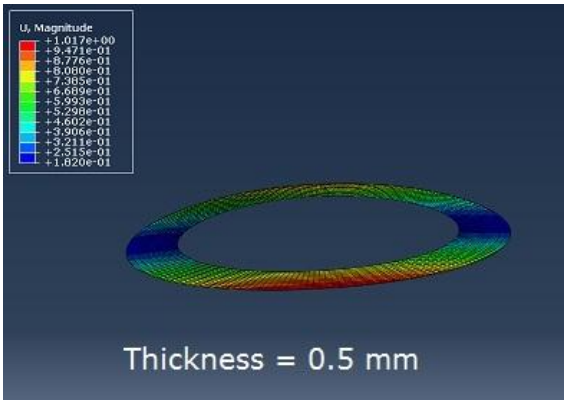

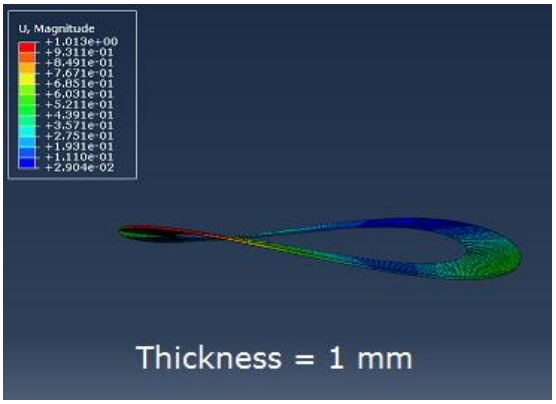

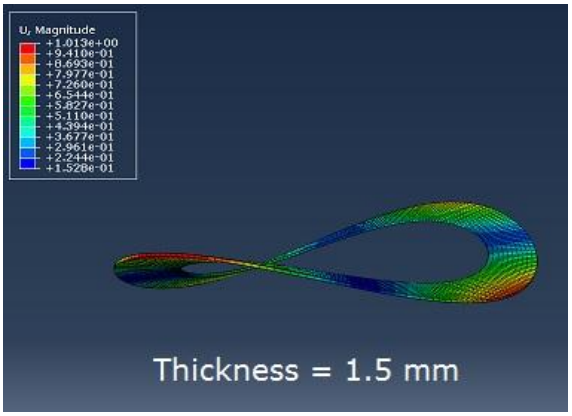

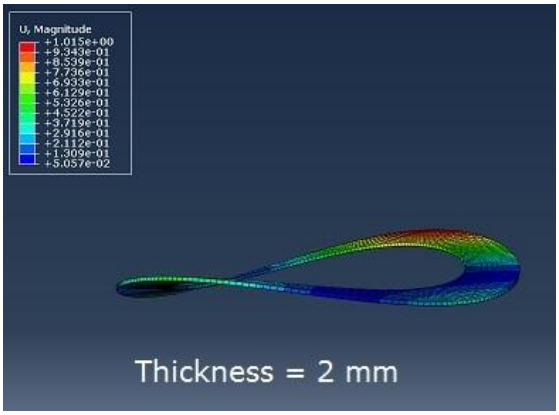

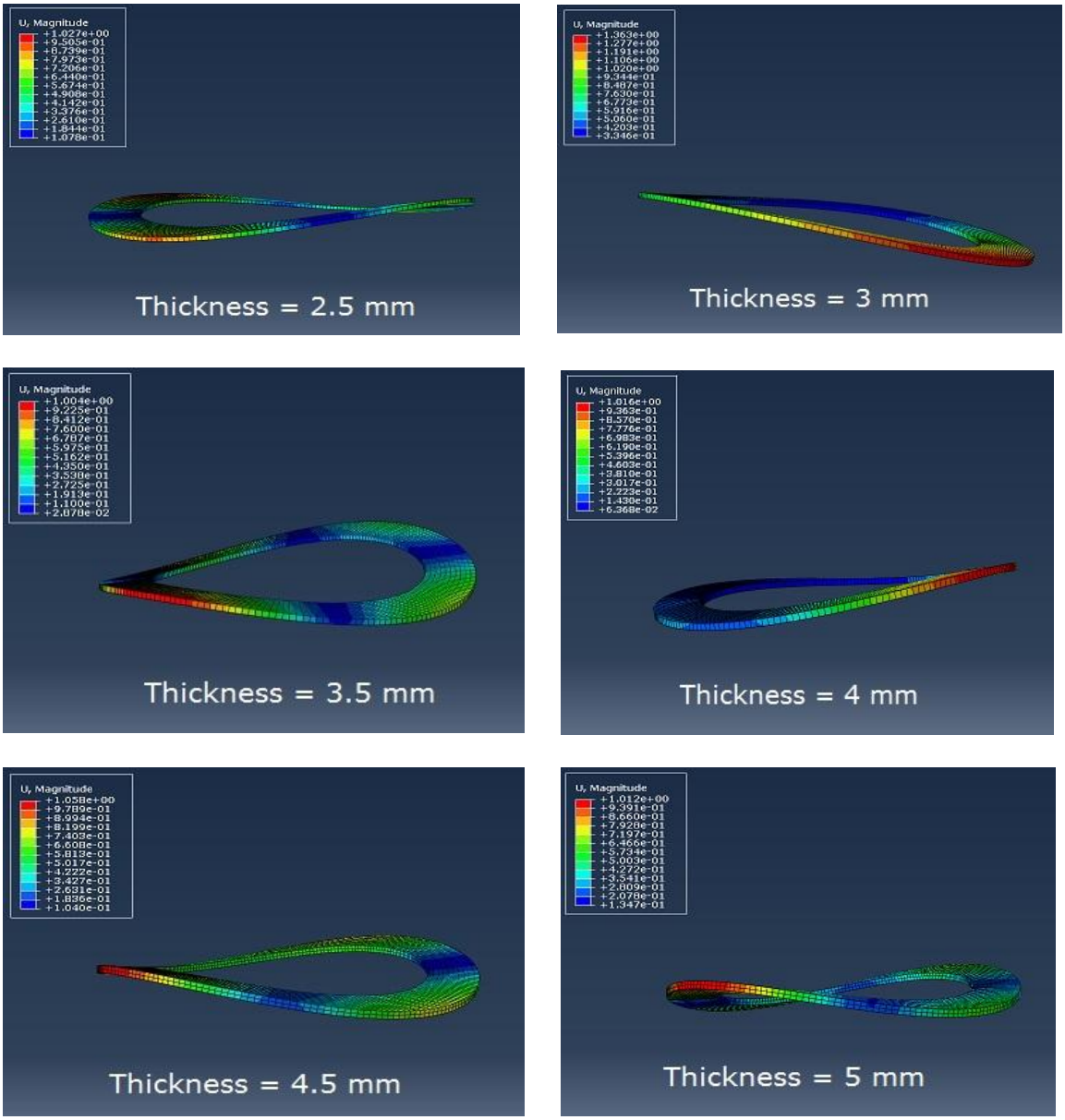

Figure 4.15: Deformation mode of thermal Buckling at different Thickness

Fixed parameters:

Thickness (h)	Sliding length	Center Radius (R)	Young's modulus (E)	Thermal Expansion (α)
0.5 ~ 5 mm	30 mm	105 mm	$210x10^3$ N/mm^2	$12.5x10^{-6}$

H (mm)	Ra	Rb	T(Analytical)	M1(Analytical)	T(Numerical)	ʎ1	M1(Numerical)
0.5	85	115	17	-0.8	17	1	-0.8
1	85	115	66	-6.43	66	1	-6.43
1.5	85	115	149	-21.7	149	1	-21.7
2	85	115	264	-51.5	264	1	-51.5
2.5	85	115	412	-100.5	410	0.995	-99.9975
3	85	115	593	-173.79	588	0.991	-172.22589
3.5	85	115	808	-275.97	797	0.986	-272.10642
4	85	115	1055	-411.9	1036	0.982	-404.4858
4.5	85	115	1400	-586.5	2600	1.85	-1085.025
5	85	115	1700	-804.6	3218	1.89	-1520.694

Table 4.4: Modeling parameters for changing thickness (h) for linear temperature distribution

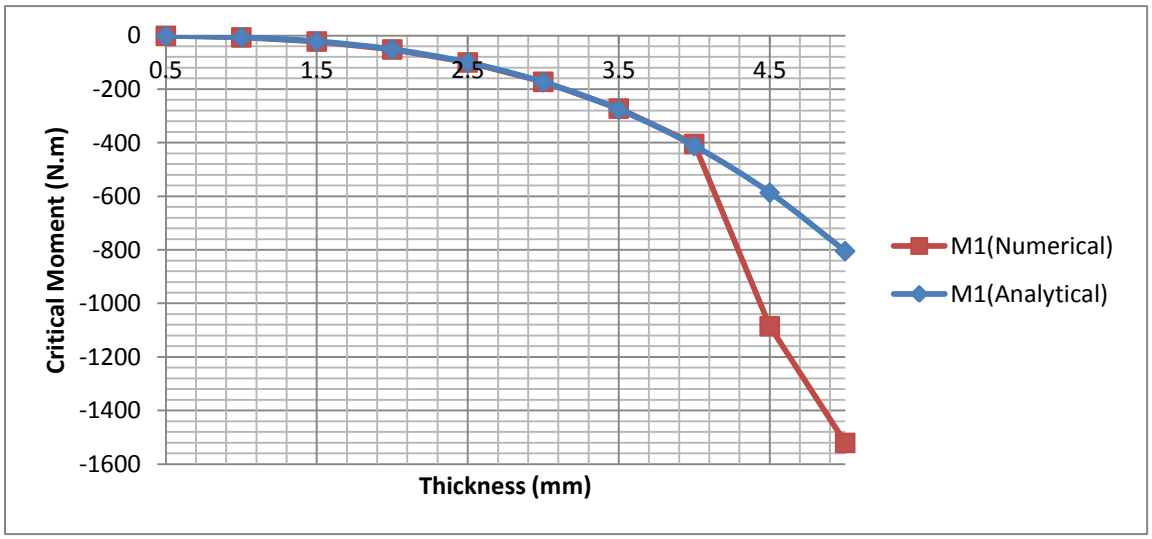

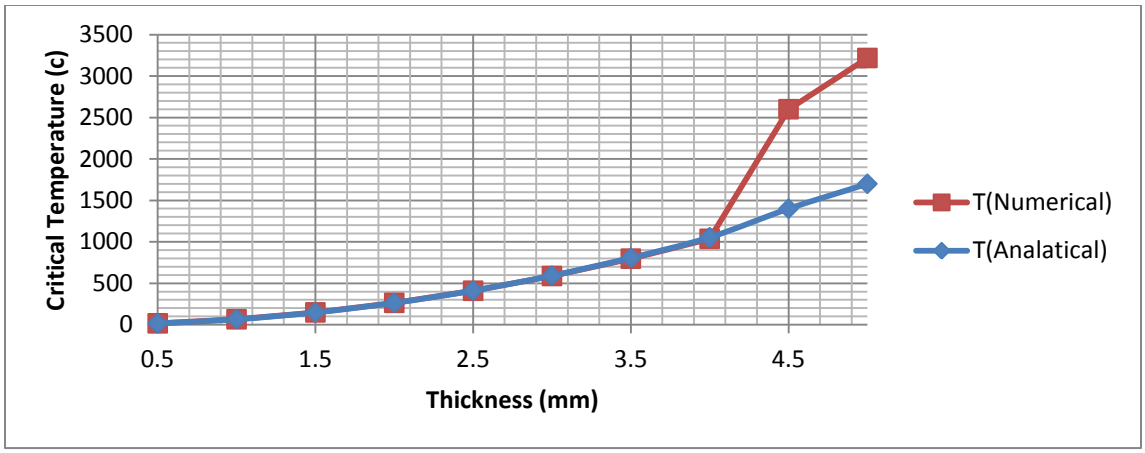

Figure 4.16: Analytical versus numerical results

4.3.2 Parabolic Temperature Distribution

The parabolic temperature distribution proved more complex than the linear temperature distribution model. It involved a parabolic rise and fall in temperature from ***a*** to ***b***, as illustrated in Figure (4.17). This results in a model similar to the ABAQUS model shown in Figure (4.18). The reasoning behind the consideration of a parabolic temperature distribution is its correlation to the notion of "hot spots" and its similarity in overall temperature change across the surface to the power temperature distribution, which is mentioned in numerous existing works [33 and 44]. Though with the notable difference of a decreasing increase in temperature resulting in a peak or plateau of overall temperature. Some existing works directly note and utilize a parabolic distribution [45 and 46]. The authors of [47] utilized and referenced the measurement and actual case study of the authors of [48 and 49], which they demonstrated in a figure in which the measured temperature distribution over the radius was approximately parabolic. Typically, the parabolic distribution is skewed with the mode of the distribution being

centered towards the smaller, inner radius. In the most extreme cases of this, a power distribution has been used rather than a parabolic distribution as discussed in the next section. Authors of current works indicated that the AMC brake rotor demonstrates a more evenly distributed temperature than a cast iron brake rotor, thereby preventing the formation of hot spot zones. The parabolic temperature distribution creates a focal point for heat buildup. It involved a parabolic increase with the maximum temperature found at ***R*** and minimum temperature found at ***a*** and ***b***.

$$T(r) = Tmax - (r - R)^2\ Q \tag{4.12}$$

where

$$Q = \frac{Tmax - Tmin}{\left(\frac{b-a}{2}\right)^2}$$

making

$$\int_a^r Tr\ dr = \frac{Q}{12}\left(3(a^4 - r^4) + 8\ R(r^3 - a^3) + 6R^2(a^2 - r^2)\right) + \frac{Tmax}{2}(r^2 - a^2) \tag{4.13}$$

Substituting (13) into (1) and (2) yields:

$$\sigma_r = -\frac{\alpha E}{r^2}\left[\frac{Q}{12}\left(3(a^4 - r^4) + 8\ R(r^3 - a^3) + 6R^2(a^2 - r^2)\right) + \frac{Tmax}{2}(r^2 - a^2)\right] + \frac{EC_1}{1-v} - \frac{EC_2}{(1+v)r^2} \tag{4.14}$$

$$\sigma_\theta = \frac{\alpha E}{r^2}\left[\frac{Q}{12}\left(3(a^4 - r^4) + 8\ R(r^3 - a^3) + 6R^2(a^2 - r^2)\right) + \frac{Tmax}{2}(r^2 - a^2)\right] - \alpha E[Tmax -$$

$$(r - R)^2\ Q] + \frac{EC_1}{1-v} + \frac{EC_2}{(1+v)r^2} \tag{4.15}$$

These radial and tangential stresses for a parabolic temperature distribution yield the curves shown in Figure (4.19). While the tangential stress is an order of magnitude greater than the radial stress, it depends upon the resulting moment and its relationship to the critical moment for each direction as to whether or not buckling occurs. The sinusoidal pattern of radius stress is highly-indicative of buckling due to the extremes of

its crest and trough. Substituting (4.15) into (4.4) yields the moments produced by tangential stress:

$$M_\theta = h\left[\int_a^b \sigma_\theta r\, dr - \int_a^b \sigma_\theta R\, dr\right] \tag{4.11}$$

where

$$\int_a^b \sigma_\theta\, r\, dr = \int_a^b \frac{\alpha E}{r}\left[\frac{Q}{12}\left(3(a^4 - r^4) + 8\,R(r^3 - a^3) + 6R^2(a^2 - r^2)\right) + \frac{Tmax}{2}(r^2 - a^2)\right] dr -$$

$$\int_a^b \alpha E r\left[Tmax - (r - R)^2\, Q\right] dr + \int_a^b \frac{EC_1 r}{1-v} + \frac{EC_2}{(1+v)r}\, dr$$

$$\int_a^b \sigma_\theta R\, dr = \int_a^b \frac{\alpha E R}{r^2}\left[\frac{Q}{12}\left(3(a^4 - r^4) + 8\,R(r^3 - a^3) + 6R^2(a^2 - r^2)\right) + \frac{Tmax}{2}(r^2 -$$

a2 dr −abαER[Tmax−(r−R)2 Q] dr+abEC1R1−v+EC2R1+vr2 dr

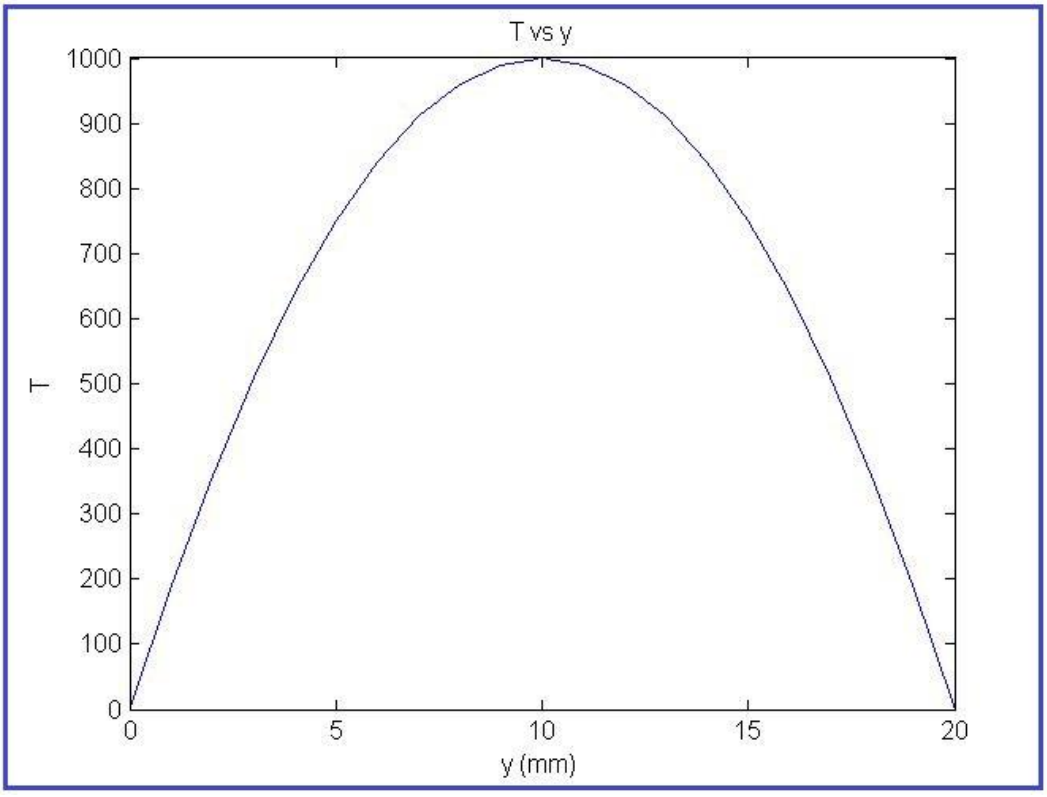

Figure 4.17: Parabolic Temperature Distribution

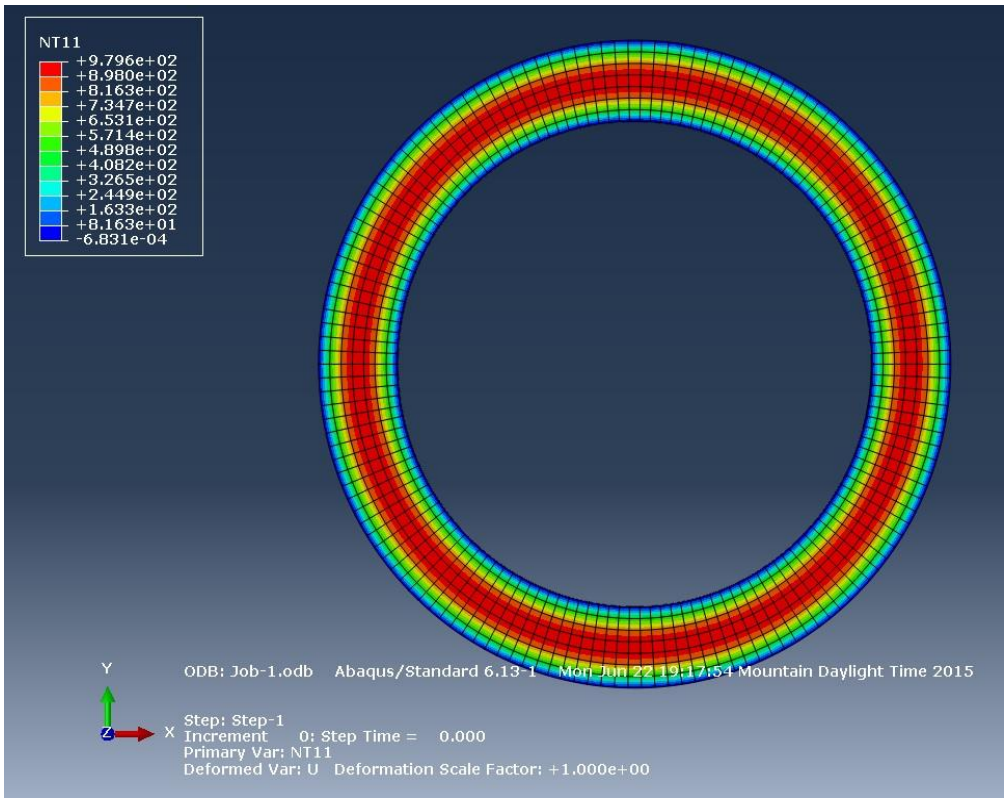

Figure 4-18: Parabolic Temperature Distribution in Disc

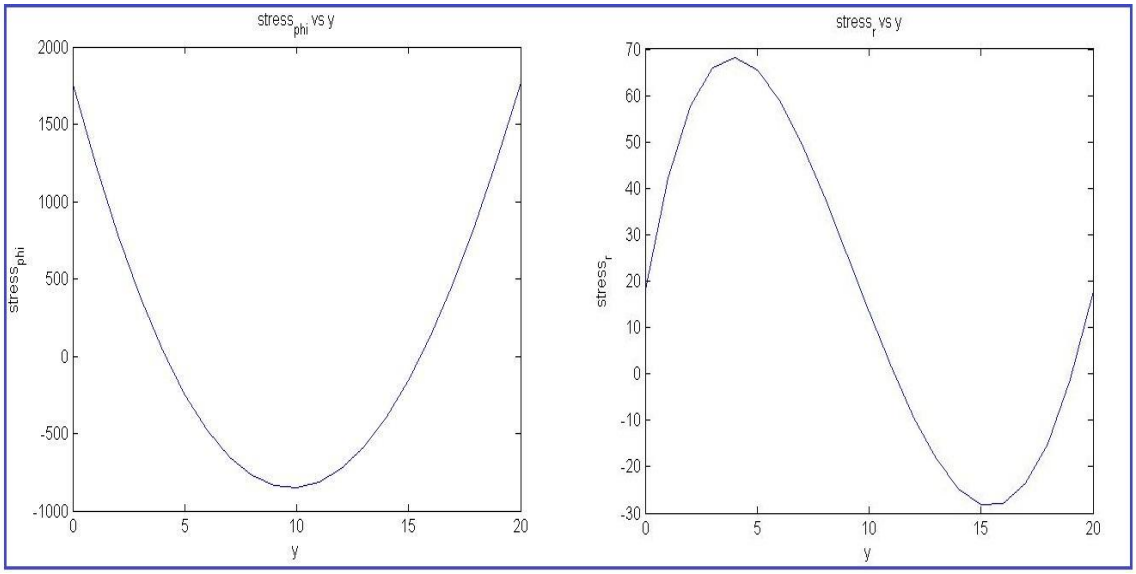

Figure 4.19: Stress Distributions for Parabolic Temperature Distribution

Graphing both critical moments from (4.5) with (4.11) show the relationships between critical moment and the produced moments. Figure (4.20) shows the relationship with varying central radius $\boldsymbol{R}$ with various maximum temperatures. Figure (4.21) shows the relationship with varying sliding length ($\boldsymbol{b}$-$\boldsymbol{a}$) with various maximum temperatures. Figure (4.22) shows the relationship with varying thickness $\boldsymbol{h}$ with various maximum temperatures.

Figure (4.21) clearly shows that a smaller sliding length is necessary to prevent buckling with a maximum temperature of 2000 ˚C than with a minimum temperature of 500 ˚C, but not to the extreme that was found with a linear temperature distribution. The dependence on sliding length for avoidance of buckling nearly vanishes at around 60 millimeters. Figure (4.20) shows that central radius does not play an important role until it becomes quite large. Figure (4.22) shows that choosing an adequate thickness in the presence of a parabolic temperature distribution will prevent buckling for operating temperatures in most applications.

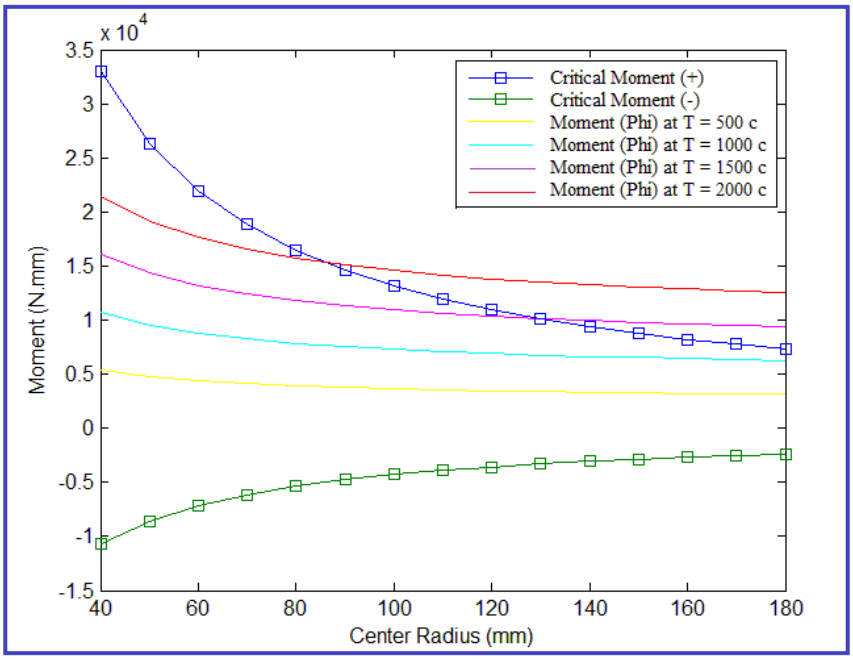

Figure 4.20: Relationship between actual moment and critical moments for parabolic temperature distributions with varying central radius

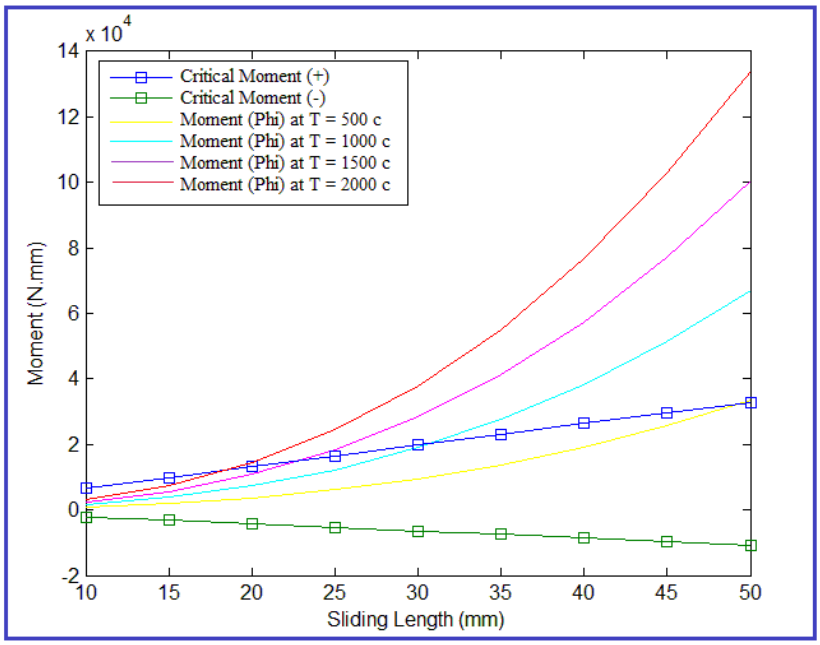

Figure 4.21: Relationship between actual moment and critical moments for parabolic temperature distributions with varying Sliding length

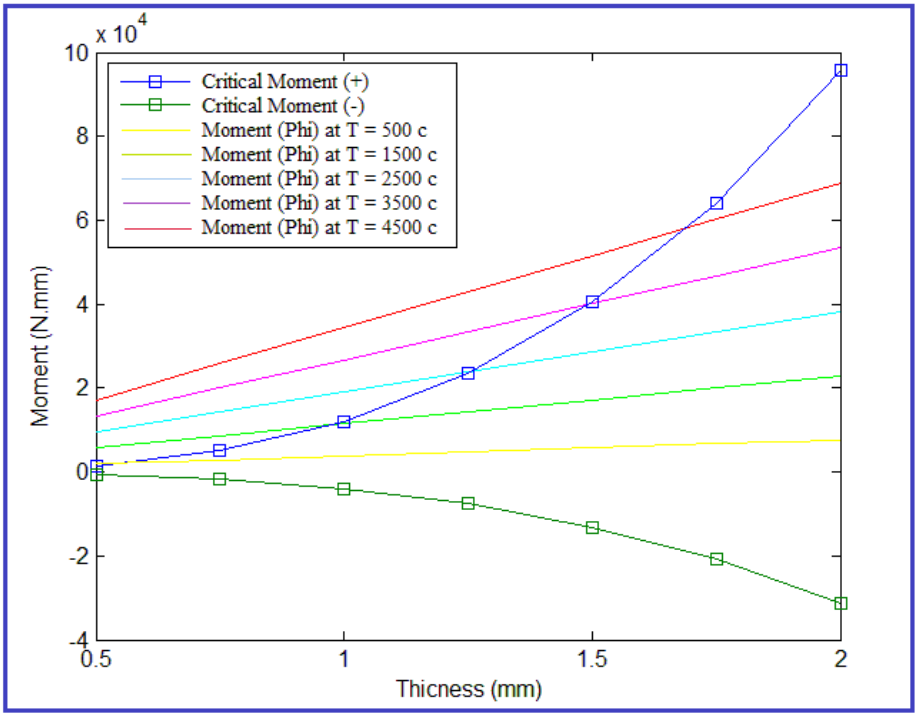

Figure 4.22: Relationship between actual moment and critical moments for parabolic temperature distributions with varying thickness

Figure (4.23) has shown the thermal buckling for cylindrical disk when the temperature is parabolic distribution at different sliding length, and Figure (4.25) has shown the thermal buckling for cylindrical disk when the temperature is parabolic distribution at different thickness. Table (4.5), and table (4.6) and corresponding Figure (4.24), and Figure (4.26) show comparison of the analytical and numerical results of our investigation for a parabolic temperature distribution. The numerical solution for varying sliding length produced lower critical moment and corresponding lower critical temperature. This is possibly due to additional complexities in the way that cooling is modelled within the software package used for numerical analysis. The numerical and analytical results for varying thickness proved nearly identical with only a slight divergence at larger thicknesses. The numerical results for varying central radius showed

no variation with change in central radius. This is likely due to the cross-sectional modeling remaining unchanging as the central radius changes.

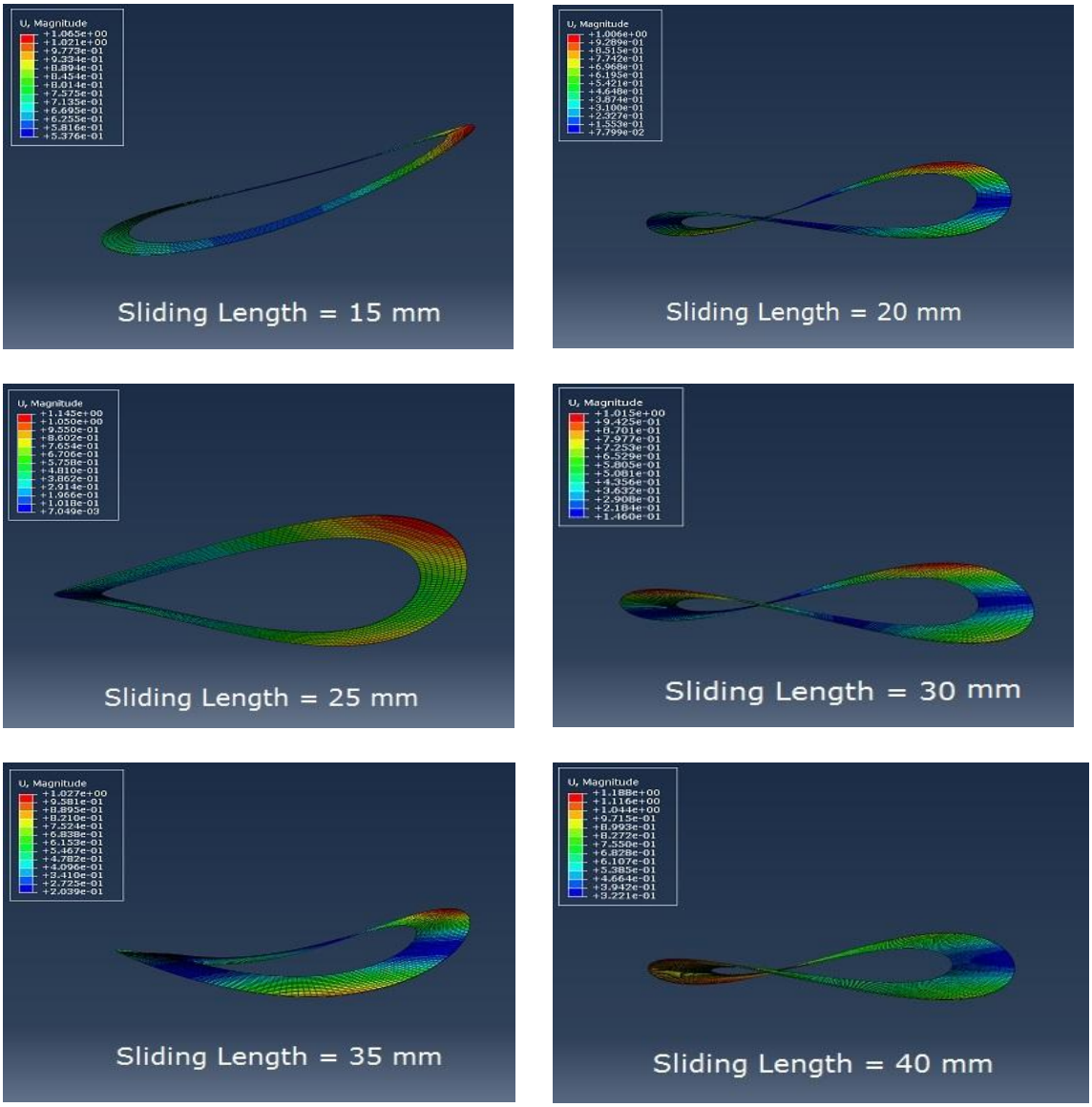

Figure 4.23: Deformation mode of thermal Buckling at different sliding length

Fixed parameters

Sliding length	Center Radius (R)	Thickness (h)	Young modules (E)	Thermal Expansion (α)
15 ~ 40 mm	110 mm	0.5 mm	$210x10^3$ N/mm^2	$12.5x10^{-6}$

Sliding Length	Ra	Rb	T(Analytical)	M (Analytical)	T(Numerical)	ʎ1	M (Numerical)
15	92.5	107.5	660	1.24	660	1	1.24
20	90	110	460	1.65	385	0.84	1.386
25	87.5	112.5	330	2.05	245	0.73	1.4965
30	85	115	260	2.47	160	0.62	1.5314
35	82.5	117.5	200	2.88	120	0.6	1.728
40	80	120	170	3.29	90	0.53	1.7437

Table 4.5: Modeling parameters for changing sliding length for parabolic temperature distribution

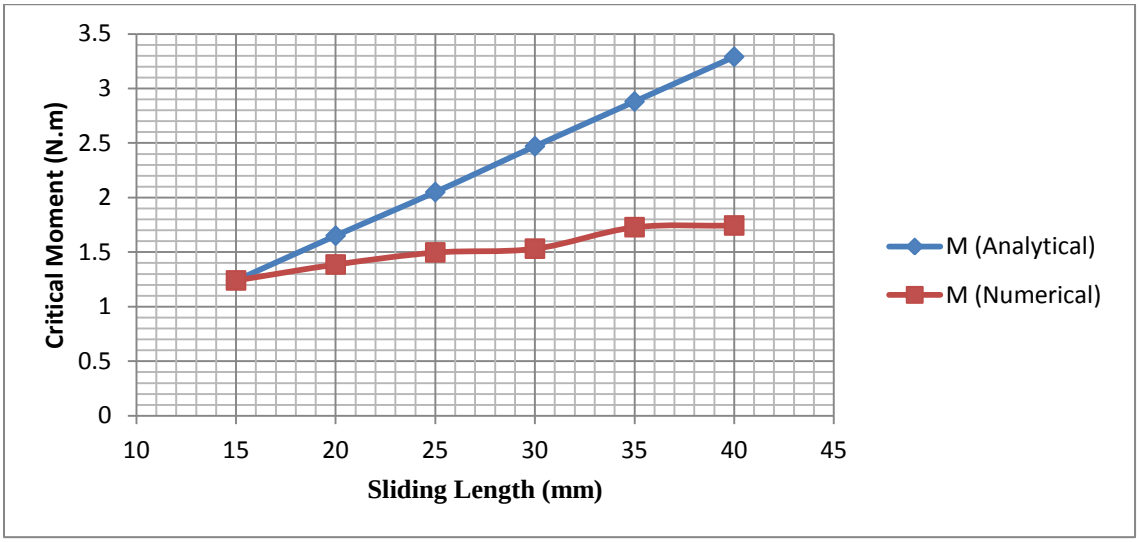

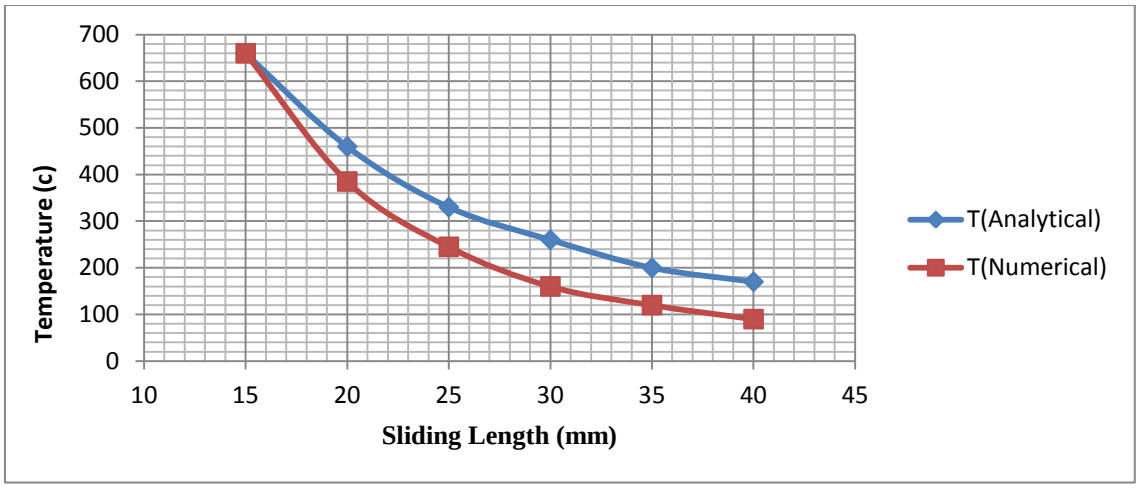

Figure 4.24: Analytical versus numerical results

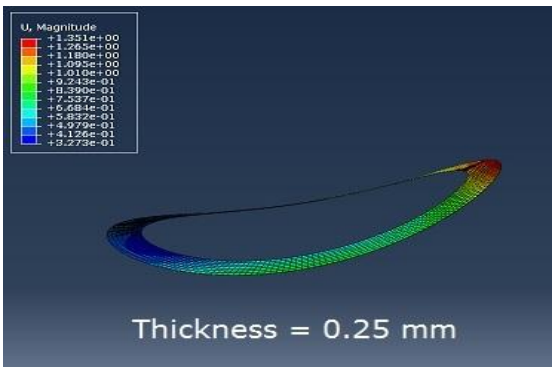

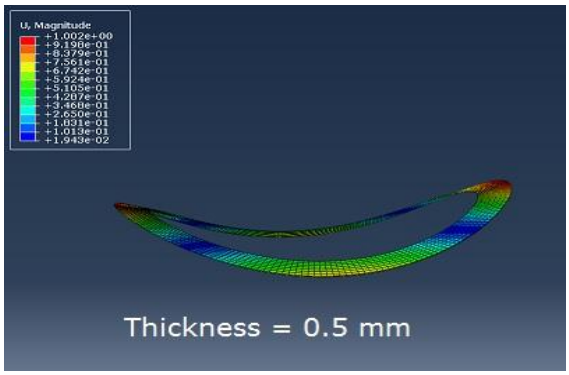

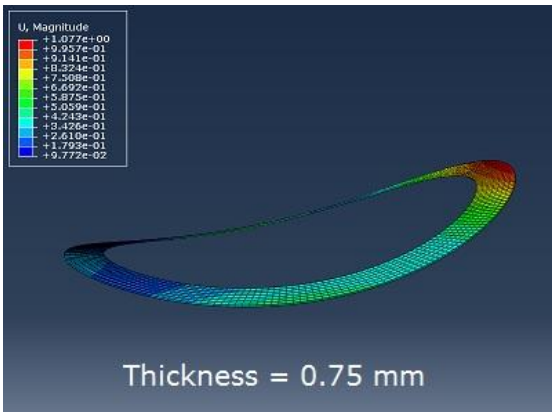

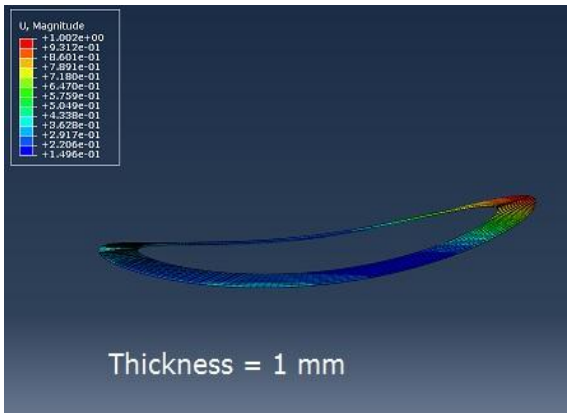

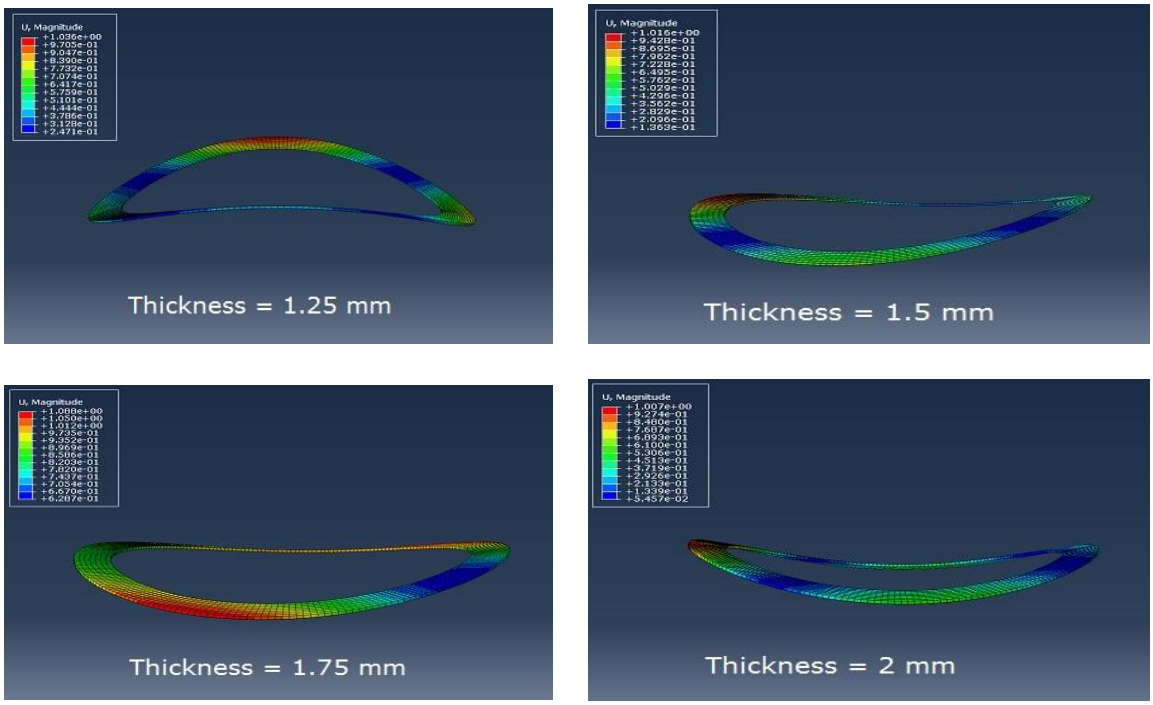

Figure 4.25: Deformation mode of thermal Buckling at different Thickness

Fixed parameters

Thickness (h)	Sliding length	Center Radius (R)	Young modules (E)	Thermal Expansion (α)
0.25 ~ 2 mm	20 mm	110 mm	$210x10^3$ N/mm^2	$12.5x10^{-6}$

H(mm)	Ra	Rb	T-A max	T-N max	M1(Analytical)	ʎ1	M1(Numerical)
0.25	100	120	98	95	0.187	0.97	0.18139
0.5	100	120	385	381	1.49	0.99	1.4751
0.75	100	120	880	855	5.05	0.97	4.8985
1	100	120	1560	1516	11.9	0.97	11.543
1.25	100	120	2450	2370	23.4	0.97	22.698
1.5	100	120	3530	3460	40.4	0.97	39.188
1.75	100	120	4800	4600	64.19	0.96	61.6224
2	100	120	6280	5980	95.8	0.95	91.01

Table 4.6: Modeling parameters for changing thickness (h) for parabolic temperature distribution

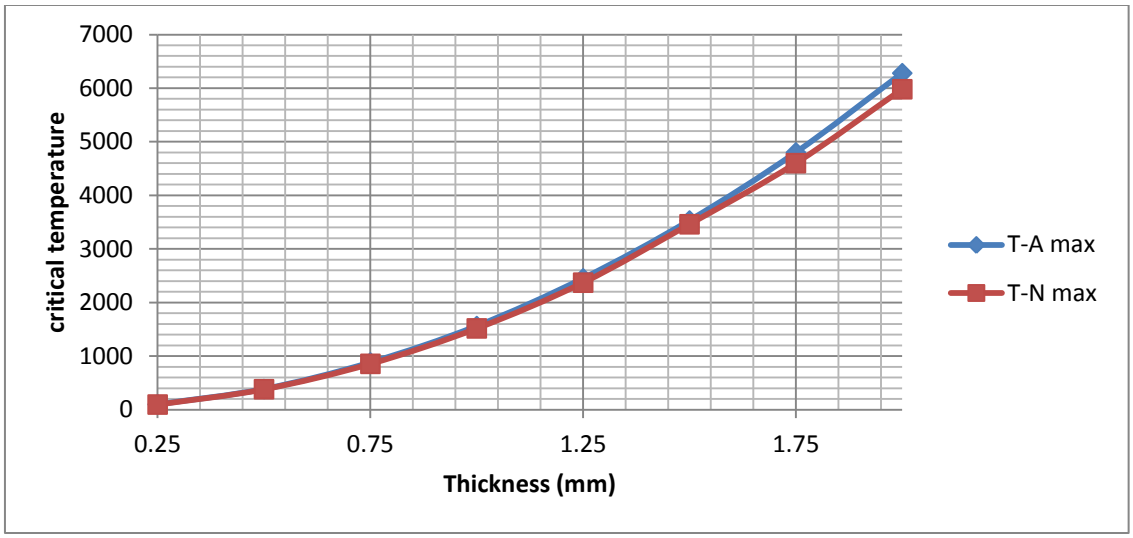

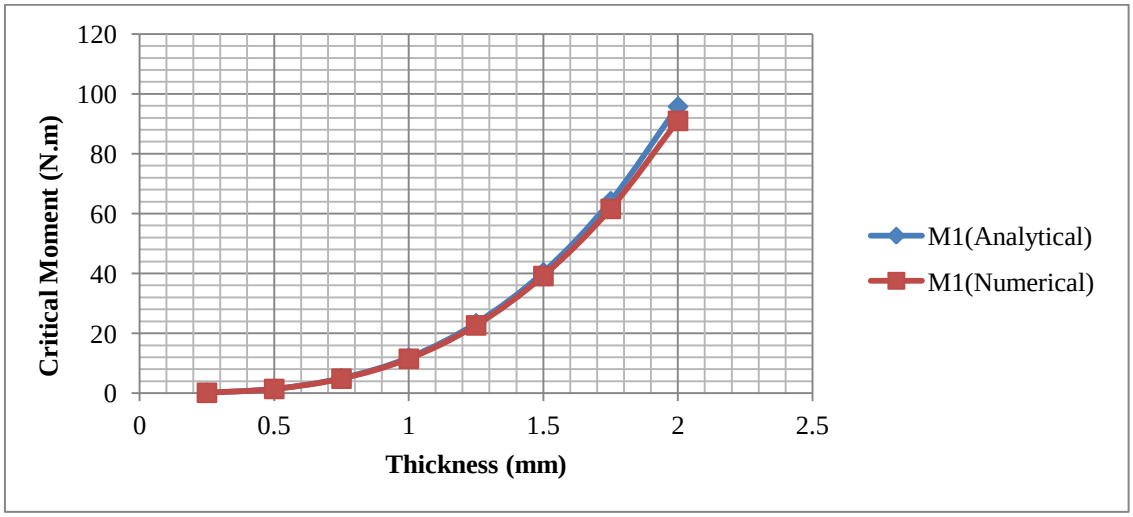

Figure 4.26: Analytical versus numerical results

4.3.3 Power Temperature Distribution

The power temperature distribution proved the most complex among the three distribution models considered. It involved a parabolic rise and fall in temperature from ***a*** to ***b***, as illustrated in Figure (4.27). This results in a model similar to the ABAQUS model shown in Figure (4.28). Numerous existing works focus on power temperature distributions [33 and 44]. The authors of [47] referenced the case study of the authors of

[48 and 49] when analyzing temperature distribution, indicating that the study found that higher temperature occurs at the center of a rotor surface and spread towards the circumferential direction. The thermograph imagery obtained during this study showed an increasing temperature radially with a power distribution appearance. The authors of [51] illustrated an excellent example of power temperature distribution and its changes through time although it is possible to interpret the illustration as a quite-skewed parabolic distribution, which seems to concur in the measurements and models of other similar works. The choice of consideration of power temperature distribution was based on its popularity and validity stemming from existing works as well as the considerable variance in temperature that it yields across the surface resulting in great buckling potential. In this work, power temperature distribution involved a fourth-order power increase in temperature from ***a*** to ***b***, though other orders could also be considered, such as a first-order, known as a linear temperature distribution.

$$T(r) = Tmin + \frac{(r-a)^4}{B}(Tmax - Tmin) \tag{4.16}$$

where

$$B = (b-a)^4$$

making

$$\int_a^r Tr\, dr = \frac{1}{30\,B}\big((Tmax - Tmin)(15a^4r^2 - 40a^3r^3 + 45a^2r^4 - 24ar^5 + 5r^6 -$$

$$a6+15B\,Tmin\,r2-a2 \tag{4.17}$$

Substituting (4.14) into (4.1) and (4.2) yields:

$$\sigma_r = -\frac{\alpha E}{r^2}\left[\frac{1}{30\,B}\left((Tmax - Tmin)(15a^4r^2 - 40a^3r^3 + 45a^2r^4 - 24ar^5 + 5r^6 - a^6) + \right.\right.$$

$$15B\,Tmin\,r2 - a2] + EC11 - v - EC21 + vr2 \qquad (4.18)$$

$$\sigma_\theta = \frac{\alpha E}{r^2}\left[\frac{1}{30\,B}\left((Tmax - Tmin)(15a^4r^2 - 40a^3r^3 + 45a^2r^4 - 24ar^5 + 5r^6 - a^6) + \right.\right.$$

$$15B\,Tmin\,r2 - a2] - \alpha E[Tmin + r - a4BTmax - Tmin] + EC11 - v + EC21 + vr2 \qquad (4.19)$$

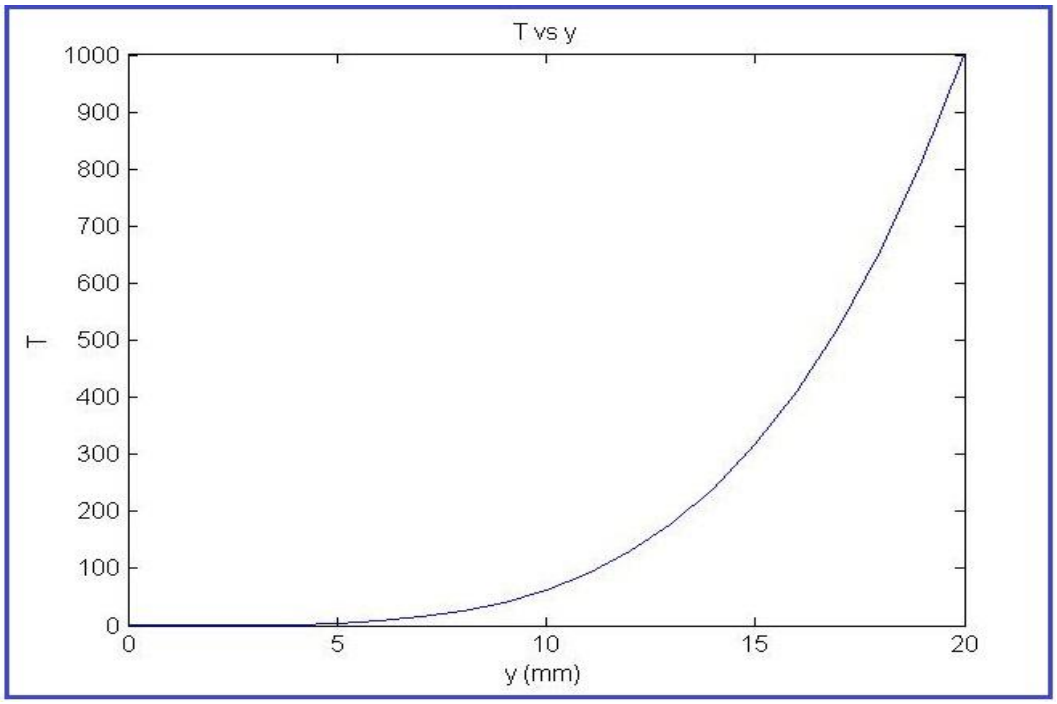

Figure 4.27: Power Temperature Distribution

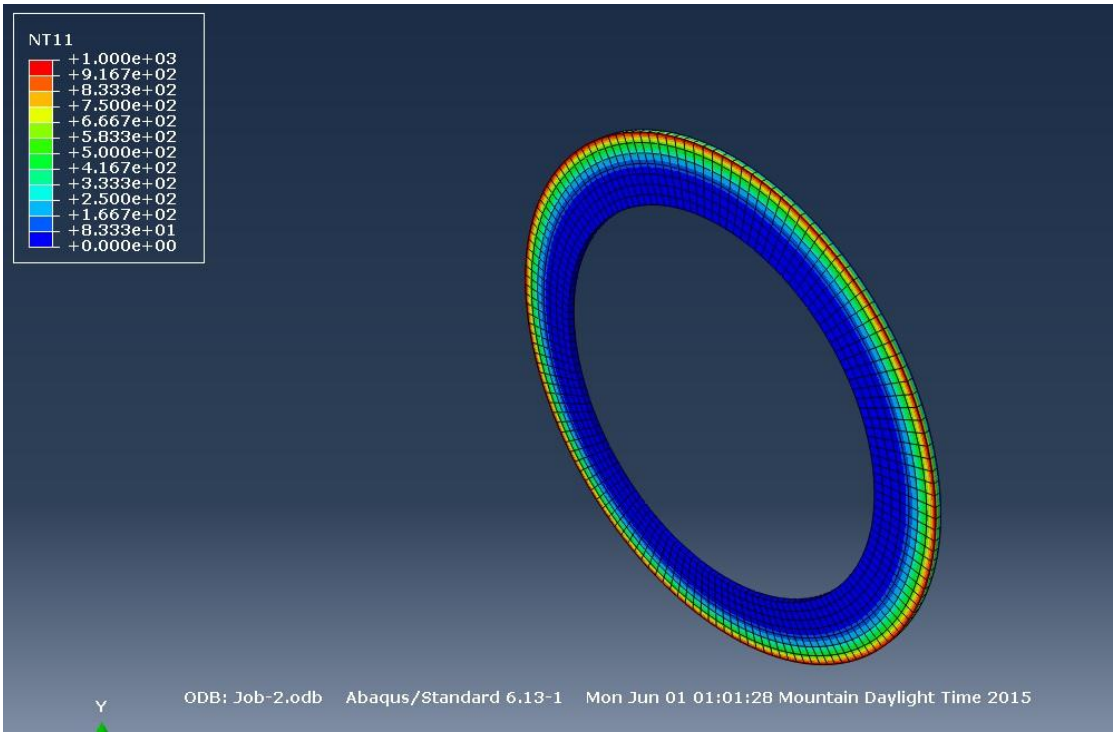

Figure 4-28: Power Temperature Distribution in Disc

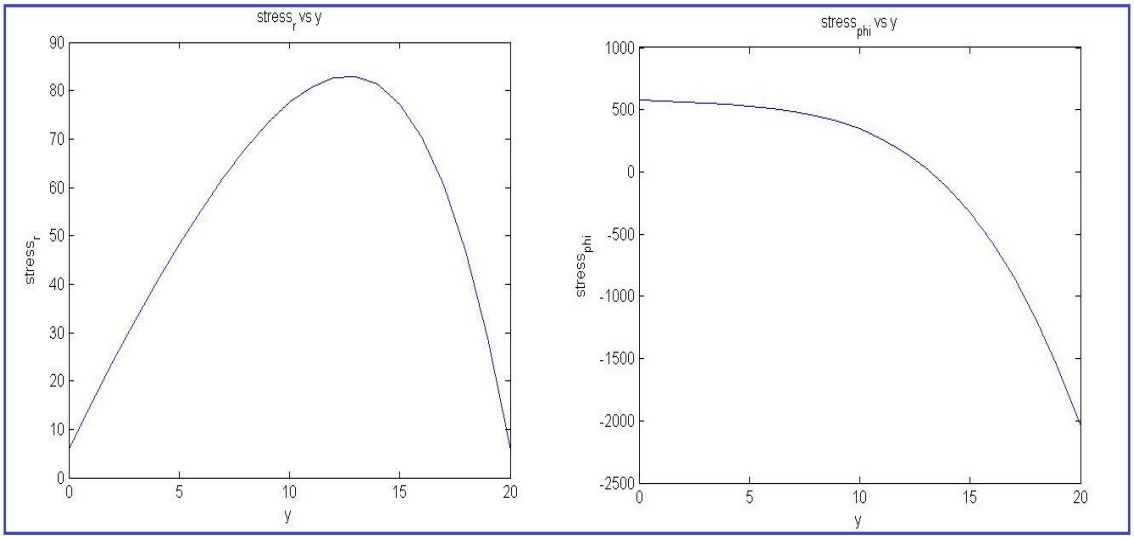

Figure 4.29: Stress Distributions for Power Temperature Distribution

These radial and tangential stresses for a power temperature distribution yield the curves shown in Figure (4.29). While the tangential stress is an order of magnitude

greater than the radial stress, it depends upon the resulting moment and its relationship to the critical moment for each direction as to whether or not buckling occurs. The sharp extremes in tangential stress across the radial axis indicate likelihood of buckling.

Substituting (19) into (4) yields the moments produced by tangential stress:

$$M_\theta = h\left[\int_a^b \sigma_\theta r\, dr - \int_a^b \sigma_\theta R\, dr\right] \tag{4.11}$$

where

$$\int_a^b \sigma_\theta\, r\, dr = \int_a^b \frac{\alpha E}{r}\left[\frac{1}{30\,B}\Big((Tmax - Tmin)\big(15a^4r^2 - 40a^3r^3 + 45a^2r^4 - 24ar^5 + 5r^6 - a6+15B\quad Tmin\quad r2-a2\quad dr-ab\alpha E[Tmin+r-a4B\quad Tmax-Tmin]r\, dr+abEC1r1-v+EC21+vr\, dr$$

$$\int_a^b \sigma_\theta R\, dr = \int_a^b \frac{\alpha ER}{r^2}\left[\frac{1}{30\,B}\Big((Tmax - Tmin)\big(15a^4r^2 - 40a^3r^3 + 45a^2r^4 - 24ar^5 + 5r^6 - a6+15B\quad Tmin\quad r2-a2dr-ab\alpha ERTmin+r-a4B\quad Tmax-Tmindr+abEC1R1-v+EC2R1+vr2\, dr$$

Graphing both critical moments from (4.5) with (4.11) show the relationships between critical moment and the produced moments. Figure (4.30) shows the relationship with varying central radius ***R*** with various maximum temperatures. Figure (4.31) shows the relationship with varying sliding length (***b***-***a***) with various maximum temperatures. Figure (4.32) shows the relationship with varying thickness ***h*** with various maximum temperatures.

Figure (4.31) clearly shows the necessity of a large sliding length compared with the linear and parabolic temperature models, although the necessity becomes greatly diminished for higher temperature differentials once an adequately large radial thickness

has been established. Figure (4.30) shows that maintaining a minimal central radius is critical for almost all temperature differentials. The window of function becomes so narrow that it will likely be unsafe to attempt even moderately-larger radii. Figure (4.32) shows that an adequate thickness will overcome the wide spread in moment ranges of different temperature distributions.

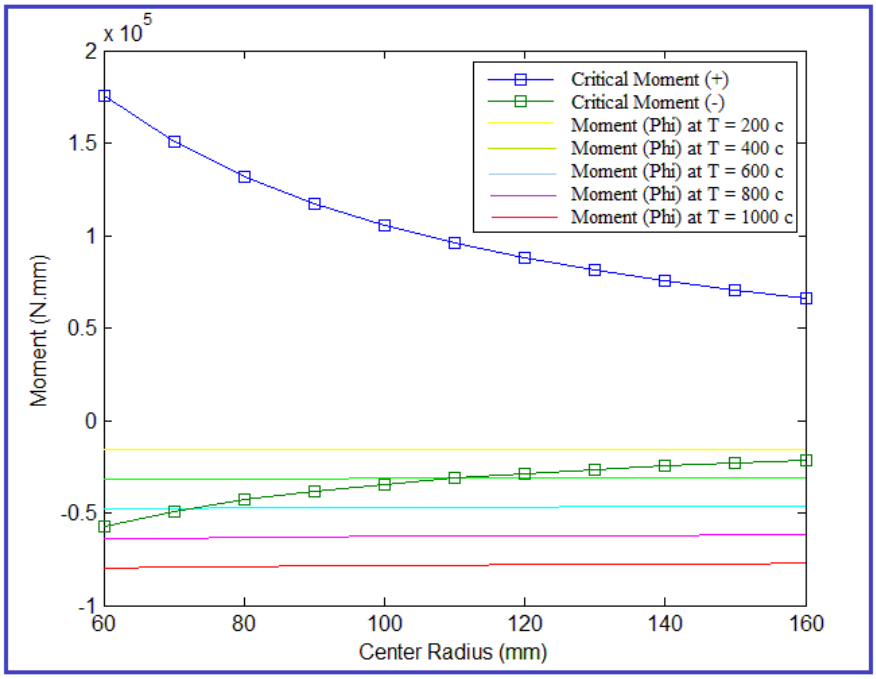

Figure 4.30: Relationship between actual moment and critical moments for power temperature distributions with varying central radius

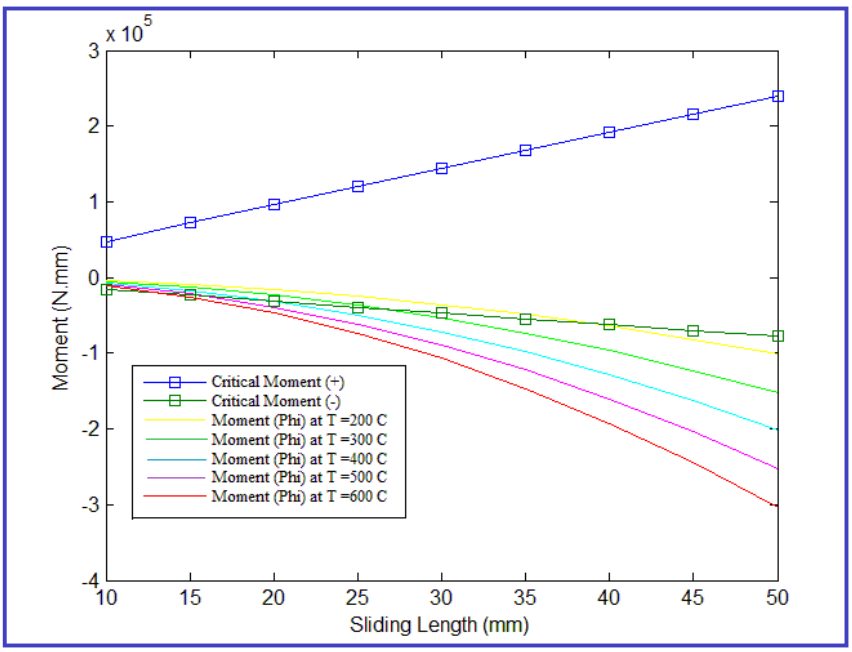

Figure 4.31: Relationship between actual moment and critical moments for power temperature distributions with varying Sliding length

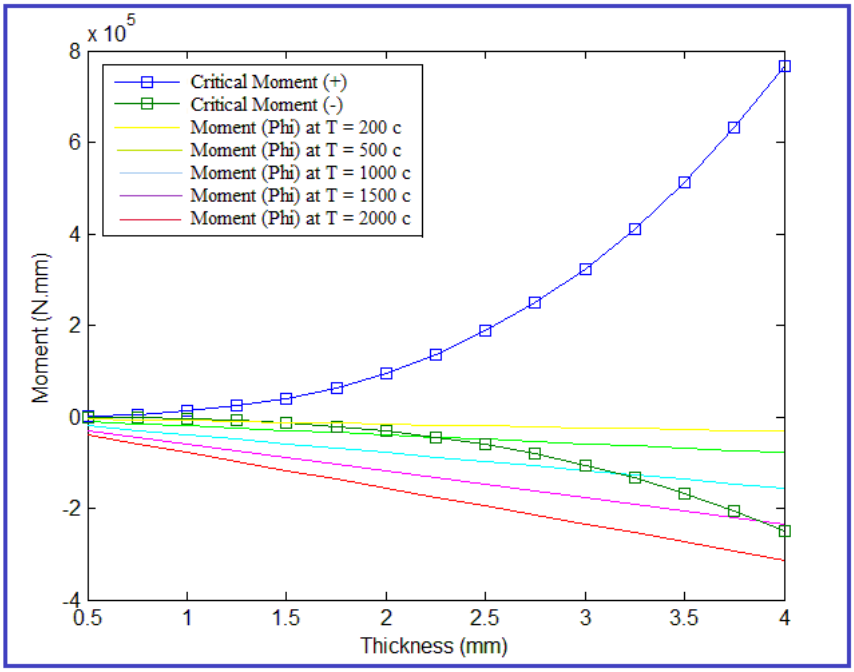

Figure 4.32: Relationship between actual moment and critical moments for power temperature distributions with varying thickness

Figure (4.33) has shown the thermal buckling for cylindrical disk when the temperature distribution is power at different center radius and Figure (4.35) has shown the thermal buckling for cylindrical disk when the temperature distribution is power at different sliding length and Figure (4.37) has shown the thermal buckling for cylindrical disk when the temperature distribution is power at different thickness.

Table (4.7), Table (4.8), and Table (4.9) and the corresponding Figure (4.34), Figure (4.36), and Figure (4.38) show comparisons of the analytical and numerical results of our experiment for a power temperature distribution. The results for varying central radius and radial thickness were fairly consistent between the analytical and numerical solutions with the numerical results diverging slightly for larger radial thicknesses. The numerical results for varying thickness showed a marked anomaly at larger thicknesses. This is likely due to the software package used for numerical analysis modelling the material differently at a larger thickness. The reason may be related to the different theories used in the two methods.

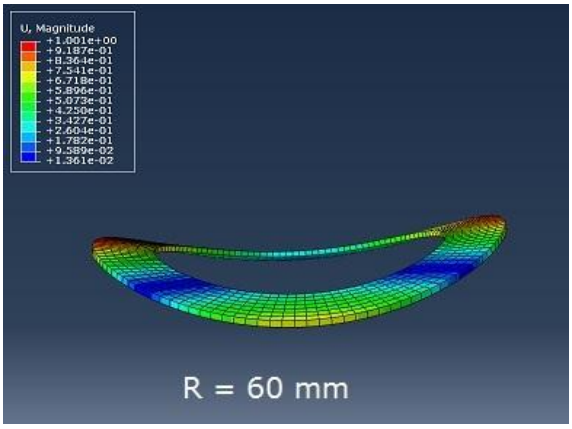

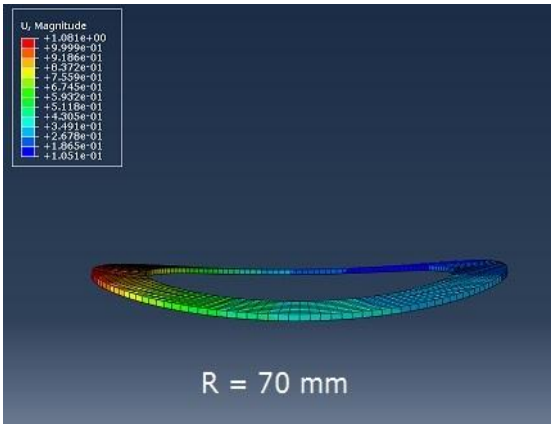

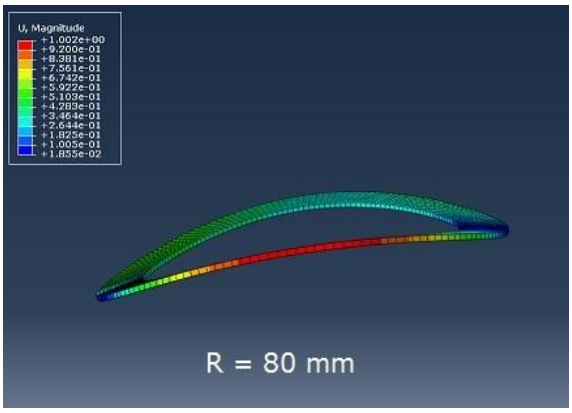
U, Magnitude
+1.002e+00
+9.200e-01
+8.381e-01
+7.561e-01
+6.742e-01
+5.922e-01
+5.103e-01
+4.283e-01
+3.464e-01
+2.644e-01
+1.825e-01
+1.005e-01
+1.855e-02
R = 80 mm

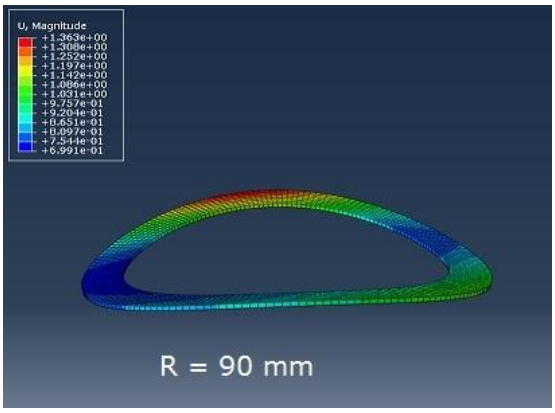
U, Magnitude
+1.363e+00
+1.308e+00
+1.252e+00
+1.197e+00
+1.142e+00
+1.086e+00
+1.031e+00
+9.757e-01
+9.204e-01
+8.651e-01
+8.097e-01
+7.544e-01
+6.991e-01
R = 90 mm

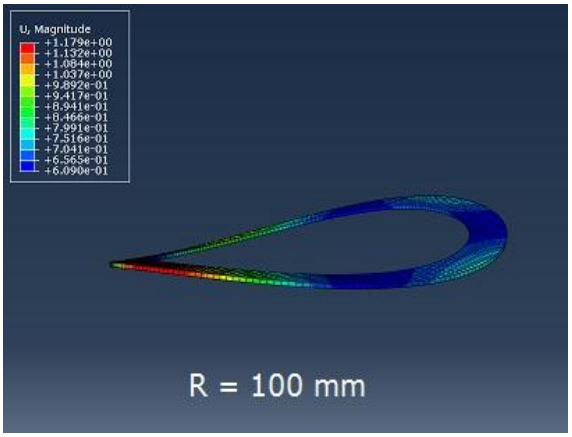
U, Magnitude
+1.179e+00
+1.132e+00
+1.084e+00
+1.037e+00
+9.892e-01
+9.417e-01
+8.941e-01
+8.466e-01
+7.991e-01
+7.516e-01
+7.041e-01
+6.565e-01
+6.090e-01
R = 100 mm

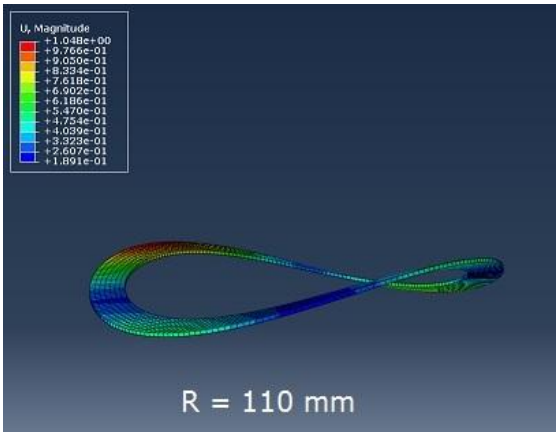
U, Magnitude
+1.04Be+00
+9.766e-01
+9.050e-01
+8.334e-01
+7.618e-01
+6.902e-01
+6.186e-01
+5.470e-01
+4.754e-01
+4.039e-01
+3.323e-01
+2.607e-01
+1.891e-01
R = 110 mm

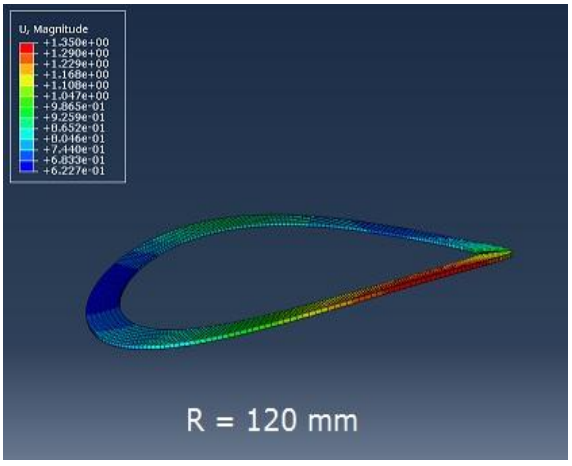
U, Magnitude
+1.350e+00
+1.290e+00
+1.229e+00
+1.168e+00
+1.108e+00
+1.047e+00
+9.865e-01
+9.259e-01
+8.652e-01
+8.046e-01
+7.440e-01
+6.833e-01
+6.227e-01
R = 120 mm

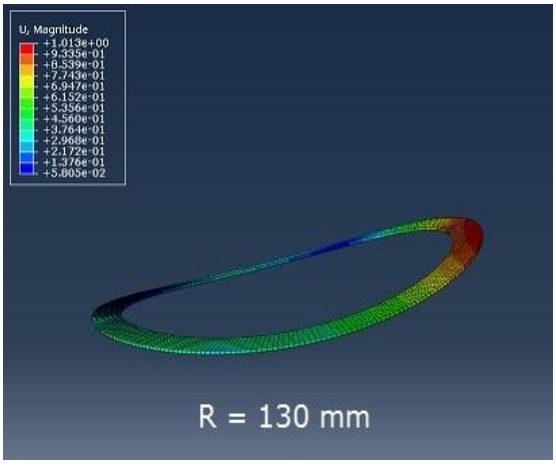
U, Magnitude
+1.013e+00
+9.335e-01
+8.539e-01
+7.743e-01
+6.947e-01
+6.152e-01
+5.356e-01
+4.560e-01
+3.764e-01
+2.968e-01
+2.172e-01
+1.376e-01
+5.805e-02
R = 130 mm

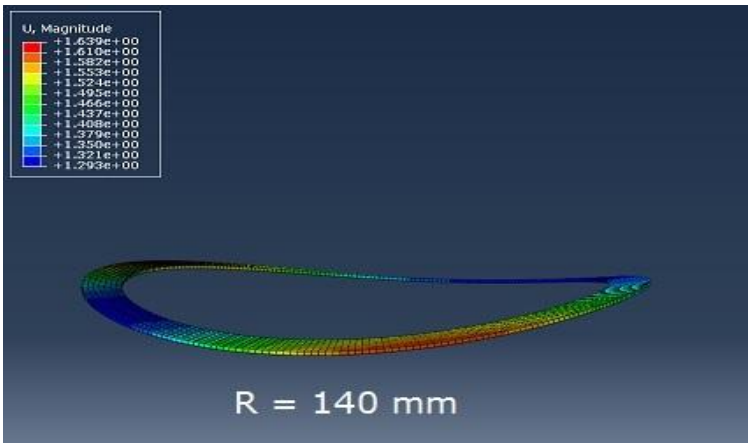

Figure 4.33: Deformation mode of thermal Buckling at different Center Radius

Fixed parameters

Center Radius (R)	Sliding length	Thickness (h)	Young modules (E)	Thermal Expansion (α)
60 ~ 140 mm	20 mm	2 mm	$210x10^3$ N/mm^2	$12.5x10^{-6}$

R (mm)	Ra	Rb	T(Analytical)	M (Analytical)	T(Numerical)	ʎ1	M (Numerical)
60	50	70	730	-57.2	757	1.036	-59.2592
70	60	80	630	-49	652	1.034	-50.666
80	70	90	545	-42.9	572	1.049	-45.0021
90	80	100	500	-38.14	510	1.02	-38.9028
100	90	110	450	-34.3	460	1.022	-35.0546
110	100	120	400	-31.2	419	1.04	-32.448
120	110	130	370	-28.6	384	1.03	-29.458
130	120	140	340	-26.41	355	1.044	-27.57204
140	130	150	317	-24.52	330	1.04	-25.5008

Table 4.7: Modelling parameters for changing central radius for power temperature distribution

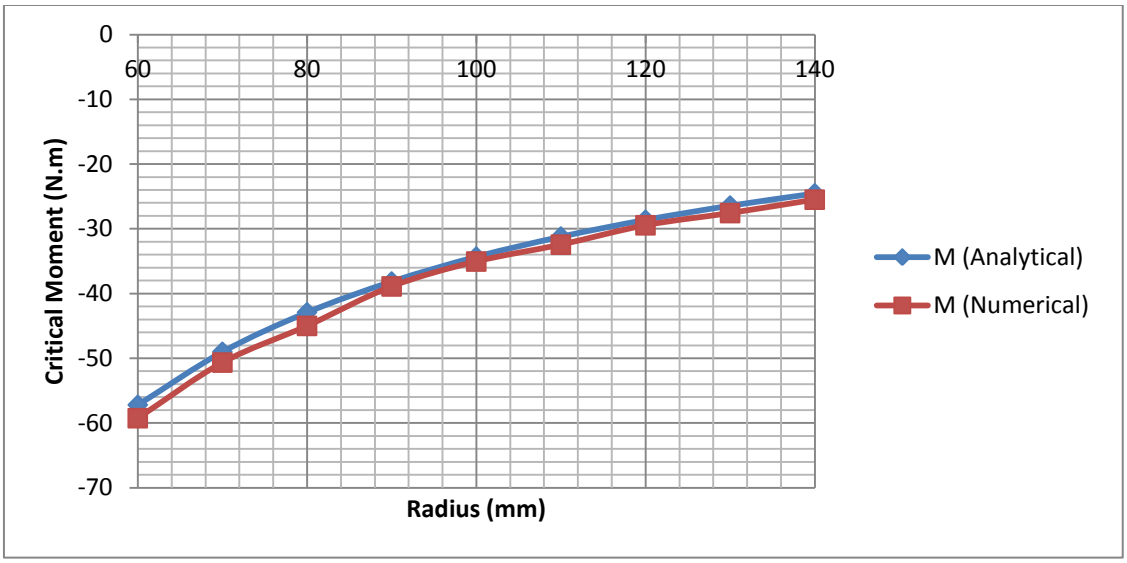

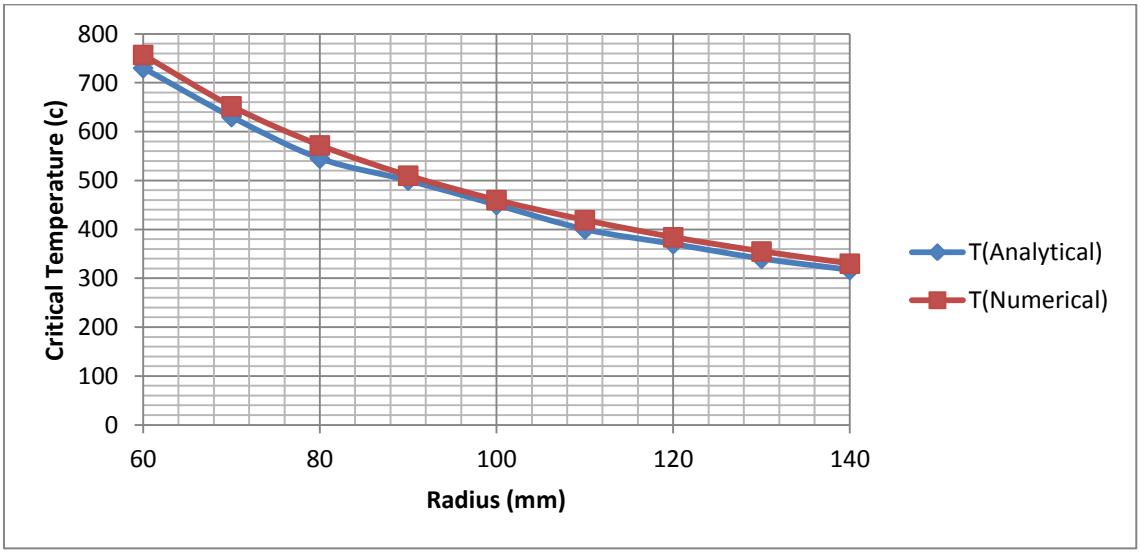

Figure 4.34: Analytical versus numerical results

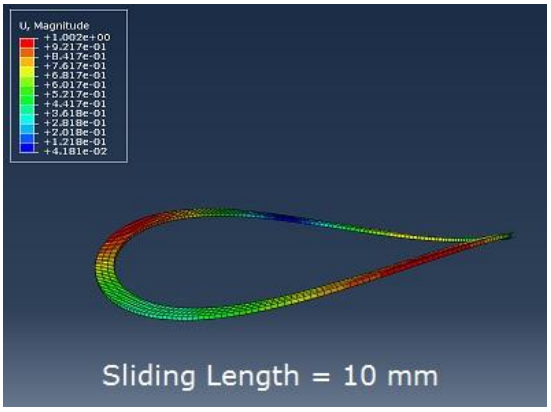
U, Magnitude
+1.002e+00
+9.217e-01
+8.417e-01
+7.617e-01
+6.817e-01
+6.017e-01
+5.217e-01
+4.417e-01
+3.618e-01
+2.818e-01
+2.018e-01
+1.218e-01
+4.181e-02
Sliding Length = 10 mm

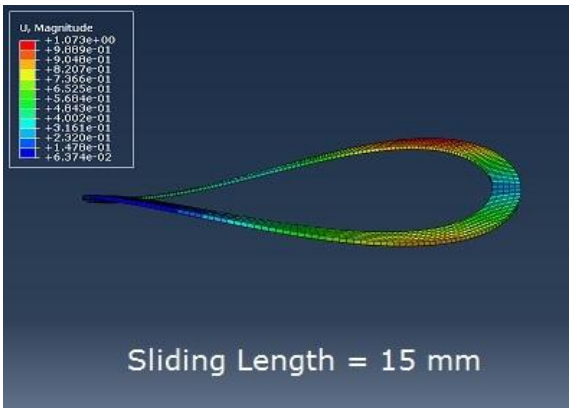
U, Magnitude
+1.073e+00
+9.889e-01
+9.048e-01
+8.207e-01
+7.366e-01
+6.525e-01
+5.684e-01
+4.843e-01
+4.002e-01
+3.161e-01
+2.320e-01
+1.478e-01
+6.374e-02
Sliding Length = 15 mm

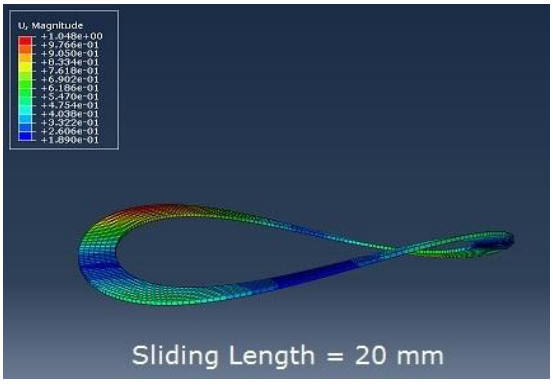
U, Magnitude
+1.048e+00
+9.766e-01
+9.050e-01
+8.334e-01
+7.618e-01
+6.902e-01
+6.186e-01
+5.470e-01
+4.754e-01
+4.038e-01
+3.322e-01
+2.606e-01
+1.890e-01
Sliding Length = 20 mm

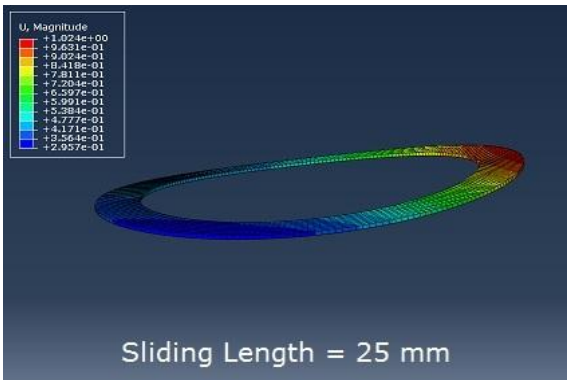
U, Magnitude
+1.024e+00
+9.631e-01
+9.024e-01
+8.418e-01
+7.811e-01
+7.204e-01
+6.597e-01
+5.991e-01
+5.384e-01
+4.777e-01
+4.171e-01
+3.564e-01
+2.957e-01
Sliding Length = 25 mm

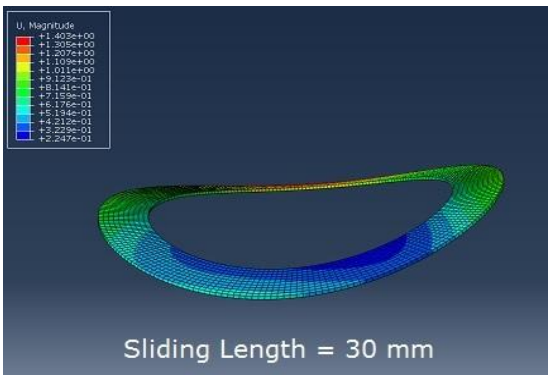
U, Magnitude
+1.403e+00
+1.305e+00
+1.207e+00
+1.109e+00
+1.011e+00
+9.129e-01
+8.141e-01
+7.159e-01
+6.176e-01
+5.194e-01
+4.212e-01
+3.229e-01
+2.247e-01
Sliding Length = 30 mm

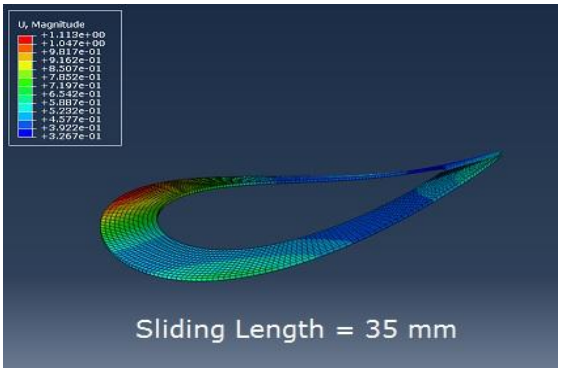
U, Magnitude
+1.119e+00
+1.047e+00
+9.817e-01
+9.162e-01
+8.507e-01
+7.852e-01
+7.197e-01
+6.542e-01
+5.887e-01
+5.232e-01
+4.577e-01
+3.922e-01
+3.267e-01
Sliding Length = 35 mm

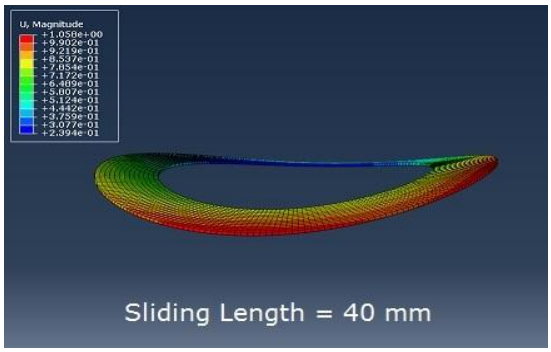
U, Magnitude
+1.058e+00
+9.902e-01
+9.219e-01
+8.537e-01
+7.854e-01
+7.172e-01
+6.489e-01
+5.807e-01
+5.124e-01
+4.442e-01
+3.759e-01
+3.077e-01
+2.394e-01
Sliding Length = 40 mm

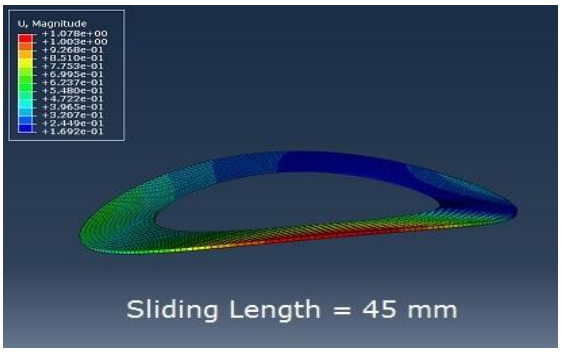
U, Magnitude
+1.078e+00
+1.003e+00
+9.268e-01
+8.510e-01
+7.753e-01
+6.995e-01
+6.237e-01
+5.480e-01
+4.722e-01
+3.965e-01
+3.207e-01
+2.449e-01
+1.692e-01
Sliding Length = 45 mm

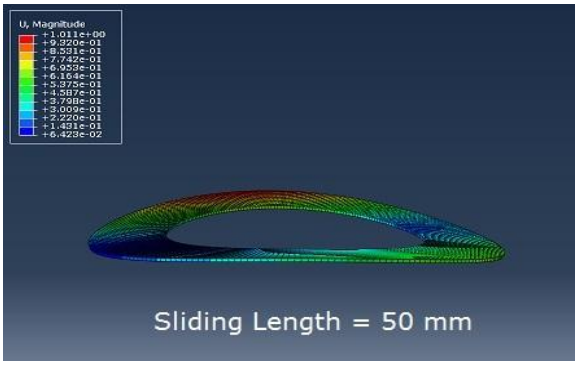

Figure 4.35: Shows thermal Buckling at different sliding length

Fixed parameters

Sliding Length	Center Radius (R)	Thickness (h)	Young modules (E)	Thermal Expansion (α)
10 ~ 50 mm	110 mm	2 mm	210x10^3 N/mm^2	12.5x10^{-6}

Sliding length mm	Ra	Rb	T (Analytical)	M (Analytical)	T (Numerical)	ʎ1	M (Numerical)
10	105	115	800	-15.6	763	0.95	-14.82
15	102.5	117.5	540	-23.4	547	1.012	-23.6808
20	100	120	400	-31.2	419	1.04	-32.448
25	97.5	122.5	327	-39.01	336	1.027	-40.06327
30	95	125	263	-46.8	281	1.06	-49.608
35	92.5	127.5	224	-54.6	241	1.07	-58.422
40	90	130	195	-62.4	210	1.076	-67.1424
45	87.5	132.5	173	-70.2	187	1.08	-75.816
50	85	135	155	-78	168	1.083	-84.474

Table 4.8: Modelling parameters for changing sliding length for power temperature distribution

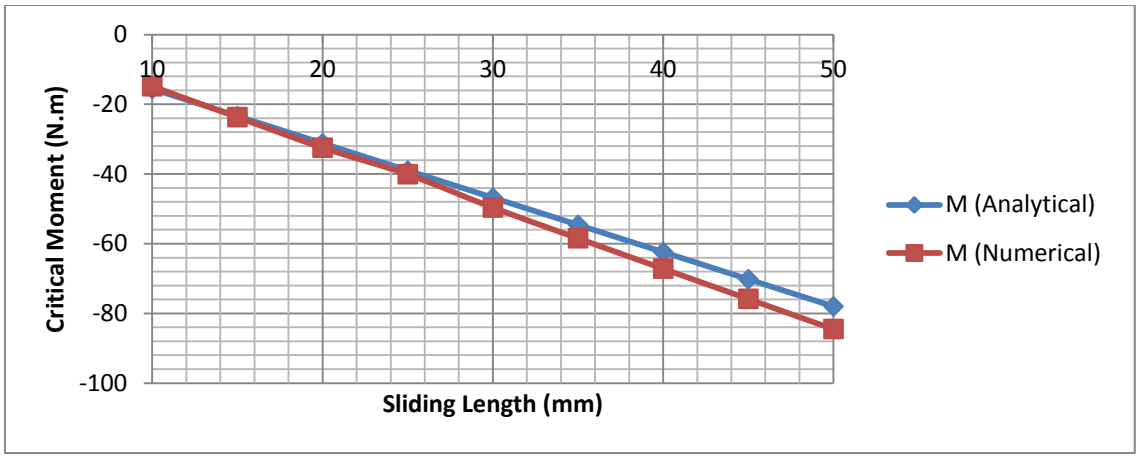

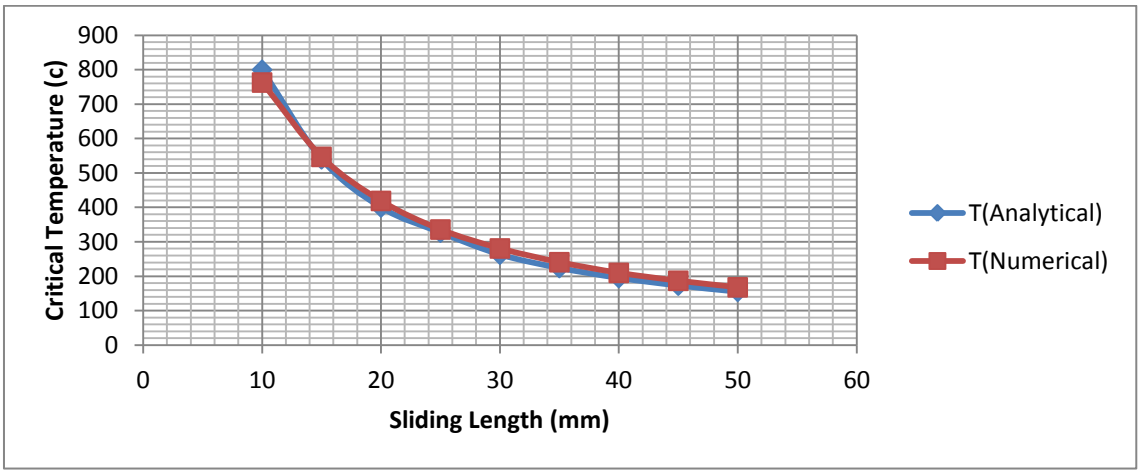

Figure 4.36: Analytical versus numerical results

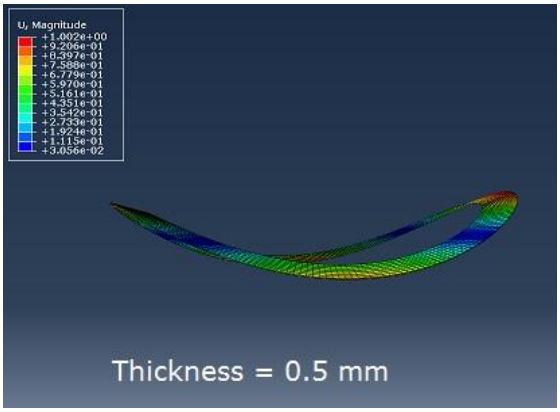

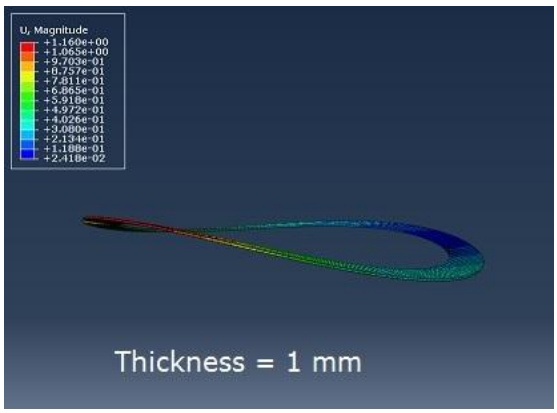

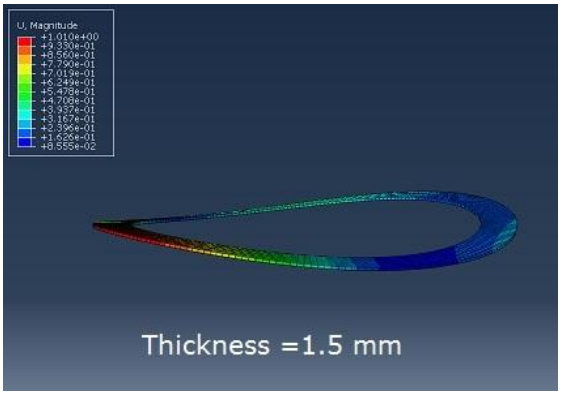
U, Magnitude
Thickness =1.5 mm

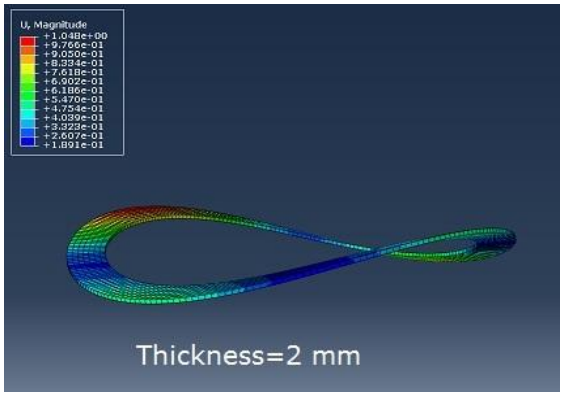
U, Magnitude
Thickness=2 mm

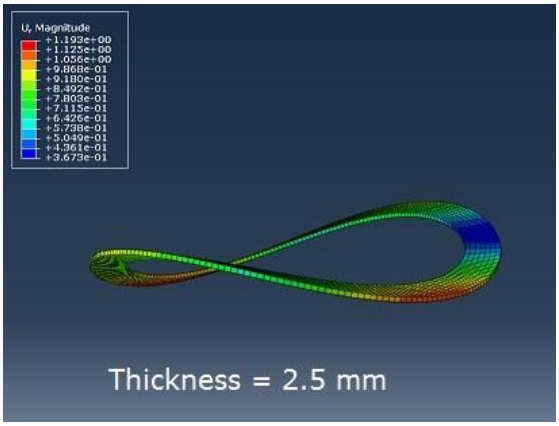
U, Magnitude
Thickness = 2.5 mm

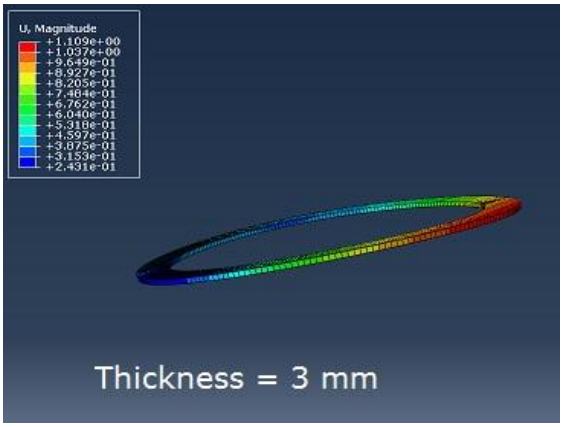
U, Magnitude
Thickness = 3 mm

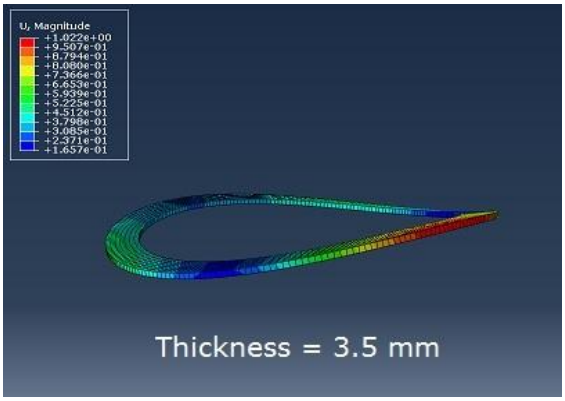
U, Magnitude
Thickness = 3.5 mm

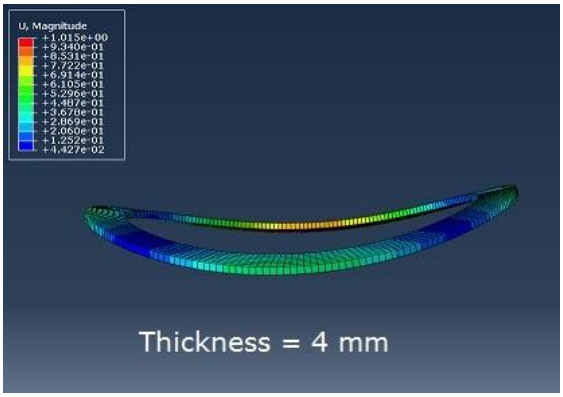
U, Magnitude
Thickness = 4 mm

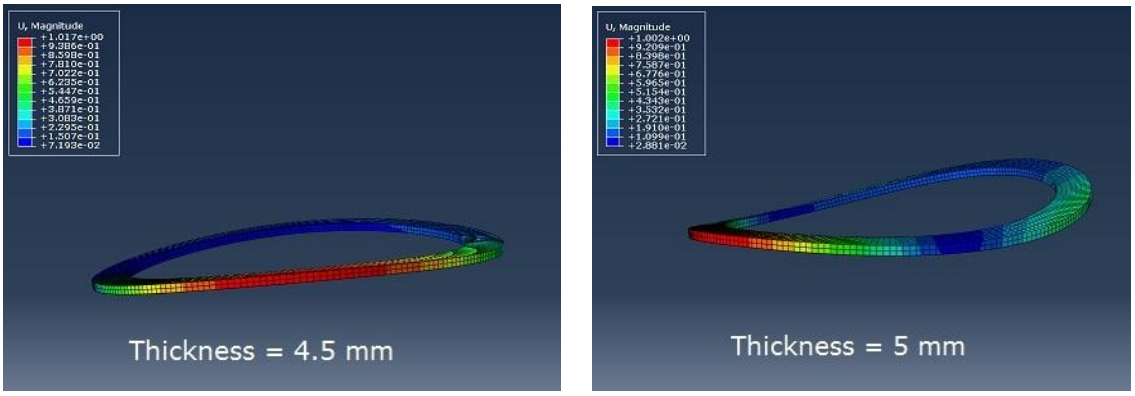

Figure 4.37: Shows thermal Buckling at different Thickness

Fixed parameters

Thickness (h)	Sliding length	R	Young modules (E)	Thermal Expansion (α)
0.5 ~ 5 mm	20 mm	110 mm	210x10^3 N/mm^2	12.5x10^{-6}

Thickness (mm)	Ra	Rb	T (Analytical)	M (Analytical)	T (Numerical)	ʎ1	M (Numerical)
0.5	100	120	25	-0.487	26	1.04	-0.50648
1	100	120	100	-3.9	105	1.05	-4.095
1.5	100	120	226	-13.16	237	1.05	-13.818
2	100	120	400	-31.2	419	1.05	-32.76
2.5	100	120	630	-60.9	650	1.03	-62.727
3	100	120	900	-105.3	929	1.03	-108.459
3.5	100	120	1225	-167.2	1255	1.02	-170.544
4	100	120	1600	-249.6	1626	1.02	-254.592
4.5	100	120	2100	-355.5	3500	1.6	-568.8
5	100	120	2600	-487.6	5000	1.9	-926.44

Table 4.9: Modelling parameters for changing thickness (h) for power temperature distribution

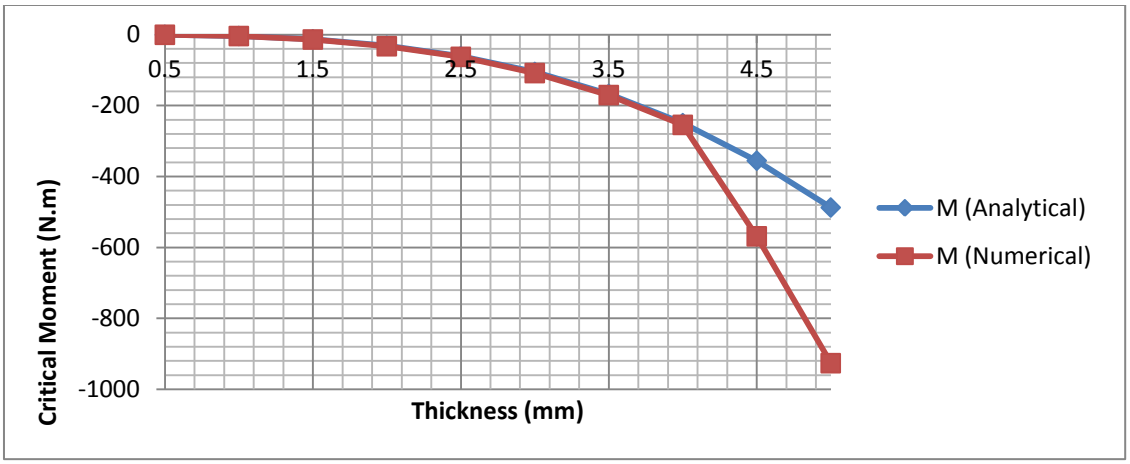

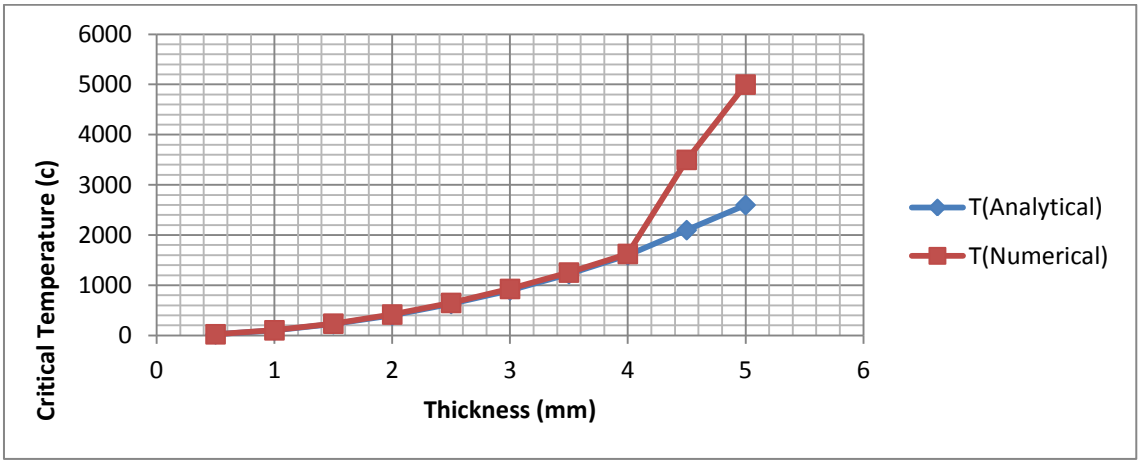

Figure 4-38: Analytical versus numerical results

4.4 Summary and Conclusions

Friction disc systems are always subject to constraints of heat dissipation and material limitations. Of particular concern is the non-homogeneity of the temperature field inside friction discs that causes thermal stresses that can lead to hot spots and eventually failure due to thermoelastic distortion that results in buckling. Many disassembled systems have found “cone” or “potato chip” deformations out-of-plane of the disc. These two modes of deformation show very distinct patterns of distortion related

to variations in thermoelastic stress along the radial and circumferential/tangential axes. It is from these concepts that we modelled our disc for experimentation in variations of temperature distribution and system configuration parameters.

Based on the related, proven mechanical and thermal concepts, we utilized the relationships between thermal distribution and generation of moments in the radial and tangential directions and compared such moments with critical moments that indicate buckling, which allowed us to model conditions under which buckling would occur and experiment with various system parameters and three primary thermal distribution models (linear, parabolic, and power) to draw conclusions regarding the relationships of material and geometric configurations to indicated temperature distribution. When a critical moment was exceeded in either the radial or tangential direction, buckling occurred. Adjustments in system geometry and material properties allowed for higher temperature variations before the onset of buckling. In the linear temperature distribution case, thickness was the primary controlling factor of buckling with central radius and radial thickness being less sensitive in regards to buckling. In the parabolic temperature distribution case, central was the primary controlling factor for buckling while radial thickness and thickness were far less sensitive. While in the power temperature distribution case, both central radius and radial thickness exhibited strong control over buckling while thickness was much less sensitive. Overall, these results were conclusive and expected though some of the narrowness of windows for parameter change were quite small.

We believe that the models relayed herein are generalizable for other specific situations and that the approaches and findings presented show strong and recognizable indications of buckling conditions and how to avoid buckling. We believe that future endeavors that follow paths based on the theoretical models and proven mechanical and thermal properties upon which our conclusions were based should provide conclusive physical evidence of the indications shown in this work. It is our hope that the models and approaches detailed and discussed provide clear direction and thought regarding design constraints and modelling of frictional disc systems and other similarly-conditioned thermal-mechanical systems.

CHAPTER 5

Conclusions and Future Work

5.1 Conclusions

Several, interrelated objectives were undertaken and accomplished within this work. A current understanding of thermoelastic instability (TEI) and the mechanism of convective cooling on TEI with specific focus on the use of finite element analysis (FEA) was first established. This was followed by the development of a finite element model (FEM) for the frictionally-excited thermoelastic instability problem in intermittent sliding contact with finite geometries and realistic friction materials along with validating the model in several limiting cases using analytical solutions. This was followed by the establishment a current understanding of thermal buckling and its associated behavior in regard to rotor discs, specifically in regards to modes of failure, and the presentation of results and discussion of an analytical experiment with established material properties and thermal loadings where properties of disc geometry were varied.

In regards to the first objective, the phenomenon of frictionally-excited thermoelastic instability and thermal buckling in automotive disc brakes and clutches were investigated both theoretically and numerically. A finite element method was implemented to investigate the effect of convective cooling on the stability boundaries of thermo- elastic instability in a couple of representative brake and clutch systems. By

adding a negative term representing the convective heat dissipation to the frictional heat generation rate, convective cooling is successfully incorporated into the finite element formulation. This is analogous to a system with a reduced frictional heat rate and, therefore, can stabilize the thermal–mechanical process. As a consequence, it has been found that previous analyses of TEI typically overestimated critical sliding speeds. Liquid cooling such as water and lubricants removes heat at a much faster rate than gases such as air, and therefore affect system stability more significantly. The parametric studies have shown that the critical speed in some cases where the water cools the system can be three times as high as the value without convective cooling. However, the wave number corresponding to the lowest critical speed is nearly independent of the convection effect. This implies that the dominant mode pattern at a given sliding speed remains unchanged as well. Further, in comparison with linear elements, quadratic elements are capable of accurately capturing the oscillatory patterns of temperature in the vicinity of the friction interface and therefore provide a better numerical accuracy with the same computational effort. Although using quadratic elements is not necessary for lower dimensions, it will potentially permit efficient solutions for problems defined in higher dimensions.

In regards to the second objective, a finite element scheme based on the eigenvalue method was implemented for the analysis of thermoelastic instability in intermittent sliding contact with practical model parameters. A numerical algorithm was developed to determine critical velocities by tracking eigenmode patterns and corresponding growth rates. The method was validated by both analytical and numerical solutions in some limiting situations. It was concluded that when realistic materials and

geometric configurations were considered for intermittent contact, neither the strategy of time-averaged heat input nor the analytical solution derived from the half-plane model work properly. Finite element analyses revealed a bell-shaped relationship between dimensionless critical speed and wavelength: for longer waves the dimensionless critical speed approaches zero rather than unity; for shorter waves the critical speed is much lower than that predicted by the analytical half-plane solution. There exists a location where the dimensionless critical speed is the maximum. In general, the strategy of averaging the heat input over the entire circumference is appropriate only when the period of frictional contact is longer than the period of separation, and when the peak value of the dimensionless critical speed is our primary concern.

In regards to the fourth objective, friction disc systems have ever been subject to constraints of heat dissipation and material limitations. Of particular concern is the non-homogeneity of the temperature field inside friction discs that causes thermal stresses that can lead to hot spots and eventually failure due to thermoelastic distortion that results in buckling. Many disassembled systems have found “cone” or “potato chip” deformations out-of-plane of the disc. These two modes of deformation show very distinct patterns of distortion related to variations in thermoelastic stress along the radial and circumferential/tangential axes. It is from these concepts that we modelled our disc for experimentation in variations of temperature distribution and system configuration parameters. Based on the proven mechanical and thermal concepts, we utilized the relationships between thermal distribution and generation of moments in the radial and tangential directions and compared such moments with critical moments that indicate

buckling, which allowed us to model conditions under which buckling would occur and experiment with various system parameters and three primary thermal distribution models (linear, parabolic, and power) to draw conclusions regarding the relationships of material and geometric configurations based on the given temperature distribution. When a critical moment of appropriate direction was exceeded in either the radial or tangential directions, buckling took place. Adjustments in system geometry and material properties allowed for higher temperature variations before the onset of buckling. In the linear temperature distribution case, thickness was the primary controlling factor of buckling with central radius and radial thickness being less sensitive in regards to buckling. In the parabolic temperature distribution case, the central radius does not play an important role until it becomes quite large. While radial thickness and thickness were more sensitive. While in the power temperature distribution case, both central radius and radial thickness exhibited strong control over buckling while thickness was much less sensitive. Overall, these results were conclusive and expected though some of the narrowness of windows for parameter change were quite small.

In conclusion, we believe that the models and analyses relayed herein are generalizable for other specific situations and that the approaches and findings present specific evidence of the general outcomes. We also believe that future endeavors that follow paths based on the theoretical models and proven mechanical and thermal properties upon which our conclusions were based should provide conclusive evidence of the indications shown in this work. It is our hope that the models and approaches detailed and discussed provide clear direction and thought regarding design constraints and

modelling of frictional disc systems and other similarly-conditioned thermal-mechanical systems.

5.2 Future work

The methods, observations, analyses, and conclusions presented within work lead to suggestions of expansion for future endeavors. Some of these come as direct variations in properties or subjects of the current work, while others are suggested by limitations due to assumption or structure within the current work.

5.2.1 Experimental Verifications

Analytical and numerical methods were used in this study on thermal buckling of an annular disc. The results show the possible buckling loads and modes for certain conditions. However, no experimental verifications were performed to verify the findings from this study. These experimental verifications would not only provide further support to the validity of this work, but potentially yield new areas for exploration or further caveats for modeling.

5.2.2 Increased Model Complexity

In the present work of thermal analysis of disc brakes and clutches, a simplified model of the discs without any vents has been used. In the future work, a more complex model with ventilated disc could be taken into consideration and thereby forced convection would be involved in the analysis. The linear, parabolic and power temperature distributions have been investigated and compared with the numerical results assuming linear elasticity. In the future it is suggested to investigate the elastoplastic

buckling performance along with more practical loading conditions and geometric structures. Also the effect of periodic temperature distribution along the circumference on the critical buckling temperature and the thermal stresses could be investigated.

5.2.3 Material Variance

The current work is limited to particular materials and structures with specific properties. More complex materials could be considered including multi-layered materials and composite materials. Such efforts would expand the scope of this work into additional domains to allow a greater understanding of buckling across materials to enable better material choices and designs.

5.2.4 Additional Temperature Models

The current work styles temperature models based on classical patterns that have existing research and applications from which to draw information and comparisons. Additional temperature models could be considered, which could include sinusoidal or reverse-parabolic models, among others.

5.2.5 Dimensional Variations

The current work investigates temperature, moments, and buckling primarily in the spatial domain. Future endeavors could investigate buckling with time to allow variations in loading with time as well as other complex effects that vary with time. These investigations would allow a greater understanding of the developing conditions of buckling along with the effects of applied physical forces that could accelerate, decelerate, or perturb buckling behaviors.

5.2.6 TEI and Buckling

The models of TEI and buckling on cylindrical disk systems could be comparatively investigated to understand the influences of the two models and the separate and collective implications they bring. These investigations would allow a more unified understanding of thermal modeling and potentially lead to combinational or alternative models.

Publication

1. Yun-Bo Yi , Ali.Bendawi , “Effect of convective cooling on frictionally excited thermoelastic instability “, Wear 296 pp. 583–589 (2012) (published)
2. Yun-Bo Yi, Ali Bendawi, Heyan Li, and Jiaxin Zhao “ Fininte element analysis of thermoelastic instability in intermittent sliding contact “ , Journal of Thermal Stresses 37, pp. 670 – 883 (2014) (published)
3. Ali Bendawi, Yun-Bo Yi, Heyan Li “ Buckling of cylindrical Disk due to thermal stress”, International Journal of Vehicle Engineering. (submitted)
4. Zhuo Chen, Ali Bendawi, Yun-Bo Yi, “A reduced Fourier model for prediction of thermal buckling”, in preparation.

References

[1] Yi, Y. B., (2001), "Thermoelastic Instability in Automotive Brakes and Clutches." Ph.D. Dissertation., the University Of Michigan.

[2] Barber, J.R., (1969), "Thermoelastic instabilities in the sliding of conforming solids." Proceedings of the Royal Society of London, Series A 312, pp. 381–394.

[3] Lee, K.J., Barber, J.R., (1993), "Frictionally-excited thermoelastic instability in automotive disk brakes", ASME Journal of Tribology 115: 607–614.

[4] Afferrante, L., Ciavarella, M., Barber, J.R., (2006), "Thermoelastodynamic instability (TEDI): a new mechanism for sliding instability", Proceedings of the Royal Society of London Series A 462: 2161–2176.

[5] Du, S., Zagrodzki, P., Barber, J.R., Hulbert, G.M., (1997), "Finite element analysis of frictionally-excited thermoelastic instability", Journal of Thermal Stresses 20: 185–201.

[6] Zagrodzki, P., (2009), "Thermoelastic instability in friction clutches and brakes-transient modal analysis revealing mechanisms of excitation of unstable modes", International Journal of Solids and Structures 46: 2463–2476.

[7] Yi, Y. B., Barber, J.R., Zagrodzki, P., (2000), "Eigenvalue solution of thermoelastic instability problems using Fourier reduction", Proceedings of the Royal Society of London Series A 456: 2799–2821.

[8] Burton, R.A., Nerlikar, V., Kilaparti, S.R., (1973), "Thermoelastic instability in a seal-like configuration." Wear 24 (1973):177–188.

[9] Yi, Y. B., Du, S., Barber, J. R., and Fash, J. W., (1999), "Effect of Geometry on Thermoelastic Instability in Disk Brakes and Clutches", ASME Journal of Tribology, Vol. 121, pp. 661-666.

[10] Hartsock, D.L., Fash, J.W., (2000), "Effect of pad/caliper stiffness, pad thickness, and pad length on thermoelastic instability in disk brakes", ASME Journal of Tribology 122: 511–518.

[11] Lee, S.W., Jang, Y.H., (2009), "Effect of functionally graded material on frictionally excited thermoelastic instability", Wear 266: 139–146.

[12] Decuzzi, P., Demelio, G., (2002), "The effect of material properties on the thermoelastic stability of sliding systems", Wear 252: 311–321.

[13] Ramousse, S., Hoj, J.W., Sorensen, O.T., (2001), "Thermal characterisation of brake pads", Journal of Thermal Analysis and Calorimetry 64: 933–943.

[14] Choi, J.H., Han, J.H., Lee, I., (2004), "Transient analysis of thermoelastic contact behaviors in composite multidisk brakes", Journal of Thermal Stresses 27: 1149–1167.

[15]Anonymous, AquaMaKKs, (2011), "clutches and brakes stop corrosion, with new composite water jackets that allow cooling with salt water", Anti-Corrosion Methods and Materials 58: 155–155.

[16] Bergman, T.L., Lavine, A.S., Incropera, F.P., DeWitt, D.P., (2007), "Fundamentals of Heat and Mass Transfer", 7th ed., John Wiley & Sons, Inc, Hoboken, NJ.

[17] Zagrodzki, P.,(2009), "Effect of Newtonian Cooling on Frictionally-Excited Thermo- elastic Instability in Wet Friction Clutches and Brakes", In: Proceedings of the 8th International Congress on Thermal Stresses, June 1–4, 2009, Urbana-Champaign, USA.

[18] Payvar, P., Laminar, (1991), "heat-transfer in the oil groove of a wet clutch", International Journal of Heat and Mass Transfer 34: 1791–1798.

[19] Barber, J.R., (1969), "Thermoelastic Instabilities in the Sliding of Conforming Solids", Proceedings of the Royal Society of London Series A, vol. 312, pp. 381–394.

[20] Afferrante, L., Ciavarella, M., and Barber, J.R., (2006),

‘‘Thermoelastodynamic Instability (TEDI): A New Mechanism for Sliding Instability’’, Proceedings of the Royal Society of London Series A, vol. 462, pp. 2161–2176.

[21] Zagrodzki, P., Lam, K.B., Al-Bahkali, E., and Barber, J.R., (2001), ‘‘Nonlinear Transient Behavior of a Sliding System with Frictionally Excited Thermoelastic Instability’’, ASME Journal of Tribology, vol. 123, pp. 699–708.

[22] Du, S., Zagrodzki, P., Barber, J.R., and Hulbert, G.M., (1997), ‘‘Finite Element Analysis of Frictionally-Excited Thermoelastic Instability’’, Journal of Thermal Stresses, vol. 20, pp. 185–201.

[23] Zagrodzki, P., (2009), ‘‘Thermoelastic Instability in Friction Clutches and Brakes Transient Modal Analysis Revealing Mechanisms of Excitation of Unstable Modes’’, International Journal of Solids and Structures, vol. 46, pp. 2463–2476.

[24] Barber, J.R., Beamond, T.W., Waring, J, R., and Pritchard, C., (1985), ‘‘Implications of Thermoelastic Instability for the Design of Brakes’’, ASME Journal of Tribology, vol. 107, pp. 206–210.

[25] Hartsock, D.L., and Fash, J.W., (2000), ‘‘Effect of Pad/Caliper Stiffness, Pad Thickness, and Pad Length on Thermoelastic Instability in Disk Brakes’’, ASME Journal of Tribology, vol. 122, pp. 511–518.

[26] Ayala, J.R.R., Lee, K., Rahman, M., and Barber, J.R., (1996), ‘‘Effect of Intermittent Contact on the Stability of Thermoelastic Sliding Contact’’, ASME Journal of Tribology, vol. 118, pp. 102–108.

[27] Godoy, L. A. (2000), ‘‘Theory of Elastic Stability: Analysis and Sensitivity’’, Taylor & Francis.

[28] Decuzzi, P., and Demelio, G., (2002), ‘‘The Effect of Material Properties on the Thermoelastic Stability of Sliding Systems’’, Wear vol. 252, pp. 311–321.

[29] Hartsock, D. L., and Fash, J. W., (2000) ‘‘Effect of Pad/Caliper Stiffness, Pad Thickness, and Pad Length on Thermoelastic Instability in Disk Brakes’’, Journal of Tribology, Vol. 122, July, pp. 511-518.

[30] Yi, Y. B, (2001) ‘‘Finite Element Analysis of Frictionally Excited

Thermoelastic Instabilities in Automotive Brakes and Clutches", Ph.D. Dissertation, University of Michigan.

[31] Yi, Y. B, (2006), "Finite Element Analysis of Thermoelastodynamic Instability Involving Frictional Heating", ASME Journal of Tribology, vol. 128, pp. 718–724.

[32] Burton, R.A., Netlike, V., and Kilaparti, S.R., (1973) "Thermoelastic Instability in a Seal-Like Configuration", Wear vol. 24, pp. 177–188.

[33] Lee, K.J., and Barber, J.R., (1993), "Frictionally-Excited Thermoelastic Instability in Automotive Disk Brakes", ASME Journal of Tribology, vol. 115, pp. 607–614, 1993.

[34] Straub, H., Der Lamellenverschleiss als Lebensdauergrenze, VDI-Berichte, (1963) vol. 73, pp. 81-87.

[35] Newcomb, T.P., and Spurr, R.T., (1973), "The Interaction Between Friction Materials and Lubricants", Wear vol. 24, pp. 69-76.

[36] Zagrodzki, P., (1985), "Numerical Analysis of Temperature Fields and Thermal Stresses in the Friction Disks of a Multidisc Wet Clutch", Wear, vol. 101, pp. 255-271.

[37] Nadine Audebert, Barber, J.R., Zagrodzki, P., (1998), "Buckling Of Automatic Transmission Clutch Plates Due To Thermoelastic / Plastic Residual Stresses", Thermal Stresses, 21:309-326.

[38] Timoshenko, Stephen.P., Gere, James.M., (1961), "Theory of Elastic Stability" published by the Mc Graw-Hill Book Company, Inc.

[39] Kao, T.K., Richmond, J.W., Douarre, A., (2000), "Brake disc hot spotting and thermal judder: an experimental and finite element study", Int. J. of Vehicle Design, Vol. 23, No. ¾, pp. 276-296

[40] Matysiak, S.J., Yevtushenko, A.A., and Ivanyk, E.G., (2002), "Contact temperature and wear of composite friction elements during braking", International Journal of Heat and Mass Transfer, Volume 45, Issue 1, pp. 193–199

[41] Ashby, M.F., Abulawi, J., Kong, H.S., (1991), "Temperature Maps for Frictional Heating in Dry Sliding", Tribology

Transactions. Volume 34, Issue 4, pp.577-587.

[42] Fan, X, and Lippmann, H., (1996), "Elastic-Plastic Buckling of Plates under Residual Stress", Advances in Engineering Plasticity and Its Applications. Proc. AEPA/ 96, 21-24 Aug., pp. 95-100.

[43] Halderman, J. D. and Mitchell, C. D., (2000), ‘‘Automotive Brake Systems’’, 2nd Ed. Prentice Hall Multimedia Series in Automotive Technology.

[44] Yi, Y. B., Barber, J. R., and Hartsock, D. L., (2002), Thermoelastic instabilities in automotive disc Brakes - Finite element analysis and experimental verification, in J.A.C.Martins and Manuel D.P.Monteiro Marques eds., Contact Mechanics, Kluwer, Dordrecht, pp. 187-202.

[45] Dufrénoy, P., & Weichert, D., (2003), ‘‘Thermomechanical model for the analysis of disc brake fracture mechanisms’’, Journal of Thermal Stresses Volume 26, Issue 8, pp. 815-828.

[46] Quinna, T.F.J., (1967), ‘‘The Effect of ‘‘Hot-Spot’’ Temperatures on the Unlubricated Wear of Steel’’, A S L E Transactions Volume 10, Issue 2, pp.158-168.

[47] Adebisi, A.A., Maleque, M.A., and Shah, Q.H., (2011), ‘‘Surface temperature distribution in composite brake rotor’’, International Journal of Mechanical and Materials Engineering (IJMME), Vol.6 (2011), No.3, pp. 356-361

[48] Choi, J. H. and Lee I. (2004). ‘‘Finite element analysis of transient thermoelastic behaviors in disk brakes’’. Wear, 257 (1-2), 47-58.

[49] Eltoukhy, M., Asfour, S., Almakky, M., and Huang, C., (2006), ‘‘Thermoelastic Instability in Disk Brakes: Simulation of the Heat Generation Problem’’, Proceedings of the COMSOL Users Conference, Boston, USA.

[50] Turvey, G. J. and Drinali, H., (1985), "Elastic Postbuckling of Circular and Annular Plates with Imperfections", Proc. 3rd Int. Conf. Composite Structure, Applied Science Publication. pp. 315-335.

[51] Singh, H., Shergill, H., (2012), ‘‘Thermal Analysis of Disc Brake Using Comsol’’, International Journal on Emerging Technologies

3(1): pp.84-88.

[52] Chen, L. W., and Hwang, J. R. (1989) “Finite Element Analysis of Thick Annular Plates under Internal Forces", Computers & Structures, Vol. 32. No. 1, pp. 63-68.

[53] Dow, T.A., and Burton, R.A., (1972), “Thermoelastic Instability of Sliding Contact in the Absence of Wear”, Wear vol. 19, pp. 315-328.

[54] Kennedy, F.E., and Ling, F.F., (1974), “A Thermal, Thermoelastic and Wear Simulation of a High Energy Sliding Contact Problem”, ASME J. Lub. Tech., vol. 96, pp. 497-507.

[55] Zagrodzki, P., (1990), “Analysis of Thermomechanical Phenomena in Multidisc Clutches and Brakes”, Wear, vol. 140, pp. 291-308.

[56] Chang, J. S. and Shiao, F. J., (1990), “Thermal Buckling Analysis of Isotropic and Composite Plates with a Hole”, Journal of Thermal Stresses, Vol. 13, pp. 315- 332.

[57] Bruno A. Boley, Jerome H. Weiner. (1960) “Theory of Thermal Stresses”, by John Wiley & Sons, Inc.

[58] Yi, Y.B., Bendawi, A., Li, H., and Zhao, J., (2014), “Finite Element Analysis of Thermoelastic Instability in Intermittent Sliding Contact”, Journal of Thermal Stresses Vol 37:pp. 870–883.

[59] Yi, Y.B. and Bendawi, A., (2012), “Effect of Convective Cooling on Frictionally Excited Thermoelastic Instability”, Wear, Vol. 296, pp. 583-589.

[60]. Yi, Y.B., (2010), “Finite Element Analysis of Thermoelastic Damping in Contour-Mode Vibrations of Micro- and Nanoscale Ring, Disk, and Elliptical Plate Resonators”, ASME Journal of Vibration and Acoustics, Vol. 132 (4), art. 041015, pp.1-7.

[63] Avalos, D. R. et al. ,(1995), "Transverse Vibrations and Buckling of Circular Plates of Discontinuously Varying Thickness subject to an In-plane State of Hydrostatic Stress", Ocean Engineering, Vol. 22, no. 1, pp. 105-110.

[61] Azarkhin, A. and Barber, J. R., (1986), "Thermoelastic

Instability for the Transient Contact Problem of Two Sliding Half-Planes", Journal of Applied Mechanics, Vol. 53, pp. 565-571.

[62] Barber, J. R., (1984), "Thermoelastic Displacements and Stresses due to a Heat Source Moving over the Surface of a Half Plane", Journal of Applied Mechanics, Vol. 51, pp. 636-640.

[63] Barber, J. R., (1986), "Nonuniqueness an Stability for Heat Conduction through a Duplex Heat Exchanger Tube", Journal of Thermal Stresses, Vol. 9, pp.69-78.

[64] Barber, J. R., (1987), "Thermoelastic Distortion of the Half-Space", Journal of Thermal Stresses, Vol. 10, pp. 221-228.

[65] Bargmann, H. W., (1985), "Thermal Buckling of Elastic Plates", Journal of Thermal Stresses, Vol. 8, pp. 71-98.

[66] Berger, E. J., Krousgrill, C. M. And Sadeghi, F., (1997), "Stability of Sliding in a System Excited by Rough Moving Surface", Journal of Tribology, Vol. 119, pp. 673-680.

[67] Bloom, F. and Goffin, D., (2001), Hand book of Thin Plate Buckling and Postbuckling, Chapman & Hall/CRC

[68] Boley, B. A., (1969), "On Thermal Stresses and Deflections in Thin Ring",
International Journal of Mech. Science, Vol. 11, pp. 781-789.

[69] Boley, B. A., and Weiner, J. H. (1960), "Theory of Thermal Stresses", John Wiley and Sons, New York.

[70] Brush, D. O., and Almroth, B. O., (1975), "Buckling of Bars, Plates and Shells", McGraw- Hill.

[71] Bryan, G. H., (1891), "Buckling of Plates", Proceedings of the London Mathematical Society, Vol. 22, pp.54.

[72] Chang, C. N., and Chiang, F. K., (1990), "Stability Analysis of a Thick Plate with Interior Cutout ", AlAA Journal, Vol. 28, no. 7, pp. 1285-1291.

[73] Chang, T. P., and Chang, H. C., (1997), "Vibration and Buckling Analysis of Rectangular Plates with Nonlinear Elastic End Restraints Against Rotation", International Journal of Solid s Structures, Vol. 34, No. 18, pp. 2291-2301.

[74] Cook, Robert D., Malkus, David S., and Plesha, Michael, E.,

(1989), ‘‘Concepts and Applications of Finite Element Analysis’’, John Eiley & Sons, Inc.

[75] Dean, W. R., (1924), "The Elastic Stability of an Annular Plate," Proceedings of the Royal Society of London, England, Ser. A, Vol. 106, p.268.

[76] Du, S., Zagrodzki, P., Barber, J. R., & Hulbert, G. M. (1997) "Finite Element Analysis of Frictionally-Excited Thermoelastic Instability", Journal of Thermal Stress, Vol. 20, pp. 185-201.

[77] Du, S., and Fash, J. W. (2000) "Finite Element Analysis of Frictionally-Excited Thermoelastic Instability in 3D Annular Disk", International Journal of Vehicle Design, Vol. 23, nos. 3/4, pp. 203-217.

[79] DuPay, R. K. et al., (2000), ‘‘Automotive Brake Systems’’, 3rd Ed., Chek-Chart Publications. Prentice Hall.

[80] Elishakoff, I., and Tang, J., (1988), "Buckling of Polar Orthotropic Circular Plates on Elastic Foundation by Computerized Symbolic Algebra", Computer Method s in Applied Mechanics and Engineering, Vol. 68, pp. 229-247.

[82] Fuad, K., Daimaruya, M. and Kobayashi, H., (1994), "Temperature and Thermal Stresses in a Brake Drum Subjected to Cyclic Heating", Journal of Thermal Stresses, Vol. 17, pp. 515-527.

Appendix A

1 Example of Matlab Program

1.1 Linear Temperature & Stress Distribution

```
clc;
format;
alpha = 12.5e-6; % thermal expansion coefficient (should vary with temperature?)
E = 210e3; % N/mm^2 Young's modulus (should vary with temperature?)
v = 0.3; % Poisson's ratio
ra = 60; % radius of hole
rb = 80; % maximum radius of disc
h = 2; % thickness of chunk (mm)
Tmin = 0;
Tmax = 800;
Trange = Tmax - Tmin;
rinc = 1.0; % increments of r from ra to rb to use for calculation
r = ra:rinc:rb;
R = (ra+rb)/2;
y = 0:20;
m =(Tmax-Tmin)/(rb-ra);
T =(m*(r-ra))+Tmin;
intr_f = @(r) (1/6)*((-3*ra*m*r.^2)+(2*m*r.^3)+(3*r.^2*Tmin));
intr = intr_f(r) - intr_f(ra);
C1 = (1-v)*alpha ./ (rb^2 - ra^2) * intr(end);
C2 = (1+v)*alpha*ra^2 ./ (rb^2 - ra^2) * intr(end);
stressr = -(alpha*E./r.^2).*intr + E*(C1/(1-v) - C2./((1+v)*r.^2));
stressphi = (alpha*E./r.^2).*intr - alpha*E*T + E*(C1/(1-v) + C2./((1+v)*r.^2));
% Figures
figure(1);
plot(y',stressr','-*');
title('stress vs y');
xlabel('y(mm)');
ylabel('stress');
hold on
plot(y',stressphi','-');
legend('stress_r','stress_P_h_i');
figure(2);
plot(y',stressr','-');
title('stress_r vs y');
xlabel('y(mm)');
ylabel('stress_r');
figure(3);
plot(y',stressphi','-');
title('stress_p_h_i vs y');
```

```
xlabel('y(mm)');
ylabel('stress_p_h_i');
figure(4);
plot(y',T','-');
title('T vs y');
xlabel('y(mm)');
ylabel('T');
```

1.2 Relationship between actual moment and critical moments for linear temperature with varying central radius

```
%close all;
clear;
clc;
format;
% --- Independent Variables ---
alpha = 12.5e-6; % thermal expansion coefficient (should vary with temperature?)
E = 210e3 ; % Young's modulus (should vary with temperature?)
v = 0.3; % Poisson's ratio
G = E/(2*(1+v)); % N.mm-2
h = 3; % thickness of chunk (mm)
a = 30; % radial thickness
Tmin = 0;
Tmax = 456;
rpoints = 30; % number of points between ra and rb
 Rrange =  80:10:140;
%Rrange = 125;
stressr(rpoints,length(Rrange)) = 0;
stressphi(rpoints,length(Rrange)) = 0;
M(length(Rrange)) = 0;
Mcr(length(Rrange),2) = 0;
for Ri = 1:length(Rrange)
R = Rrange(Ri)
ra = R - a/2; % radius of hole
rb = R + a/2; % maximum radius of disc
r = linspace(ra,rb,rpoints);
y = r - R;
m =(Tmax-Tmin)/a;
T =(m*(r-ra))+Tmin;
intr_f = @(r) (1/6)*((-3*ra*m*r.^2)+(2*m*r.^3)+(6*r.*Tmin));
intr = intr_f(r) - intr_f(ra);
%C1 = (1-v)*alpha ./ (rb^2 - ra^2) * intr(end);
C1 = alpha ./ (2*(1-v)*(rb^2 - ra^2)) * intr(end);
C2 = (1+v)*alpha*ra^2 ./ (rb^2 - ra^2) * intr(end);
stressr   = -alpha*E * (intr ./r.^2      + intr(end)/(rb^2 - ra^2) * (1 - ra^2 ./ r.^2));
```

```
stressphi =  alpha*E * (intr ./ r.^2 - T + intr(end)/(rb^2 - ra^2) * (1 + ra^2 ./ r.^2));
qL1 = @(r) ((-(ra*m - Tmin) / 2) * r.^2 / 2 + (m / 3) * r.^3 / 3)   -   ((-(ra*m - Tmin) / 2) *
ra^2 + (m / 3) * ra^3) * log(r);
qL2 = @(r) m * r.^3 / 3 + (Tmin - m*ra) * r.^2 / 2;
qL3 = @(r) (-(ra*m - Tmin) / 2) * (rb^2 - ra^2) + (m / 3) * (rb^3 - ra^3);
QphiL_f = @(r) (alpha*E/2 * (qL1(r) - qL2(r) + (r.^2 / 2 + ra^2 * log(r)) * qL3(r) / (rb^2
- ra^2)));
QphiL = QphiL_f(rb) - QphiL_f(ra);
qR1 = @(r) ((-(ra*m  - Tmin) / 2) * r + (m / 3) * r.^2 / 2)   -   ((-(ra*m  - Tmin) / 2) * ra^2
+ (m / 3) * ra^3) * - 1 ./ r;
qR2 = @(r) m * r.^2 / 2 + (Tmin - m*ra) * r;
QphiR_f = @(r) alpha*E * (qR1(r) - qR2(r) + (r + ra^2 * -1 ./ r) * qL3(r) / (rb^2 - ra^2))
* ra ;
QphiR = QphiR_f(rb) - QphiR_f(ra);
M(Ri) = (QphiL-QphiR)*h
K = (1+v) /2;
N = 2 ;
McrNoDimPos = (1 + K) / 2 + hypot((1-K)/2, sqrt(K)*N);
McrNoDimNeg = (1 + K) / 2 - hypot((1-K)/2, sqrt(K)*N);
Mcr(Ri,1) = McrNoDimPos*G*a*h^3/(3*R);
Mcr(Ri,2) = McrNoDimNeg*G*a*h^3/(3*R)
end
% Figures
figure(1001);
plot(Rrange',Mcr,'s-'); % comment out for combined
hold on;
plot(Rrange',M','k');
title('Moment vs Critical Moment');
xlabel('Center Radius (mm)');
ylabel('Moment (N.mm) ');
%legend('Critical Moment (+)','Critical Moment (-)','Moment (r)','Moment (phi)'); %
uncomment for combined
legend('Critical Moment (+)','Critical Moment (-)','Moment (phi)at T= '); % comment out
for combined
```

1.3 Parabolic Temperature Distribution & Stress Distribution

```
close all;
clear;
clc;
format;
alpha = 12.5E-6; % thermal expansion coefficient (should vary with temperature?)
E = 210E3; % Young's modulus (should vary with temperature?)
v = 0.3; % Poisson's ratio
ra = 60; % radius of hole
```

```
rb = 80; % maximum radius of disc
rinc = 1.0; % increments of r from ra to rb to use for calculation
h = 1; % thickness of chunk (mm)
Tmax = 1000;
r = ra:rinc:rb;
R = (ra+rb)/2;
thickness = rb - ra;
%y = r - R;
y = 0:20
a = rb-ra;
T = Tmax - (r - R).^2 * (Tmax / (a/2)^2);
Q = Tmax / (thickness/2)^2;
%intr_f = @(r) -Q*r.^4/4 + 2*Q*R*r.^3/3 + (Tmax - Q*R^2)*r.^2/2;
intr_f = @(r) 1/12*(-3*Q*r.^4 +8*r.^3*Q*R -6*r.^2*Q*R^2 +6*r.^2*Tmax);
intr = intr_f(r) - intr_f(ra);
C1 = alpha ./ (2*(1-v)*(rb^2 - ra^2)) * intr(end);
C2 = (1+v)*alpha*ra^2 ./ (rb^2 - ra^2) * intr(end);
stressr = -(alpha*E./r.^2).*intr + E*(C1/(1-v) - C2./((1+v)*r.^2));
stressphi = (alpha*E./r.^2).*intr - alpha*E*T + E*(C1/(1-v) + C2./((1+v)*r.^2));
% Figures
figure(1);
plot(y',stressr','-*');
title('stress vs y');
xlabel('y(mm)');
ylabel('stress');
hold on
plot(y',stressphi','-');
legend('stress_r','stress_P_h_i');
figure(2);
plot(y',stressr','-');
title('stress_r vs y');
xlabel('y');
ylabel('stress_r');
figure(3);
plot(y',stressphi','-');
title('stress_p_h_i vs y');
xlabel('y');
ylabel('stress_p_h_i');
figure(4);
plot(y',T','-');
title('T vs y');
xlabel('y (mm)');
ylabel('T');
```

1.4 Relationship between actual moment and critical moments for parabolic temperature distribution with varying central radius

```
% close all;
Clear ;
clc;
format;
alpha = 12.5e-6; % thermal expansion coefficient (should vary with temperature?)
E = 210e3; % Young's modulus (should vary with temperature?)
v = 0.3; % Poisson's ratio
G = E/(2*(1+v)); % GPa
h = 1 ; % thickness of chunk (mm)
a = 20; % radial thickness
Tmax = 630;
rpoints = 30; % number of points between ra and rb
Rrange = 40:10:160;
stressr(rpoints,length(Rrange)) = 0;
stressphi(rpoints,length(Rrange)) = 0;
M(length(Rrange)) = 0;
Mcr(length(Rrange),2) = 0;
for Ri = 1:length(Rrange)
R = Rrange(Ri)
ra = R - a/2; % radius of hole
rb = R + a/2; % maximum radius of disc
r = linspace(ra,rb,rpoints);
y = r - R;
A=((rb-ra)/2)^2;
Q = Tmax/A;
T = Tmax - (r - R).^2 * Q;
intr_f = @(r) (1/12)*(8*Q*R*r.^3 -3*Q*r.^4 -6*R^2*r.^2*Q +6*r.^2 *Tmax);
intr = intr_f(r) - intr_f(ra);
C1 = alpha ./ (2*(1-v)*(rb^2 - ra^2)) * intr(end);
C2 = -(1+v)*alpha*ra^2 ./ (ra^2 - rb^2) * intr(end);
stressr = -(alpha*E./r.^2).*intr + E*(C1/(1-v) - C2./((1+v)*r.^2));
stressphi = (alpha*E./r.^2).*intr - alpha*E*T + E*(C1/(1-v) + C2./((1+v)*r.^2));
L1=alpha*E/12*(ra^2*log(rb/ra)*(3*ra^2*Q-8*ra*Q*R+6*Q*R^2-6*Tmax) +
Q/12*(32*rb^3*R-32*ra^3*R-9*rb^4+9*ra^4-
36*R^2*rb^2+36*R^2*ra^2)+3*Tmax*(rb^2-ra^2));
L2=alpha*E/12*(Q*(3*ra^4-3*rb^4+8*rb^3*R-8*ra^3*R-
6*rb^2*R^2+6*ra^2*R^2)+6*Tmax*(rb^2-ra^2));
L3=E*C1/(2*(1-v))*(rb^2-ra^2);
L4=E*C2/(1+v)*log(rb/ra);
LL=L1-L2+L3+L4;
```

```
W1=alpha*E*ra/12*(ra^2/rb*(8*ra*Q*R-3*ra^2*Q+6*Tmax-6*Q*R^2)+4*ra^3*Q-
12*ra^2*Q*R+12*ra*Q*R^2-12*ra*Tmax+6*rb*Tmax-Q*rb^3+4*Q*rb^2*R -
6*Q*R^2*rb );
W2=alpha*E*ra /3*((ra-rb)*(ra^2*Q +ra*Q*(rb-3*R) +Q*rb^2 -3*rb*R*Q +3*Q*R^2-
3*Tmax));
W3=(E*C1*ra)/(1-v)*(rb-ra);
W4=(E*C2)/(v+1)*(1-(ra/rb));
WW=W1-W2+W3+W4;
M(Ri) = (h*(LL - WW))
K = (1+v) / 2;
N = 2;
McrNoDimPos = (1 + K) / 2 + hypot((1-K)/2, sqrt(K)*N);
McrNoDimNeg = (1 + K) / 2 - hypot((1-K)/2, sqrt(K)*N);
Mcr(Ri,1) = McrNoDimPos*G*a*h^3/(3*R);
Mcr(Ri,2) = McrNoDimNeg*G*a*h^3/(3*R)
end
figure(1003);
plot(Rrange',Mcr,'s-'); % comment out for combined
hold on;
plot(Rrange',M','r');
title('');
xlabel('Center Radius (mm)');
ylabel('Moment (N.mm)');
%legend('Critical Moment (+)','Critical Moment (-)','Moment (r)','Moment (phi)'); %
uncomment for combined
legend('Critical Moment (+)','Critical Moment (-)','Moment (phi)'); % comment out for
combined
```

1.5 Power Temperature Distribution & Stress Distribution

```
%close all;
clear;
clc;
format;
% --- Independent Variables ---
alpha = 12.5e-6; % thermal expansion coefficient (should vary with temperature?)
E = 210e3; % Young's modulus (should vary with temperature?)
v = 0.3; % Poisson's ratio
G = E/(2*(1+v)); % N.mm-2
h = 2; % thickness of chunk (mm)
a = 20; % radial thickness
rinc = 1.0; % increments of r from ra to rb to use for calculation
Tmax =    1000;
rpoints = 30; % number of points between ra and rb
R =70;
```

```
ra =60; % radius of hole
rb =80; % maximum radius of disc
r = ra:rinc:rb;
y =0:20;
B=(rb-ra)^4;
T = (r-ra).^4/B * Tmax ;
intTrdr_f = @(r)   (Tmax/(30*B))*(15*r.^2*ra^4 -40*ra^3*r.^3 +45*ra^2*r.^4 -
24*ra*r.^5 +5*r.^6);
intTrdr = intTrdr_f(r) - intTrdr_f(ra);
C1 = alpha ./(2*(1-v)*(rb^2 - ra^2)) * intTrdr(end);
C2 = (1+v)*alpha*ra^2 ./ (rb^2 - ra^2) * intTrdr(end);
stressr  = -(alpha*E./r.^2).*intTrdr + E*(C1/(1-v) - C2./((1+v)*r.^2));
stressphi = (alpha*E./r.^2).*intTrdr - alpha*E*T + E*(C1/(1-v) + C2./((1+v)*r.^2));
figure(1);
plot(y',stressr','-*');
title('stress vs y');
xlabel('y(mm)');
ylabel('stress');
hold on
plot(y',stressphi','-');
legend('stress_r','stress_P_h_i');
figure(2);
plot(y',stressr','-');
title('stress_r vs y');
xlabel('y');
ylabel('stress_r');
figure(3);
plot(y',stressphi','-');
title('stress_p_h_i vs y');
xlabel('y');
ylabel('stress_p_h_i');
figure(4);
plot(y',T','-');
title('T vs y');
xlabel('y (mm)');
ylabel('T');
```

1.6 Relationship between actual moment and critical moments for Power temperature distribution with varying central radius

```
%close all;
clear;
clc;
format;
alpha = 12.5e-6; % thermal expansion coefficient (should vary with temperature?)
E = 210e3; % Young's modulus (should vary with temperature?)
```

```
v = 0.3; % Poisson's ratio
G = E/(2*(1+v)); % N.mm-2
h = 2; % thickness of chunk (mm)
a = 20; % radial thickness
Tmax =    318;
rpoints = 30; % number of points between ra and rb
Rrange = 90:10:140;
stressr(rpoints,length(Rrange)) = 0;
stressphi(rpoints,length(Rrange)) = 0;
M(length(Rrange)) = 0;
Mcr(length(Rrange),2) = 0;
for Ri = 1:length(Rrange)
R  = Rrange(Ri)
ra = R - a/2; % radius of hole
rb = R + a/2; % maximum radius of disc
r = linspace(ra,rb,rpoints) ;
y = r - R;
B=(rb-ra)^4;
T = (r-ra).^4/B * Tmax ;
intTrdr_f = @(r)   (Tmax/(30*B))*(15*r.^2*ra^4 -40*ra^3*r.^3 +45*ra^2*r.^4 -
24*ra*r.^5 +5*r.^6);
intTrdr = intTrdr_f(r) - intTrdr_f(ra);
C1 = alpha ./(2*(1-v)*(rb^2 - ra^2)) * intTrdr(end);
C2 = (1+v)*alpha*ra^2 ./ (rb^2 - ra^2) * intTrdr(end);
stressr(:,Ri)   = -(alpha*E./r.^2).*intTrdr + E*(C1/(1-v) - C2./((1+v)*r.^2));
stressphi(:,Ri) = (alpha*E./r.^2).*intTrdr - alpha*E*T + E*(C1/(1-v) + C2./((1+v)*r.^2));
L1=alpha*E*Tmax/(950*B)*(60*ra^6*log(ra/rb) +450*ra^4*rb^2 -800*ra^3*rb^3
+675*ra^2*rb^4 -288*ra*rb^5 +50*rb^6 -87*ra^6);
L2=alpha*E*Tmax/(30*B)*(15*rb^2*ra^4 -40*rb^3*ra^3 +45*ra^2*rb^4 -24*ra*rb^5
+5*rb^6-ra^6);
L3=E*C1/(2*(1-v))*(rb^2-ra^2);
L4=E*C2/(1+v)*log(rb/ra);
LL=L1-L2+L3+L4;
W1=alpha*E*ra*Tmax/(30*B)*((ra^6/rb) +15*ra^4*rb -20*ra^3*rb^2 +15*ra^2*rb^3 -
6*ra*rb^4 +rb^5 6*ra^5);
W2=alpha*E*ra*Tmax/(5*B)* (rb-ra)^5;
W3=(E*C1*ra)/(1-v)*(rb-ra);
W4=(E*C2)/(v+1)*(1-(ra/rb));
WW=(W1-W2+W3+W4);
M(Ri) = h*(LL - WW)
K = (1+v) / 2;
N = 2;
McrNoDimPos = (1 + K) / 2 + hypot((1-K)/2, sqrt(K)*N);
McrNoDimNeg = (1 + K) / 2 - hypot((1-K)/2, sqrt(K)*N);
```

```
Mcr(Ri,1) = McrNoDimPos*G*a*h^3/(3*R);
Mcr(Ri,2) = McrNoDimNeg*G*a*h^3/(3*R)
end
figure(1001);
plot(Rrange',Mcr,'s-'); % comment out for combined
hold on;
plot(Rrange',M','r');
title('');
xlabel('Radius (mm)');
ylabel('Moment (N.mm) ');
legend('Critical Moment (+)','Critical Moment (-)','Moment (phi)'); % comment out for
combined
```

Appendix B

2. Examples of Abaqus INP File

2.1 Linear temperature distribution at center radius change

```
*Heading
** Job name: R60 Model name: Model-1
** Generated by: Abaqus/CAE 6.13-1
*Preprint, echo=NO, model=NO, history=NO, contact=NO
**
** PARTS
**
*Part, name=Part-1
*Node
      1,          45.,           0.,           0.
      2,          45.,           0.,           3.
      3,         -45.,           0.,           3.
      4,         -45.,           0.,           0.
      5,          75.,           0.,           3.
      6,         -75.,           0.,           3.
      7,         -75.,           0.,           0.
      8,          75.,           0.,           0.
      9,   44.9440613,   2.24306488,           3.
     10,   44.7763863,   4.48055315,           3.
     11,   44.4973869,   6.70690203,           3.
     12,   44.1077614,   8.91657639,           3.
     13,   43.6084785,   11.1040831,           3.
     14,   43.0007744,   13.2639828,           3.
     15,   42.2861671,   15.3909063,           3.
   ~ ~ ~
   2765,  -66.3462906,  -27.9673061,           0.
   2766,  -67.6578674,  -24.6254501,           0.
   2767,   -68.801239,  -21.2223721,           0.
   2768,  -69.7735672,  -17.7665329,           0.
   2769,  -70.5724182,  -14.2665224,           0.
   2770,   -71.195816,  -10.7310429,           0.
*Element, type=C3D8I
     1,  274,  284, 1099,  541,    1,    2,    9,  132
     2,  541, 1099, 1100,  542,  132,    9,   10,  131
     3,  542, 1100, 1101,  543,  131,   10,   11,  130
     4,  543, 1101, 1102,  544,  130,   11,   12,  129
     5,  544, 1102, 1103,  545,  129,   12,   13,  128
     6,  545, 1103, 1104,  546,  128,   13,   14,  127
```

```
     7,  546, 1104, 1105,  547,  127,   14,   15,  126
     8,  547, 1105, 1106,  548,  126,   15,   16,  125
~~~~
    1258,  538,  419,  418,  539, 2212, 2770, 2771, 2213
    1259,  539,  418,  417,  540, 2213, 2771, 2772, 2214
    1260,  540,  417,    7,    6, 2214, 2772,  265,  275
*Nset, nset=Set-1, generate
    1,  2772,     1
*Elset, elset=Set-1, generate
    1,  1260,     1
** Section: Section-1
*Solid Section, elset=Set-1, material=Steel
*End Part
**
**
** ASSEMBLY
**
*Assembly, name=Assembly
**
*Instance, name=Part-1-1, part=Part-1
*End Instance
```

2.2 Parabolic temperature distribution at sliding length change

```
*Heading
** Job name: A10 Model name: Model-1
** Generated by: Abaqus/CAE 6.13-1
*Preprint, echo=NO, model=NO, history=NO, contact=NO
**
** PARTS
**
*Part, name=Part-1
*Node
      1,          95.,           0.,           0.
      2,          95.,           0.,          0.5
      3,         -95.,           0.,          0.5
      4,         -95.,           0.,           0.
      5,         105.,           0.,          0.5
      6,        -105.,           0.,          0.5
      7,        -105.,           0.,           0.
      8,         105.,           0.,           0.
      9,   94.9566574,   2.86928773,          0.5
     10,   94.8266754,   5.73595715,          0.5
*Element, type=C3D8I
     1,  424,  427, 1047,  841,    1,    2,    9,  214
```

```
   2,  841, 1047, 1048,  842,  214,    9,   10,  213
   3,  842, 1048, 1049,  843,  213,   10,   11,  212
   4,  843, 1049, 1050,  844,  212,   11,   12,  211
   5,  844, 1050, 1051,  845,  211,   12,   13,  210
   6,  845, 1051, 1052,  846,  210,   13,   14,  209
   7,  846, 1052, 1053,  847,  209,   14,   15,  208
*Nset, nset=Set-1, generate
   1,  1664,     1
*Elset, elset=Set-1, generate
   1,  624,    1
** Section: Section-1
*Solid Section, elset=Set-1, material=STEEL
*End Part
**
**
** ASSEMBLY
**
*Assembly, name=Assembly
**
*Instance, name=Part-1-1, part=Part-1
*End Instance
**
*Nset, nset=Set-1, instance=Part-1-1
    2,   3,   5,   6,   9,  10,  11,  12,  13,  14,  15,  16,  17,  18,  19,  20
    21,  22,  23,  24,  25,  26,  27,  28,  29,  30,  31,  32,  33,  34,  35,  36
    37,  38,  39,  40,  41,  42,  43,  44,  45,  46,  47,  48,  49,  50,  51,  52
*Elset, elset=Set-1, instance=Part-1-1, generate
    1,  624,    1
*End Assembly
**
** MATERIALS
**
*Material, name=STEEL
*Conductivity
  43.,
*Elastic
   210000., 0.3
*Expansion
   1.25e-05,
** ----------------------------------------------------------------
**
** STEP: Step-1
**
*Step, name=Step-1, nlgeom=NO, perturbation
```

```
*Buckle
   6, , 12, 90
**
** PREDEFINED FIELDS
**
** Name: Predefined Field-1   Type: Temperature Using Field: AnalyticalField-1
*Temperature
Part-1-1.2, 0.
Part-1-1.3, 0.
Part-1-1.5, 0.
Part-1-1.6, 0.
Part-1-1.9, -0.000845284
**
** OUTPUT REQUESTS
**
*Restart, write, frequency=0
**
** FIELD OUTPUT: F-Output-1
**
*Output, field, variable=PRESELECT
*End Step
```

2.3 Power temperature distribution at main center change

```
*Heading
** Job name: R80 Model name: Model-1
** Generated by: Abaqus/CAE 6.13-1
*Preprint, echo=NO, model=NO, history=NO, contact=NO
**
** PARTS
**
*Part, name=Part-1
*Node
      1,          70.,           0.,           0.
      2,          70.,           0.,           2.
      3,         -70.,           0.,           2.
      4,         -70.,           0.,           0.
      5,          90.,           0.,           2.
*Element, type=C3D8I
  1,  348,  355, 1181,  689,    1,    2,    9,  172
  2,  689, 1181, 1182,  690,  172,    9,   10,  171
  3,  690, 1182, 1183,  691,  171,   10,   11,  170
*Nset, nset=Set-1, generate
   1,  2656,     1
*Elset, elset=Set-1, generate
```

```
** Section: Section-1
*Solid Section, elset=Set-1, material=STEEL
*End Part
**
**
** ASSEMBLY
**
*Assembly, name=Assembly
**
*Instance, name=Part-1-1, part=Part-1
*End Instance
**
*Nset, nset=Set-1, instance=Part-1-1
   2,   3,   5,   6,   9,  10,  11,  12,  13,  14,  15,  16,  17,  18,  19,  20
  21,  22,  23,  24,  25,  26,  27,  28,  29,  30,  31,  32,  33,  34,  35,  36
  37,  38,  39,  40,  41,  42,  43,  44,  45,  46,  47,  48,  49,  50,  51,  52
*Elset, elset=Set-1, instance=Part-1-1, generate
   1, 1162,    1
*End Assembly
**
** MATERIALS
**
*Material, name=STEEL
*Conductivity
  43.,
*Elastic
  210000., 0.3
*Expansion
  1.25e-05,
** ----------------------------------------------------------------
**
** STEP: Step-1
**
*Step, name=Step-1, nlgeom=NO, perturbation
*Buckle
  6, , 12, 60
**
** PREDEFINED FIELDS
**
** Name: Predefined Field-1   Type: Temperature Using Field: AnalyticalField-1
*Temperature
Part-1-1.2, 0.
Part-1-1.3, 0.
Part-1-1.5, 1000.
```

Part-1-1.6, 1000.
**
** OUTPUT REQUESTS
**
*Restart, write, frequency=0
**
** FIELD OUTPUT: F-Output-1
**
*Output, field, variable=PRESELECT
*End Step